Title	Study of the Effect of Horizontal Plates on the Dynamic Response and Sliding of Caisson Breakwaters
Author(s)	Fundora Campos, Sila Mercedes
Citation	大阪大学, 2024, 博士論文
Version Type	VoR
URL	https://doi.org/10.18910/98794
rights	
Note	

Doctoral Dissertation

Study of the Effect of Horizontal Plates on the Dynamic Response and Sliding of Caisson Breakwaters

Sila Mercedes Fundora Campos

June 2024

Graduate School of Engineering,
Osaka University

ABSTRACT

Investigating the performance of breakwaters during the failure process has recently been mainly emphasized inside Japan. Performance can be evaluated through reliability design methods based on the deformation level using parameters such as sliding. Although it has not yet been completely applied to actual design due to the difficulties of considering all design conditions, it is expected to become one of the essential design methodologies in the future. Caisson breakwaters are among the most commonly constructed breakwaters, especially in Japan. Sliding is their most frequent failure mode, and even though it is not allowed under conventional design, caissons can maintain their functionality even if a limited amount of it occurs. Breakwater caissons' performance during the failure process was investigated in this study by developing a reliable design method to evaluate the effectiveness of introducing horizontal plates to reduce the caissons' sliding motion. Such structure proposal was based on the hypothesis that a horizontal plate located at the harborside could increase the water constriction during the movement of the caisson, increasing the hydrodynamic response through parameters such as the added mass and, consequently, decreasing the expected sliding distance and expanding the structure's functionality.

Chapter 1 of this study provided a general background on vertical breakwaters along with the problem statement, objectives, and research approach.

Chapter 2 examined documented vertical breakwater failures due to impulsive pressures and reviewed and summarized fundamental and recent studies involving impulsive pressures from a caisson design viewpoint, including prediction methods to estimate the maximum impact load and existing models for wave loading and dynamics of caisson breakwaters.

Chapter 3 described the derivation of a model for caissons with horizontal plates (non-regular caissons) and the methodology to estimate the hydrodynamic coefficients of the dynamic response and the sliding for these structures.

Chapter 4 discussed the application of the models derived in Chapter 3. The influence of the plate's geometric characteristics and arrangements on the pressures, the hydrodynamic parameters added mass (constant added mass) and damping coefficient (memory effect function), and the caisson's sliding were the objects of discussion. Assessments of the wave's rising time and magnitude were also performed, showing their strong influence on the caisson sliding.

Chapter 5 described the physical model tests for the impulsive wave generation, forces, and motions of the caissons, both regular and with horizontal rear plates. A numerical calculation was also conducted to investigate the reproducibility of the analytical method and the experimental wave generation. The influence of the plates on the caisson's sliding during physical tests was discussed, as well as the fit of the analytical models from further analysis of the resultant data from the wave-induced caisson sliding tests.

The study concluded that the current models for regular caissons sliding should not be applied to caissons with horizontal plates. The proposed model led to a good representation of the physical phenomenon, and although an increment in the added mass was seen, its influence on the sliding was reduced by the effect of the damping parameters. Furthermore, the horizontal plates were found to affect the sliding of the caisson breakwaters. Their impact was positive for plates at the surface, leading to sliding reductions, while the submersion negatively affected such parameters. On the other hand, increments of the plate length also had a good effect, decreasing the displacement of the caisson under the same conditions. However, their positive influence decreased for plates over two-thirds of the water depth. These and other findings were summarized in Chapter 6, responding to the research questions and providing recommendations for future investigations on the topic.

ACKNOWLEDGEMENTS

My most profound appreciation goes to my supervisors, Professor Dr. Shin-ichi Aoki and Professor Dr. Susumu Araki. To the first, for allowing me to proceed with postgraduate studies at Osaka University and for his valuable contribution and guidance throughout this project. To the second, for taking me in regardless of his new responsibilities' immense workload and for the always opportune advice. Sincere thanks to my program and laboratory colleagues for their support and genuine kindness, helping sustain a positive atmosphere in which to do science. My appreciation is extended to the Ministry of Education, Culture, Sports, Science and Technology of Japan (MEXT) for granting the scholarship that allowed this research.

To conclude, immeasurable thanks to my family and friends, whose value to me only grows with age and whose support has been essential at every step of my academic and personal life, especially when far from home.

TABLE OF CONTENTS

Chapter 1. INTRODUCTION

Chapter 2. LITERATURE REVIEW

Chapter 3. ANALYTICAL STUDY: THEORETICAL DESCRIPTION

Chapter 4. ANALYTICAL STUDY: PRACTICAL IMPLEMENTATION AND DISCUSSION.

Chapter 5. EXPERIMENTAL STUDY

Chapter 6. CONCLUSIONS

LIST OF FIGURES

LIST OF TABLES

LIST OF SYMBOLS

$\eta(x,t)$	Free water surface
t	Time
u,w	Velocity components (x, z directions)
$\varphi(x,z,t)$	Velocity potential (2D)
ρ	Fluid density
g	Gravitational acceleration
a	Wave amplitude
H	Wave height
k	Wave number associated with the progressive wave
k_n	Wave number associated with the evanescent wave
L	Wavelength
ω	Wave frequency
T	Wave period
h	Mean water depth
S	Wavemaker stroke
ξ, d	Wavemaker board displacement
F	Wave force
p	Pressure
m	Mass
M	Added mass
M_∞	Constant added mass
N	Damping coefficient
R	Memory effect function

F_{max}	*Maximum wave force*
F_s	Static frictional force
F_f	Dynamic frictional force. Used in the study as just frictional force
f_s	Static friction coefficient
f	Dynamic friction coefficient
α	Wave force magnitude or rising coefficient
t_p	Wave force rising time
h_s	Plate submersion distance
l	Plate length

Chapter 1. INTRODUCTION

1.1 BACKGROUND

Climate change is leading to an increase in the frequency and intensity of natural disasters and sea-level elevation, which threatens the stability of coastal protection structures. Furthermore, recent disasters have exposed the catastrophic damage to the land and port facilities that the destruction of such systems can cause. This fact implies that the loss of the structure's functionality influences the extent of damage in the area to be protected. Hence, evaluating the degree of functional deterioration of the structure at the time of failure ("performance at failure") is becoming essential.

Among coastal protection structures, vertical breakwaters have been widely utilized. Protecting the coastline, ports, and harbors from wave impacts, as well as beaches and navigation channels from sediment transport, are their most essential functions.

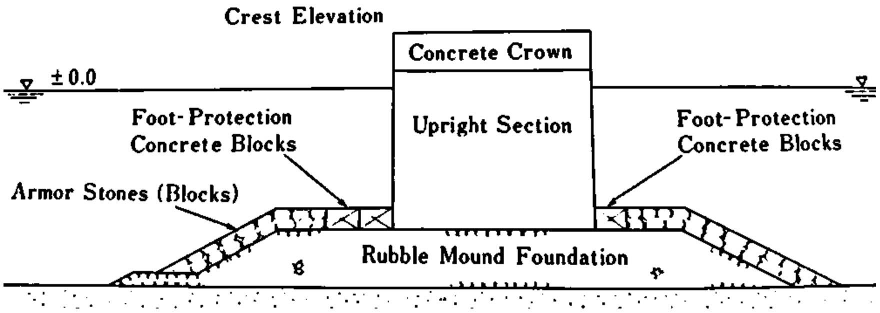

Figure 1.1. Idealized typical section of a vertical breakwater. (Goda, 1985)

There are different types of breakwaters. Vertical breakwaters, in particular, are generally composed of a superstructure usually formed by a deck and a parapet wall meant to reduce wave overtopping, a substructure built out of caissons, and a low rubble mound foundation acting as a buffer between the caisson and the seabed. An idealized typical section is shown in Figure 1.1, while a distinction according to the ratio of mound height to water depth h_b * (Allsop et al., 1999) is resumed in Table 1-1. Caissons are open reinforced concrete boxes, and the larger ones usually have partition walls, dividing them into inner cells to reduce the span length of the external walls. The inner cells are filled with different materials such as sand, rubble and/or concrete, which converts the caisson breakwaters into massive structures able to withstand and reflect significant waves actions.

Table 1-1. Distinction of breakwater type (Allsop et al., 1999)

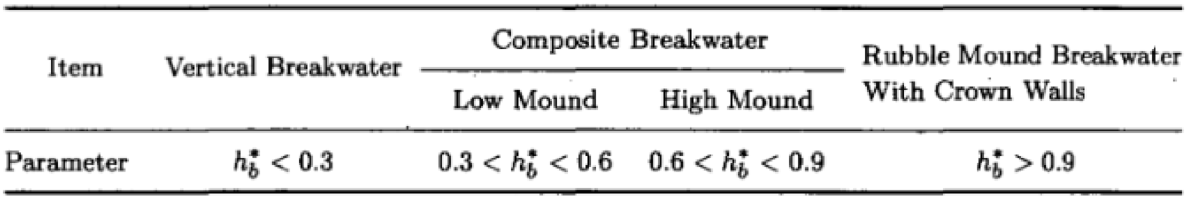

Item	Vertical Breakwater	Composite Breakwater		Rubble Mound Breakwater With Crown Walls
		Low Mound	High Mound	
Parameter	$h_b^* < 0.3$	$0.3 < h_b^* < 0.6$	$0.6 < h_b^* < 0.9$	$h_b^* > 0.9$

In Japan, thanks to the large inventory of such structures over the years, sliding has been proved as the prominent failure mode related to breakwater damage (Goda and Takagi, 2000). Also, due to a combination of increases in sea level and wave height, sliding distances of caisson breakwaters are expected to become five times greater than at present, according to Takagi et al. (2011). Caisson (upright part of the breakwaters) can maintain their functionality even if a limited amount of sliding occurs.

Table 1-2. Occurrence frequency of failure types of caisson breakwaters
(Goda and Takagi, 2000)

Most Frequency	**Failure type**
1	Sliding of the caisson.
2	Displacement of concrete blocks and large rubble stones armoring a rubble foundation mound
3	Breakage and displacement of armor units in the energy-dissipating mound in front of a caisson.
4	Rupture of front walls and other damage on concrete sections of a caisson.
5	Failure in the foundation and subsoil

Sliding is not generally allowed under traditional breakwater design. Its stability has been conventionally judged using safety factors, balancing external and resisting forces. However, deformation parameters such as the sliding distance directly indicate their stability. Some researchers have been proposing "deformation-based reliability" design methods, such as Aoki et al. (1995). In (Shimosako and Takahashi, 2000), a Level 3 Reliability design method (three levels of design methods for caisson breakwaters depending on the level of probabilistic concepts are employed) is also proposed. Furthermore, from such a viewpoint, a structure with the same failure limit may have different failure performance; thus, developing new structural shapes and devices is also pursued to improve performance at the time of failure, i.e., extending functionality.

From Figure 1.2 and Figure 1.3, the direct relation between breakwaters' loss of functionality and damage to the land area can be easily seen. The images correspond to Kamaishi City and Ofunato City in Iwate Prefecture, Japan. Those cities were affected by the 2011 Great East Japan Tsunami.

In Figure 1.2, the white shapes represent the caissons' location after the tsunami. In the case of Kamaishi City, some caissons from the north breakwater were displaced. The initial site can be easily defined since other caissons remained there even after certain displacement. In the center, where a straight white shape is displayed, caissons were not much affected. Similar behavior to that of the north but less destructive is also observed in the south. However, the discontinued black line in the Ofunato City image represents the initial location of the breakwater's caissons, showing that all caissons were displaced from their original position. That has a direct influence on the land damage seen in Figure 1.3. Among other factors, the tsunami impact on the land area was reduced where caissons remained partly or mostly in closer locations.

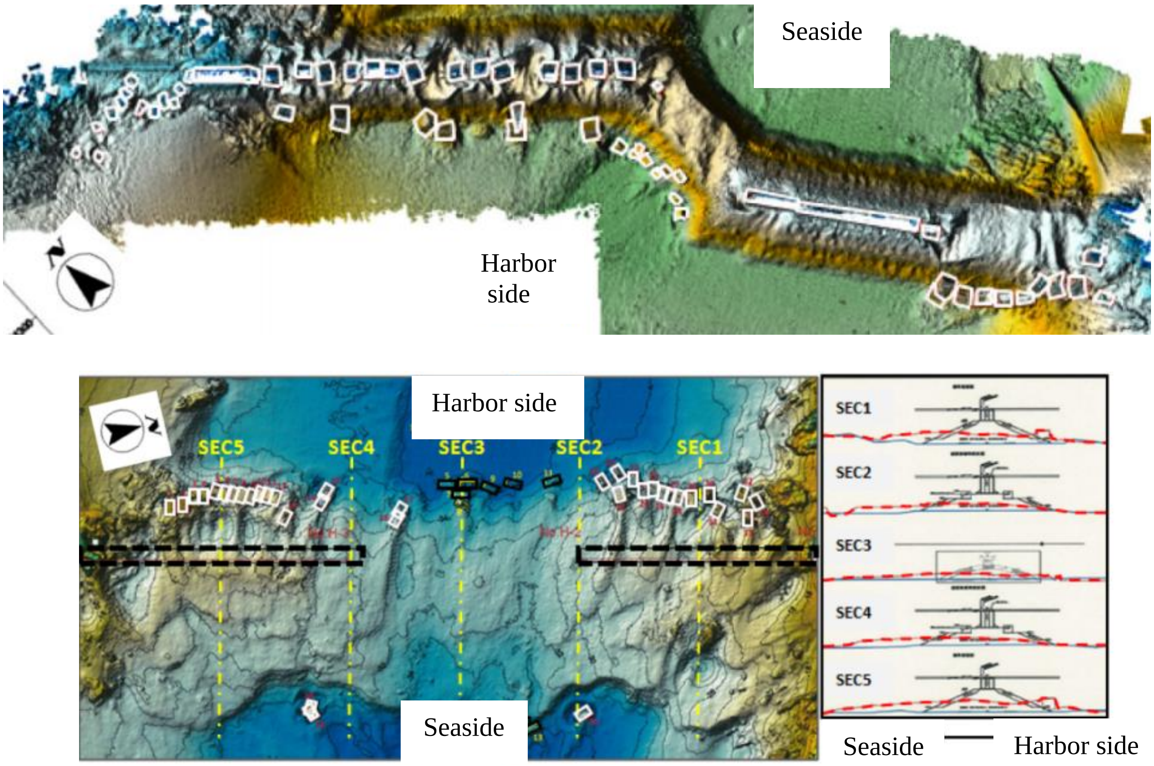

Figure 1.2. Breakwater damage in Kamaishi City (above) and Ofunato City (below) in Iwate Prefecture, Japan. June 2011. (Tomita et al.,2012)

Figure 1.3. Damage from the tsunami inundation in Kamaishi City with a maximum runup height of 11.7m (left) and Ofunato City with a maximum runup height of 10.9m (right) June 2011. (A. Suppasri et al.,2013)

The January 2024 earthquake and tsunami affecting the Noto peninsula in the southern part of the Sea of Japan and another earthquake a few months later in June at the same location remind us that the primary source of tsunamis and impulsive waves striking are more severe and frequent.

Figure 1.4. Aerial view of Iida Port before (left) and after (right) the damage to the eastern breakwater. Red circles indicate the position of the loss of the east breakwater (Sato T., 2024).

Iida Port in Suzu City was hit hard by the January earthquake measuring six on the Japanese seismic intensity scale. According to some reports, the eastern breakwater suffered noticeable damage due to the tsunami, as seen in Figure 1.4., leading to 4m wave heights that reached parts of the city at the time of the disaster (Nikkei Crosstech, 2024).

Figure 1.5. Damage to the east breakwater in Iida Port. Caisson collapsed and was submerged in the water. (Sato T., 2024).

In the center part, sections of caissons collapsed or were submerged in water, and wave-dissipating blocks were lost at the tip. Additionally, preliminary studies point out the breakwater damage was caused by either large waves overtopping or sliding due to the strong waves' impact. Interestingly, the last maintenance of the damaged areas was between 1980 and 1987, while the zones where more recent maintenance back in 2016 was performed showed almost no damage. Even though no tsunami warning was issued during the June event, a slight change in sea levels was detected. Reconstruction works should consider the maintenance and optimization of the current designs.

1.2 PROBLEM DEFINITION

Analysis of caisson breakwater failures, mainly in Japan and Europe (Takahashi et al., 2010), identified caisson sliding due to impulsive wave pressure as one of the most critical failure modes. On the other hand, the caisson's shape is directly related to the dynamics of the breakwater and its sliding distance against wave loads. Nevertheless, despite several theoretical models for the dynamics of caisson breakwater having been developed using different approaches, such as in (Aoki and Okube, 1995), (Shimosako et al., 2006), (Cuomo et al., 2011), and (Cozzutto et al.,2019), most of them are aimed at regular caissons. When new shapes need to be analyzed, the caisson dynamics are usually examined by physical tests. On this ground, modeling the dynamic behavior of non-regular caisson breakwaters would optimize the check for new structures before reaching experimental stages. That is the case of the rear horizontal plates, which were first analyzed by Yoshihara (2019) under the hypothesis that the plate would increase the inertial resistance of the structure. The plate addition showed a reduction of the sliding distance of around 20%, but it employed the same model used for regular caissons accounting only for the horizontal reaction forces.

Considering as much as possible the number of conditions is indispensable in modeling the phenomena accurately. For example, vertical hydrodynamic forces (uplift forces) might reduce the frictional resistant force, increasing sliding. Thus, the non-inclusion of the vertical force might lead to an overestimation of the positive influence of the horizontal plate on the caisson sliding reduction.

1.3 RESEARCH QUESTIONS

However, can the current simplified sliding models of regular caissons be applied when introducing new shapes, such as caissons with rear horizontal plates (non-regular caissons)? If the inertial resistance of the structure indeed increases due to the plates, what happens to the hydrodynamic parameters, and how do they affect the sliding simulation? Additionally, to what extent do the rear horizontal plates affect the total sliding of caissons, and what are the particularities for each analysis approach (analytical, numerical, and experimental) regarding such shapes?

The present research intends to contribute to the study of the caisson breakwaters' performance during the failure process by developing a reliable design method and describing the effectiveness of introducing horizontal plates to reduce the sliding motion of caissons. How does the introduction of vertical hydrodynamic force influence the effectiveness of the plate, and which plate length and submersion might be more efficient and practical to utilize, or if it is not needed at all, are the main questions to answer in this study. Identifying improvements and future research opportunities in caisson shape optimization will also expand the development of more tenacious structures, reduce the amount of sliding and the loss of functionality as long as possible, and achieve the final purpose of reducing damage to the coastal zones.

To respond to the above, a study on the effect of horizontal plates on the dynamic response and sliding caisson breakwaters is carried out and documented in this dissertation.

1.4 RESEARCH APPROACH

The present research centers on the sliding distance as a direct deformation parameter of the caisson's stability performance. As part of the fundamental research to enhance the accuracy of caisson motion models, an improved sliding model for regular caissons based on the application of the wavemaker theory and considering the uplift forces added to the system by the plates are developed, expecting to provide a better assessment of the effect of this element on the caisson sliding reduction. The model also includes using parameters related to the damping to account for the energy dissipation due to the presence of the plate. A methodology is established and applied to superficial and submerged single and multiple plates, simulating the dynamic behavior of the new caisson shapes to analyze later the effect of the plate length and submersion depth on the overall sliding of the structure. Furthermore, methods for a more practical, accessible, and faster analysis are applied to solve the boundary problems and estimate the hydrodynamic parameters since various shape variations might be studied in the future. Most of the models' development and application are computed in MATLAB.

Additionally, small-scale physical experiments are carried out for the regular and non-regular caisson shapes to confirm the response of the structures against impulsive waves generated by an experimentally first-tested method for generating concentrated waves at targeted locations. The sliding for each case is measured and compared in order to define the effect on the sliding of the different configurations. The best designs are expected to make the structure more tenacious, reduce the amount of sliding and the loss of functionality as much and long as possible, and achieve the final purpose of reducing the damage to the coastal zones.

The general description of the dissertation structure is as follows:

Chapter 2 examines actual failures of breakwaters due to impulsive pressures, reviews studies involving impulsive pressures from a caisson design viewpoint, their generation and estimation formulas, and past research on time-series load and sliding models for the evaluation of caissons' motion.

Chapter 3 describes the derivation of a model for caissons with horizontal plates (non-regular caissons) and the methodology to estimate the hydrodynamic coefficients of the dynamic response and the sliding for these structures.

Chapter 4 discusses the application of the models derived in Chapter 3. The influence of the plate geometric characteristics and arrangements on the pressures, the hydrodynamic parameters added mass (constant added mass) and damping coefficient (memory effect function), as well as the sliding of the caisson, are the objects of discussion. A discussion of the effect of the wave characteristics, such as rising time and magnitude, on the sliding is also included.

Chapter 5 describes the physical model tests for the impulsive wave generation, forces and motions of the caissons, both regular and with horizontal rear plates. Numerical calculations are also conducted to investigate the reproducibility of the analytical method and the experimental wave generation. The influence of the plates on the sliding of the caisson during the physical tests is discussed, as well as the fit of the analytical models from further analysis of the resultant data from the wave-induced caisson sliding tests.

Chapter 6 summarizes the conclusions of the study, responding to the objectives and research questions and providing recommendation points for future investigations on the topic.

Chapter 2. LITERATURE REVIEW

OUTLINE

For the development of this study, fundamental and more recent research related to caisson breakwater design is reviewed. Topics such as failure modes, documented vertical breakwater failures, and existing models for dynamics of caisson breakwater and for the wave loads leading to their failure are resumed in this chapter.

2.1 CAISSON BREAKWATERS. FAILURES

Most of the research related to caisson breakwater dynamics under wave loading focuses on observing damaged and failed structures. Surveying different cases allows for investigating the dynamics of the caissons by analyzing large data sets of responses from actual structures under natural physical phenomena.

As Takahashi et al. (2000) stated, the total length of Japanese breakwaters exceeds 800 km, with the major ones being caisson breakwaters, half of which are ordinary composite type and the other half mostly caisson breakwaters covered with wave-dissipating concrete blocks (Takahashi, 2000). This makes Japan the country with more breakwaters of this type, which, along with its tendency to be impacted by natural phenomena, leads to considerable accumulated knowledge and collected data on the behavior of such structures. Figure 2.1 displays a correlation of chains of main tsunami damage in caisson composite breakwaters (Raby et al., 2015) based on the manual of the National Institute for Land and Infrastructure Management (NILIM, 2013) of the Ministry of Land, Infrastructure, Transport and Tourism (MLIT) of Japan.

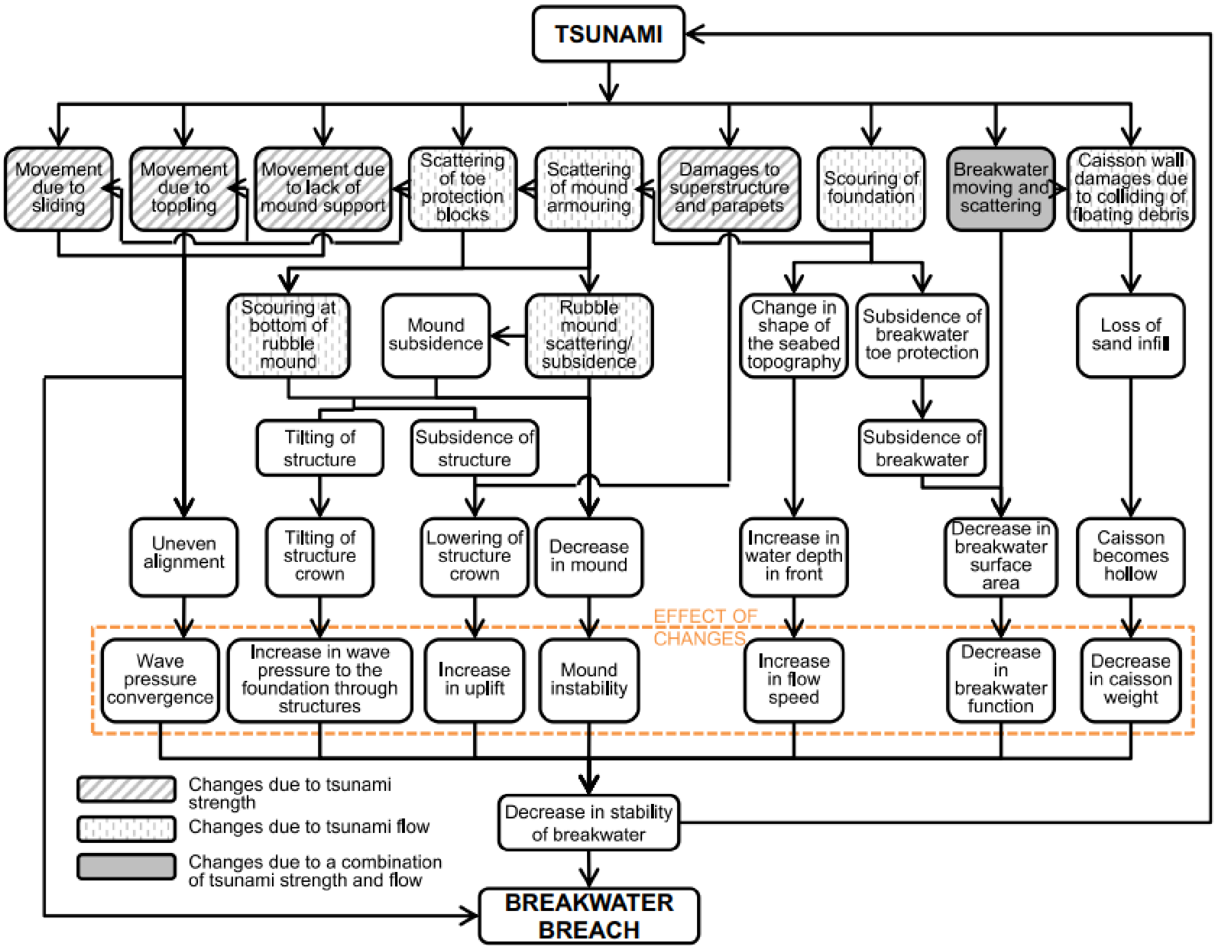

Figure 2.1. Correlation of chains of main tsunami damage in caisson composite breakwaters (Raby et al., 2015) based on (NILIM, 2013)

One of the most referred to research documenting the breakwater failures outside Japan is that by Franco (1991,1994) and Oumeraci (1994), summarizing the Italian experience between 1993 and 1991. The later included an extensive compilation of cases in Japan. In all cases, the collapse was found to be due to unexpected high wave impact loading, resulting from the underestimation of the design conditions and the wave breaking at the limited depth at the toe of the structure. Goda (1974) reported and analyzed multiple historical sliding-induced failures of vertical caisson breakwaters in Japan. At a similar time, Takahashi et al. (1993, 1998, 2000) discussed punctual caisson failures in 1973 and 1991 as well as results from an extensive field survey of Japanese breakwaters, later summarizing the caisson wall failures in the period 1977-1997, and also reported mayor failures taking place between 1983 and 1991. Goda and Takagi (2000) also summarized failure modes of vertical caisson breakwaters over several decades. After 2011, many reports and dedicated research, such as the one about the world record breakwater in Kamaishi by T. Arikawa et al.(2012). In most of the study and among other findings, the authors confirmed impulsive breaking wave pressure to be the leading cause of damage for caisson breakwaters, together with the collision of concrete blocks against the caisson walls. Additionally, they identified sliding of caissons and structural failures due to impulsive wave pressure as the most important failure modes for caisson breakwaters installed on a steep foreshore and subject to breaking wave attack.

2.2 CAISSON SLIDING MODELS

The concept of expected sliding distance (ESD) was proposed by Ito, Fujishima, and Kitatani (1966) in their research on the stability of breakwaters as the statistical value given as an average of caisson sliding distances (horizontal displacement) during the service lifetime of the caisson. However, the value itself was not estimated since assessing the wave pressure precisely at the time was difficult, hence the sliding distance. It was not until the Goda wave pressure formula (Goda,1974) and its amendments by Takahashi, Tanimoto and Shimosako (1993,1994b) that researchers started proposing models that consider calculating the sliding distance.

In Japan, Goda (1994) suggested modeling the dynamics of a composite breakwater as that of a rigid body suspended on a system of mass and dual springs for rotational and horizontal motions and using the momentum theory of impulsive breaking wave forces to estimate the sliding distance of the superstructure. Shimosako et al. (1994) presented a model for the caisson motion represented by Eq. (2.1) where $\boldsymbol{M_a}$ is the added mass, $\boldsymbol{F_R}$ is the frictional resistance force $\boldsymbol{F_R} =$

$\boldsymbol{\mu W' - U}$ ($\boldsymbol{\mu}$ been the friction coefficient, $\boldsymbol{W}$ the caisson weight, and $\boldsymbol{U}$ the uplift), and $\boldsymbol{F_D}$ is the force related sliding velocity including the wave-making resistance force.

$$\left(\frac{W}{g} + M_a\right)\ddot{x} = P - F_R - F_D \tag{2.1}$$

$\boldsymbol{P}$ represents horizontal wave force but establishes that the effective force producing caisson's sliding, that is the shear force at the caisson bottom $\boldsymbol{F_T}$ should be used instead of $\boldsymbol{P}$ in order to include the effect of dynamic response of caisson since, although the magnitude of impulsive pressure intensity is large, the shear force is significantly reduced due to the caisson's dynamic response. Furthermore, if wave pressure is not impulsive, the shear force equals the horizontal wave force (Shimosako et al., 1994). The study uses a triangular wave thrust for the analysis (wave loads models will be discussed later in the next section). The forces acting on the caisson when the sliding occurs are represented in Figure 2.2.

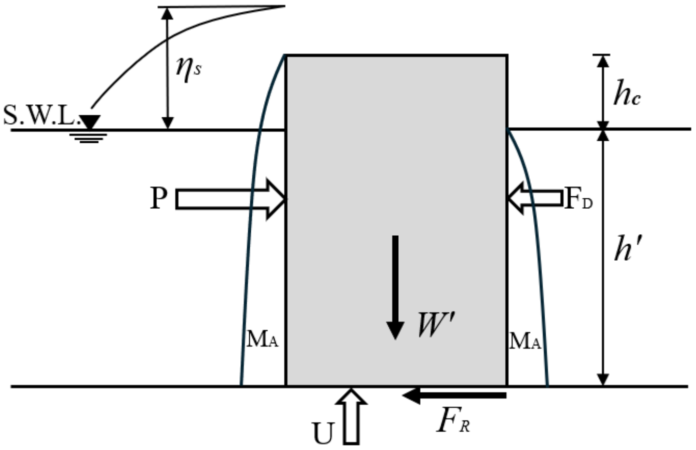

Figure 2.2. Forces acting on the caisson in sliding. Based on (Shimosako et al.,1994)

However, the simplified sliding model of Shimosako et al. (1994) assumed that the added mass $\boldsymbol{M_a}$ and $\boldsymbol{F_D}$ are small enough to be neglected, consequently, utilizing the below expression.

$$\left(\frac{W}{g}\right)\ddot{x} = F_T - \mu U - \mu W' \tag{2.2}$$

Aoki and Okube (1995) presented an arrangement as in Eq. (2.3) where $\boldsymbol{M}$ is the added mass, $\boldsymbol{N}$ is the damping coefficient and $\boldsymbol{F_f}$ is the frictional force. The model not only did account for the damping in the model, but adopted Cummins's (1962) impulsive response to express the damping in function of time $\boldsymbol{R}$ as in Eq. (2.4) and not as a unique coefficient.

$$(m+M)\ddot{x}+N\dot{x}=F(t)-F_f \tag{2.3}$$

$$(m+M_\infty)\ddot{x}+\int_0^t R(t-\tau)\dot{x}(\tau)d\tau=F(t)-F_f \tag{2.4}$$

Takahashi et al. (1994, 1998) investigated the dynamic response and the sliding through FEM models and presented a more sophisticated model accounting for non-linearities and evaluating cumulative sliding of caissons, but it was found to be complicated and time-consuming (Cuomo et al., 2011). Thus, Shimosako and Takahashi (1999) presented a simplified model for estimating the distance of caisson sliding $\boldsymbol{S}$ validated with data from small-scale physical model tests. It contemplates the effective caisson weight $\boldsymbol{W}$, friction coefficient $\boldsymbol{\mu_d}$, characteristics of the triangular wave thrust: duration $\boldsymbol{t_d}$ and peak value $\boldsymbol{F_{x,max}}$, and the uplift $\boldsymbol{F_{y,max}}$ exerted upon the caisson bottom (Shimosako and Takahashi, 1999).

$$S=\frac{t_d^2\left(F_{x,max}-F_{y,max}+\mu_d W\right)^3\left(F_{x,max}-F_{y,max}+\mu_d W\right)}{8\,\mu_d\,m_c\;W\left(F_{x,max}-F_{y,max}\right)^2} \tag{2.5}$$

The mentioned method was included in the performance-based design (Shimosako and Takahashi, 1999) and reliability design (Goda and Takagi, 2000; Kim and Takayama, 2003) methods for caisson breakwaters.

Models for the dynamics of caisson breakwaters have continuously improved, trying to reproduce more features of the caisson dynamics. Sliding, tilting, and more and better representations of the interaction structure-foundation have been gradually included since the middle of last century. Nevertheless, more comprehensive research has been focusing on sliding, especially since the introduction of performance-based reliability design proposals based on the expected sliding distance of caissons. However, most of the sliding models did not allow for the representation of the effect of the variation in time of the loading. Among those alternative models, one of the first ones from Loginov (1962 and 1969) is included in the Russian guidelines for evaluating the loadings and their effects on maritime structures and compiled in Marinski and Oumeraci (1992). The model combines swaying and rotating motions of the caisson in two rocking motions around two separate centers (located respectively above and below the center of gravity of the caisson) and neglects the effect of damping (Cuomo et al., 2011).

Takahashi et al. (1994) used a full-dynamic FEM to account for it, but it was not implemented since it was not suitable for the performance design (Cuomo et al., 2011). The simplified models for the dynamic behavior of caisson breakwaters developed by Oumeraci et al.(1992) and improved by Oumeraci and Kortenhaus (1994) attempted to quantify the relative importance of the applied dynamic load and the dynamics (mass, stiffness and damping) of the breakwater (including the superstructure, its foundation soil and the surrounding water) on the overall dynamic response of the system as a whole. The equation of motion in the study is as in Eq.(2.6), where a dot denotes differentiation with respect to time, ***M***, ***C*** and ***K*** are, respectively, the mass, the damping and the stiffness matrixes at two degrees of freedom. The vector ***u*** is composed of the displacement along ***x***, and the rocking ***θ*.**

$$M.\ddot{u}(t) + C.\dot{u}(t) + K.u(t) = F(t) \tag{2.6}$$

M included horizontal and rotational hydrodynamic mass, while the damping coefficients were obtained experimentally by means of pendulum tests on the caisson breakwater model (Oumeraci et al. 1992). Cuomo et al. (2011) used a non-linear 3D model based on Oumeraci and Kortenhaus (1994) and included a coupling between the dynamic response and the bearing capacity of the soil. The model also considered the horizontal and rotational hydrodynamic mass as part of ***M*,** while damping and stiffness were determined by expressions related to the properties of the soil foundation.

2.3 WAVE IMPACT MODELS

As stated in the revision of caisson breakwater failures, various studies identified sliding of caissons and structural failures due to impulsive wave pressure as the most important failure modes for caisson breakwaters. Thus, such wave types are reviewed in the present section.

2.3.1 *Impulsive loads*

An impulsive pressure is exerted on a vertical wall when an incident wave begins to break in front of the wall and collides with it, having the wavefront almost vertical. The impinging wave loses its forward momentum in the short time during which the collision takes place. The forward momentum is converted into an impulse which is exerted on the vertical wall. This pressure may rise to more than ten times the hydrostatic pressure corresponding to the wave height, though its duration will be very short. Such an abnormally high breaking wave pressure is called an impulsive (breaking wave) pressure (Goda, 2000). Two types of impulsive pressures are defined: Wagner and Bagnold-type pressures. The former does not entrap an air layer, while the latter does. The magnitude of impulsive pressure intensity is quite large, being several times the ordinary wave pressure. However, the effective pressure for caisson sliding is greatly reduced due to the caisson's dynamic response.

Furthermore, it is pointed out that the best countermeasure against impulsive pressures is the design prevention of dangerous conditions by determining the impulsive pressure coefficients. At the same time, other solutions currently involve using alternative breakwater structures, such as a composite breakwater covered in front with wave-dissipating concrete blocks or perforated wall caisson breakwaters. According to a study of impulsive pressures on a caisson of composite breakwater by Shimosako et al. (1993) and after reviewing actual failures of composite breakwaters due to impulsive pressures, the failure of the caisson due to impulsive pressure is characterized by small but steady sliding of the caissons.

Additionally and for easier general understanding, Figure 2.3 distinguishes between the impact loads for which the load duration and time history are most relevant for the dynamic response of the structure and which, therefore, need to be handled with special care and the pulsating wave loads for which the expected response of the structure is such that quasi-static approaches might apply (PROVERBS - Oumeraci et al., 1999).

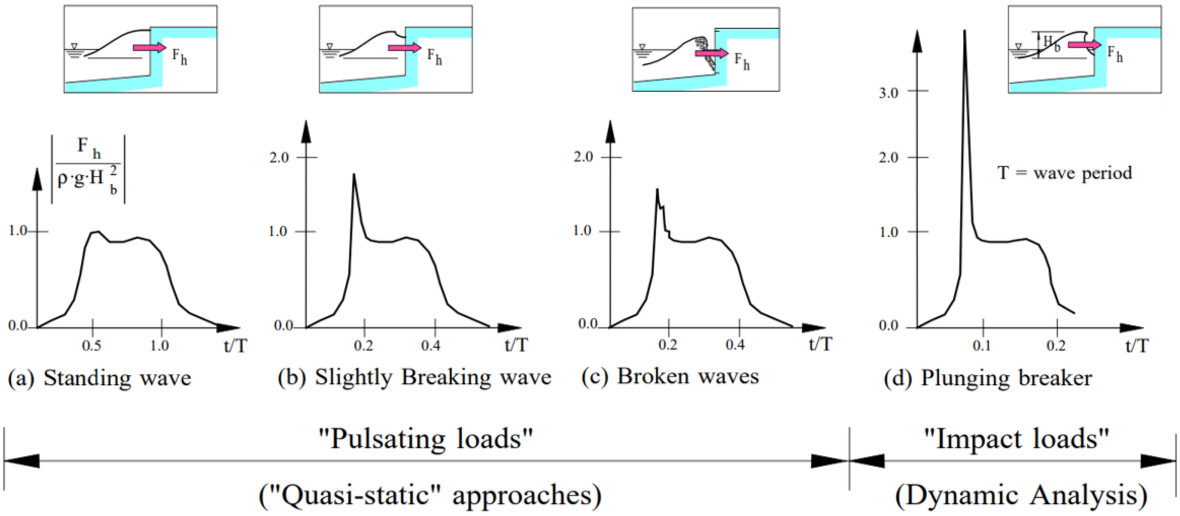
(a) Standing wave
(b) Slightly Breaking wave
(c) Broken waves
(d) Plunging breaker

Figure 2.3. Distinction of loads type and approaches (PROVERBS - Oumeraci et al., 1999)

2.3.2 *Time- series Wave Loads on Caisson Breakwaters*

According to Takayama and Fujii (1991), the most influential uncertain factors in the caisson motion simulations are the empirical formula of wave force and the friction factors used. Therefore, besides utilizing a correct friction factor (0.6 being the accepted for concrete caisson on rubble mounds), selecting the time-history load that better represents the study case is primordial.

An example of a dimensionless time-series load applied by a breaking wave on the seaward face of a vertical breakwater during physical experiments (Cuomo, 2007) is plotted in Figure 2.4 alongside a superimposed idealized load history. Non-dimensionalization of pressure and time is done by water density ρ, gravity acceleration constant g, and significant wave height H_s and period T_m, respectively.

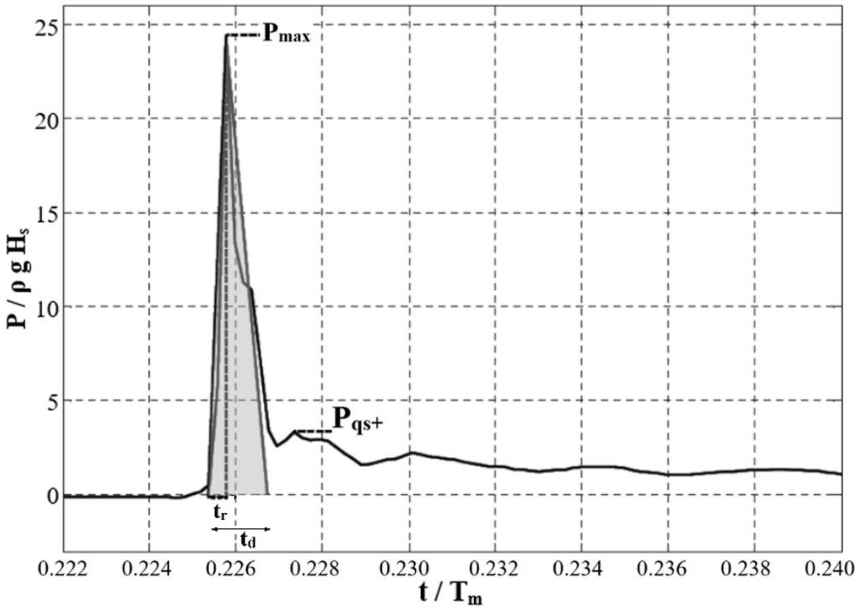

Figure 2.4. Wave-impact history load recorded during physical model tests (Cuomo, 2007)

The load model simulates a triangular spike characterized by a maximum reached during loading (P_{max}), the time needed to get to P_{max} from 0 called rising time (t_r) and back to 0 the duration time (t_d). The grey-colored area is related to the impulse, which is the moment transferred to the structure during the wave impact. Such impact is more violent, corresponding to shorter rising times and vice versa. Furthermore, passing P_{max} and before reaching 0, the force passes through a lower magnitude (P_{qs+}) with slow variation and long duration compared to the impulse peak. Following the pattern of the wave pressures, simplified time-series loads are proposed for use in the evaluation of caisson breakwater displacements. Most simplified models then assume a triangular time-history of wave thrust variation with a short duration. The existing load time series in the reviewed literature are summarized in Table 2-1.

Table 2-1. Summary of existing wave time-history loads for use in the dynamic analysis of caisson breakwaters. A modified version of the summary by Cuomo et al.(2011)

Reference	Time series scheme	Time series equation
Lundgreen(1969)	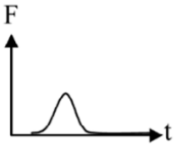	$max\left\{\frac{F_{max}}{2}\left[1-\cos\left(\frac{\pi t}{t_r}\right)\right];0\right\}$
Goda (1994)	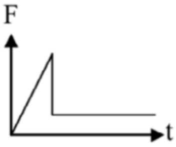	$F_{max}\frac{t}{t_r}$ for $t < t_r$ $(F_{qs^+})\frac{t}{t_r}$ for $t \geq t_d$
Oumeraci and Kortenhaus (1994)	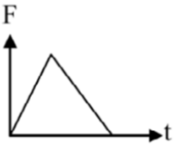	$F_{max}\frac{t}{t_r}$ for $t < t_r$ $F_{max}\left(\frac{t_d-t}{t_d-t_r}\right)$ for $t_r < t < t_d$ 0 for $t \geq t_d$
Shimosako et al. (1994)	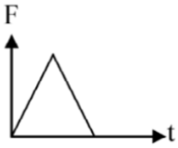	$F_{max}\frac{t}{t_r}$ for $t < t_r$ $F_{max}\left(2-\frac{t}{t_r}\right)$ for $t_r < t < 2t_r$ 0 for $t \geq 2t_r$
Aoki and Okube (1995)	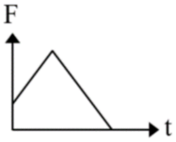	$\frac{\alpha F_s}{t_r}t + F_s$ for $t < t_r$ $-\frac{\alpha F_s}{t_r}t + (1+2\alpha)F_s$ for $t \geq t_r$
Shimosako and Takahashi (1999)	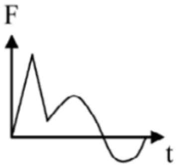	$max\left\{F_{max}\frac{t}{t_r};(F_{qs^+})sin\left(\frac{2\pi}{T_i}t\right)\right\}$ for $t < t_r$ $max\left\{F_{max}\left(2-\frac{t}{t_r}\right);(F_{qs^+})sin\left(\frac{2\pi}{T_i}t\right)\right\}$ for $t_r < t < 2t_r$ $(F_{qs^+})sin\left(\frac{2\pi}{T_i}t\right)$ for $t \geq 2t_r$
Oumeraci et al. (2001)	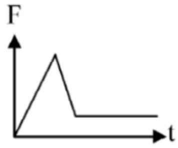	$F_{max}\frac{t}{t_r}$ for $t < t_r$ $F_{max}\left(\frac{t_d-t}{t_d-t_r}\right)$ for $t_r < t < t_d$ F_{qs^+} for $t \geq t_d$

For most of the equations in Table 2-1, parameters such as the quasi-static seaward force $\boldsymbol{F_{qs+}}$ are determined by the original formulation of Goda's method (Goda,1974) since it was proposed for ordinary vertical breakwaters, while the estimation of the maximum wave force or impact maximum F_{max} and the time components follows the formulation in each related reference. The model by Shimosako and Takahashi (1999) is the most sophisticated and has been adopted in Japan as a basis for the sliding caisson breakwater (Cuomo et al., 2011). However, small-scale experimental investigations by Kim and Takayama (2004) highlighted that the time-history model largely overestimates the wave force in the standing wave part of the Shimosako and Takahashi model, while its estimation for the impulsive part comparatively agrees with the experimental data. Thus, Oumeraci et al. (2001) simplified the standing part to a constant value. Among the models, the proposed by Shimosako et al. (1994) includes impulsive and pulsating (positive for landward and negative for seaward) forces, while Aoki and Okube's (1995) is based on the former, but it considers the sliding for all simulation cases. This is accounted for by considering the starting point of the load time-series not for a null force but for the static frictional force F_S, which is the load necessary to move the caisson considering its weight and the friction coefficient between the caisson bottom and the foundation. It also utilizes a parameter α to consider how much the maximum force exerted to the caisson exceeds the static frictional force. The consideration of rising and duration time is then viewed from the reference.

For practical reasons, the triangular pulse described by the rise time t_r and the total duration of the force t_d as discussed above, represents a reasonable choice since the triangular shape is derived from the actual force history based on the equivalence of breaking wave momentum and force impulse.

Furthermore, when doing small-scale experiments, some scaling problems in the impulsive part of the wave are expected due to the possible compressions of air pockets and the impact of breaker tongues, as well as due to the oscillations of air pockets or air scape in the quasi-static part (PROVERBS - Oumeraci et al., 1999). This can partially be adjusted by using the corrections in Figure 2.5.

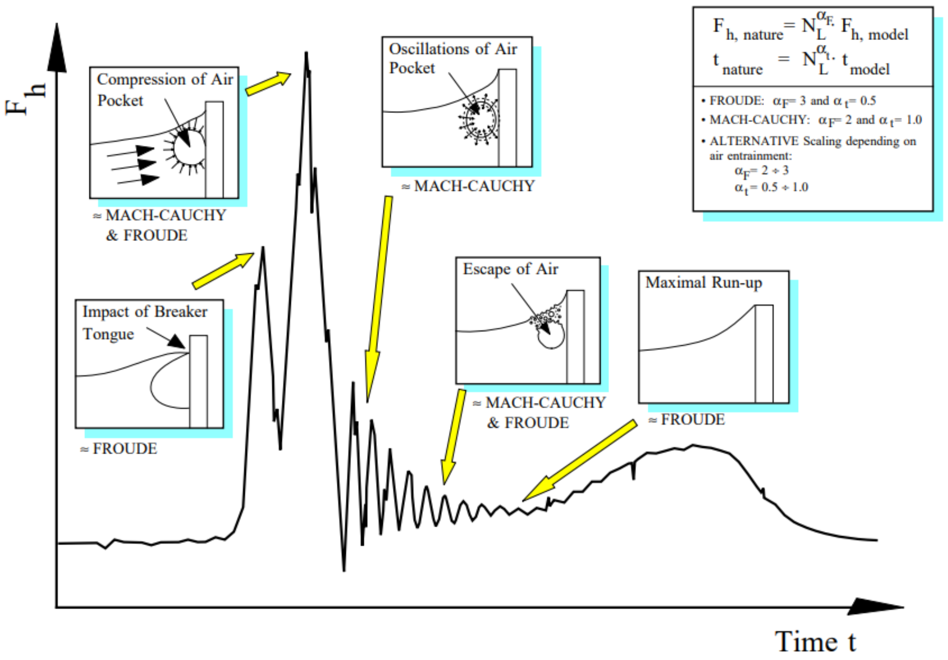

Figure 2.5. Physical processes involved in the wave load history and associated scaling problems (PROVERBS - Oumeraci et al., 1999)

2.3.3 *Prediction Methods for Wave Impact Loads on Vertical Walls*

The maximum wave force is an essential parameter for wave models; thus, estimating its magnitude has been at the center of research since the last century. Among the design methods that include forces of the wave loading is Sainflou (1928) for the vertical wall without berm; thus, no uplift is considered, but it is challenging to implement. Goda (1985), the most widely used design method, considered pressures, forces and uplift. However, these two are related to quasi-static waves.

Reviewed models accounting for impact waves started appearing in the early works of Hiroi (1920), followed by Minikin (1963) that developed a prediction formula that has been proven to be sometimes incorrect (Allsop et al., 1996) (PROVERBS - Oumeraci et al., 1999) overestimating the wave force, but it is still recommended in the Coastal Engineering Manual thus used in design practice in United States; while Takahashi et al. (1994) extended the Goda model to also described impact waves. Later, time-dependent approaches started to be developed as in Oumeraci and Kortenhaus (1995), followed by amendments as part of the European PROVERBS project (PRObabilistic design tools for VERtical Breakwaters)by McConnell (1998), Hull and Müller(1998), and Vicinanza (1998).

The Goda formula was extended to include the incident wave direction (Tanimoto, 1976), modification factors applicable to different vertical wall types, and impulsive pressure coefficients (Takahashi et al., 1994). That and the whole prediction method by Goda (2020) represent a landmark in the evolution of more developed approaches to assessing wave loads at walls. It has been included in various international standards, including those in Japan. The extension of coefficients and the notoriety are not covered here, but it is a necessary review. Another prediction method for wave impact forces in vertical breakwaters included or recommended in standards such as the British Standards (BS6349-1 and BS6349-2, 2000) is that from Allsop et al. (1996) and Allsop and Vicinanza(1996) and which was also recommended by Oumeraci (2001).

Table 2-2. Examples of wave impact forces used in standards.

Reference	Expression for maximum impulsive pressure/force
Minikin (1963)	$F_{H,imp} = \frac{101}{3}\rho g H_D^2 \frac{d}{L_D D}(d + D)$
Allsop and Vicinanza(1996)	$F_{H,imp} = 15\rho g d^2 \left(\frac{H_{si}}{d}\right)^{3.134}$
Goda (2000)	$P_{I(\max)} = \frac{\pi \rho g C_b {H_b}^2}{4 g \tau}$ $F_{H,imp} = 15\rho g {H_b}^2$ [*]

In Table 2-2, three examples of expressions used in predicting wave impact forces used in international standards, as mentioned before, are showcased. In the Minikin formula, $\boldsymbol{H_D}$ and $\boldsymbol{L_D}$ are the design wave height and length, respectively; $\boldsymbol{D}$ is the water depth at a distance $\boldsymbol{L_D}$ from the structure, and $\boldsymbol{d}$ is the water depth at the toe of the structure. For Allsop and Vicinanza's expression, $\boldsymbol{H_{si}}$ is the design wave height, and $\boldsymbol{d}$ is the water depth. Goda’s method relies on several formulae with parameters and coefficients. However, Goda (2000) presents the $\boldsymbol{P_{I(max)}}$ for the peak value of the impulsive pressure, where $\boldsymbol{H_b}$ and $\boldsymbol{C_b}$ are the wave’s height and speed. Data collected from small experiments where then used to determine a minimum value for the impulsive duration of ($\pi \boldsymbol{C_b}$ /g60), yielding to the expression with the asterisk.

Chapter 3. ANALYTICAL STUDY: THEORETICAL DESCRIPTION

OUTLINE

The initial approach followed in this study is the development of the analytical models corresponding to the sliding of the new shape breakwaters: caissons with a single submerged horizontal plate, including the particular case with the plate at the surface, and caissons with multiple plates considering the variation of plate(s) lengths and submersion depths. In this chapter, the fundaments of the theoretical framework used to build the models, such as linear wave and wavemaker theories, sliding simulations for regular breakwater caissons, and methods for boundary value problem solutions, are discussed first. The methodology to determine the sliding for the different cases and the solution for the linear waves in each case are then presented. The physical characteristics of those solutions, such as velocity potential, pressures, forces, added masses, damping coefficients, and memory-effect functions used within it, are derived, as well as the final sliding model for the study cases.

3.1 THEORETICAL BACKGROUND AND DESCRIPTION

The theoretical description of a methodology to determine the sliding for a breakwater with a horizontal plate is displayed in this chapter by introducing and deriving velocity potential, pressure, force, added mass, damping coefficient, and memory-effect function formulations. The base theories and methods for applying the methodology [linear wave and wavemaker theories and the sliding simulation for regular breakwater caissons introduced by Aoki et al. (1995)] are presented as well. Furthermore, a practical method (Yoshida et al.,1990) called the Boundary-Point Selection Method is introduced in the velocity potential calculations that simplify analytical formulations and computing processing time. Applying such a method leads to the analytical solution of the presented boundary value problem.

3.1.1 *Linear Wave Theory*

[Enhanced subsection based on the previous work of the author in Fundora (2021)]

Linear wave theory (L.W.T) is one of the simplest water wave theories introduced in the 19th century due to the application of linearization techniques to the fluid governing equations and boundary conditions, conveying a simplified version of them, and is still widely used. A list of the simplifications and approximations can be summarized as: a) Constant water depth $\boldsymbol{h}$, b) Periodic waves with period $\boldsymbol{T}$, c) Considerations restricted to the 2D vertical plane ($\boldsymbol{x}$, $\boldsymbol{z}$), d) Neglection of viscous (and turbulent) stresses so the motion becomes irrotational. e)Assumption that the wave height $\boldsymbol{H}$ is much smaller than the wavelength $\boldsymbol{L}$.

Each of these assumptions contributes to simplifying the problem, but only the last two are approximations (Svendsen, 2006). The resulting wave solution has been called “small amplitude waves”, “infinitesimal waves”, “sinusoidal waves” or ‘linear waves”. The latter is used in this study. In some fields, they are also referred to as “Airy waves” or “first-order Stokes waves” because G.B. Airy(1845) derived the first expressions describing these waves, and G.G. Stokes (1846) derived the higher-order theory.

The theory uses a potential flow (flows that can be described with the velocity potential) approach to define the motion of waves on a fluid (water) surface and assumes an inviscid, incompressible, and irrotational fluid flow. Here is a simple explanation of such an ideal fluid: it is considered inviscid when its viscosity is zero, i.e., there is no internal friction or resistance to flow; incompressible when it has constant density under different pressures, meaning that its volume remains unchanged; and irrotational when there is no vorticity, i.e., the fluid particles do not rotate around their axes and keep their movement orientation. These assumptions on the fluid properties are significant since they allow for simplifying the mathematical description of the fluid dynamics; potential functions can describe the flow, and governing equations can be simplified.

L.W.T is mainly limited to conditions where the wave height ***H*** is small compared to the water depth ***h*** (in shallow waters) and to the wavelength ***L*** (in deep waters). The free surface elevation ***η(x,t)*** is sinusoidal and a function of the horizontal position *x* and the time *t*. Such a water surface profile is one of the desired final solutions. The ***(x,z)*** are cartesian coordinates with ***z***=0 at the still water level and positive upwards, and the sinusoidal progressive wave propagates in the positive ***x***-direction. A representation of essential wave characteristics is displayed in Figure 3.1. Table 3-1 lists the wave parameters related to it and others necessary to determine the solution.

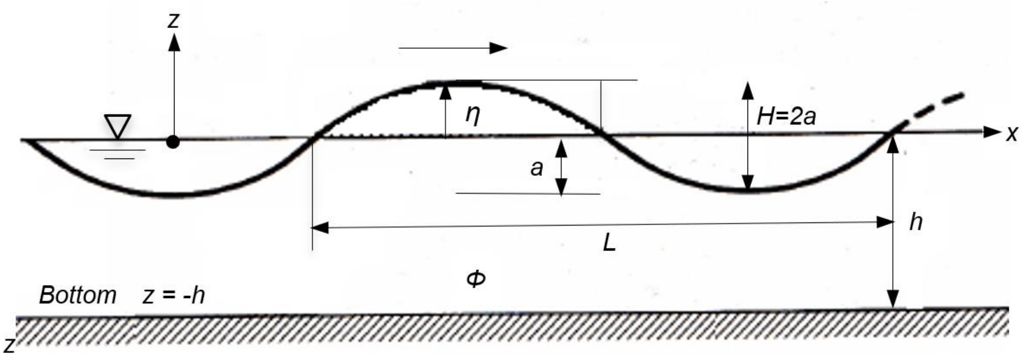

Figure 3.1. Wave characteristics. Linear Wave Theory.

Table 3-1. Parameters related to linear wave theory and their symbols.

Parameter	Symbol	Parameter	Symbol
Free water surface	$\eta(x,t)$	Wave amplitude	$a = H/2$
Time	t	Wave height	H
Velocity components (x, z directions)	u,w	Wave number	$k = 2\pi/L$
		Wavelength	L
Velocity potential (2D)	$\varphi(x,z,t)$	Wave frequency	$\omega = 2\pi/T$
Fluid density	ρ	Wave period	T
Gravitational acceleration	g	Mean water depth	h

Hydrodynamics fundamental equations are derived from the conservation laws of physics: mass, momentum, and energy conservation. For example, Eq. (3.1) is the two-dimensional Laplace equation or continuity equation for the cartesian system presented above. It expresses the conservation of mass for potential flows and provides a partial differential equation as the governing equation to be solved for the scalar function ***Φ*,** which is called velocity potential.

$$\nabla^2\Phi \equiv \frac{\partial^2\Phi}{\partial x^2} + \frac{\partial^2\Phi}{\partial z^2} = 0 \tag{3.1}$$

To understand the velocity potential more, let's recall vector analysis. According to its formulae, for an arbitrary scalar function $\boldsymbol{\Phi}\ (\boldsymbol{x}, \boldsymbol{t})$, an identity of $\boldsymbol{\nabla} \times \boldsymbol{\nabla\Phi} = 0$ (rot grad $\boldsymbol{\Phi} = 0$) holds. Therefore, if $\boldsymbol{\nabla} \times \boldsymbol{u} = 0$ is satisfied, the velocity vector $\boldsymbol{u}$ can be represented as $\boldsymbol{u} = \boldsymbol{\nabla\Phi}$ in terms of a scalar function $\boldsymbol{\Phi}$ (the velocity potential), and flows that can be described with the velocity potential are referred to as potential flows. Introducing the velocity potential may initially seem an unnecessary complication, but it is advantageous in mathematical development. The velocity is a vector quantity with three unknown scalar components, whereas the velocity potential is a single scalar unknown from which all three velocity components may be computed (Kashiwagi, 2018). Thus, the solution of incompressible, inviscid, irrotational flow requires the solution of Laplace's equation for two dimensions as in Eq.(3.2), where $\boldsymbol{u}$ and $\boldsymbol{w}$ are the horizontal and vertical velocity components, respectively.

$$\frac{\partial u}{\partial x} + \frac{\partial w}{\partial z} = 0 \tag{3.2}$$

The flow is also determined by the boundary conditions. For this problem, the kinematic condition at the bottom and the linearized kinematic and dynamic condition at the water surface are as in Eqs. (3.3), (3.4) and (3.5), respectively. For further details, including basic equations of the wave theory and their derivation to linearized forms, as well as velocity potential formulations, reference is made to Svendsen (2006).

$$\frac{\partial \Phi}{\partial z} = 0 \qquad at\ z = -h \tag{3.3}$$

$$\frac{\partial \Phi}{\partial z} = \frac{\partial \eta}{\partial t} \qquad at\ z = \eta \tag{3.4}$$

$$\frac{\partial \Phi}{\partial t} + gz = 0 \qquad at\ z = \eta \tag{3.5}$$

The solution for the potential function (velocity potential and water surface elevation) satisfying the two-dimension Laplace's equation and subject to the boundary conditions is:

$$\Phi(x, z, t) = \frac{ag}{\omega} \frac{\cosh k(z+h)}{\cosh kh} \sin(kx - \omega t) \tag{3.6}$$

$$\eta(x, t) = a \cos(kx - \omega t) \tag{3.7}$$

The velocity potential and water surface elevation on the ***x-z*** vertical plane are usually utilized in a complex form, as in Eq. (3.8) and Eq.(3.9). Furthermore, the solution to Eq.(3.9) is meaningful as long as the wave number satisfies Eq. (3.10) denominated as the dispersion relation.

$$\begin{aligned} \eta(x, t) &= a \cos(kx - \omega t) = a \cos(-kx + \omega t) \\ &= a e^{i(-kx+\omega t)} \quad = a e^{-ikx} e^{i\omega t} \end{aligned} \tag{3.8}$$

$$\Phi(x, z, t) = -\frac{ag}{i\omega} \frac{\cosh k(z+h)}{\cosh kh} e^{-ikx} e^{i\omega t} \tag{3.9}$$

$$\omega^2 = gk \tanh kh \tag{3.10}$$

Once the velocity potential is known, velocity components of the flow ***u***, ***w*** can be obtained from the derivation of Laplace's equation for irrotational flow. Moreover, by integrating the velocity potential with the momentum equation for inviscid fluid as in Eq.(3.11), the unsteady Bernoulli equation (3.12) is obtained. Finally, the pressure ***p*** equation (3.13) can be arranged from Eq.(3.12) for more clarity. Bernoulli's pressure equation is obtained from the conservation of momentum.

$$\frac{D\vec{v}}{Dt} = -\frac{1}{\rho}\nabla p + \vec{x} \qquad \text{where } \vec{v} = \nabla\Phi, \vec{x} = (0, -g) \tag{3.11}$$

$$\frac{\partial\Phi}{\partial t} + \frac{1}{2}q^2 + \frac{p}{\rho} + gz = 0 \qquad \text{where } q^2 = u^2 + w^2 = \left(\frac{\partial\Phi}{\partial x}\right)^2 + \left(\frac{\partial\Phi}{\partial z}\right)^2 \tag{3.12}$$

$$p = -\rho\frac{\partial\Phi}{\partial t} - \frac{1}{2}\rho q^2 - gz \tag{3.13}$$

3.1.2 *Wavemaker Theory.*

In the solution of boundary value problems of velocity potential, the most straightforward application might be the wavemaker theory. Classical wavemaker theory assumes that the water volume displaced by a board with sinusoidal motion in a 2D flume equals the crest volume of the propagating wave. There are flap-type and piston-type wave generators, and the latter is used in this study. For a piston-type wave generator (board) with a full stroke ***S***, the water volume ***V*** displaced by the board is expressed by Eq.(3.14), where *h* is the water depth. The water volume elevated by the motion of a wave with height ***H*** and wave number **k** = 2***π***/**L** can be estimated by Eqs. (3.14) and (3.15).

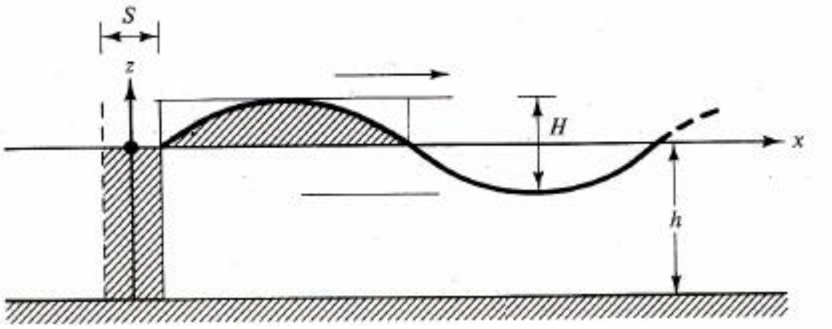

Figure 3.2. Wave generation by a piston-type generator. Based on Galvin (1964)

$$V = Sh \tag{3.14}$$

$$V = \int_0^{L/2} \frac{H}{2}\sin kx\, dx = \frac{H}{k} \tag{3.15}$$

$$\frac{H}{S} = kh \tag{3.16}$$

The ratio between wave height **H** and the stroke **S** as a function of **kh** can be obtained by equating Eqs. (3.14) and (3.15). Such relation implies that for large wave numbers **k**, i.e., for short wave periods **T**, larger wave heights are generated. The relation stated in Eq. (3.16) might appear simple; however, it has many applications. Nonetheless, the problem arises when trying to obtain an accurate value of **H** and when considering not only the progressive wave but also other components.

3.1.2.1 Velocity Potential

The wavemaker theory is used in the resolution of boundary value problems of velocity potential. The general equation of velocity potential is expressed by:

$$\Phi(x,z,t) = \phi(x,z)e^{i\omega t} \tag{3.17}$$

The exact solution of the generated wave's velocity potential **ϕ *(x,z)*** is expressed as Eq.(3.18). The first term of the equation is associated with a progressive wave (or propagating mode), and the second term with a spatially decaying standing wave (or evanescent mode).

$$\phi = A\cosh k\,(z+h)e^{-ikx} + \sum_{n=1}^{\infty} B_n \cos k_n(z+h)e^{-k_n x} \tag{3.18}$$

Where **A** and **B_n** are unknown constants and **k** and **k_n** are the wave numbers that satisfy the relations in Eq.(3.19). The first equality is the linear dispersion relation. The wave numbers can be obtained by rewriting Eq.(3.19) in a dimensionless form with the parameter $\frac{\omega^2 h}{g}$ as in Eq.(3.20) that yields to a direct or a Newton-Raphson iteration.

$$\omega^2 = gk\tanh(kh) = -gk_n\tan(k_n h) \tag{3.19}$$

$$\frac{\omega^2 h}{g} = kh\tanh(kh) = -k_n h\tan(k_n h) \tag{3.20}$$

Considering the oscillating board located at **x** = 0, its motion is expressed by Eq.(3.21) and the kinematic boundary condition on the board given by Eq.(3.22):

$$\xi(z,t) = \xi_o(z)e^{i\omega t} \tag{3.21}$$

$$\left.\frac{\partial\phi}{\partial x}\right|_{x=0} e^{i\omega t} = \frac{d\xi}{dt} = i\omega\xi e^{i\omega t} \tag{3.22}$$

This indicates continuity of velocity and yields to:

$$-ikA\cosh k\,(z+h) - \sum_{n=1}^{\infty} k_n B_n \cos k_n(z+h) = i\omega\xi_0(z) \tag{3.23}$$

To obtain the expression of the unknown constants ***A*** and ***B$_n$***, orthogonality properties of functions are utilized on the terms $\cosh k(z+h)$ and $\cos k_n(z+h)$, respectively. For example, ***A*** is determined by integrating Eq.(3.23) over the region $-h \le z \le 0$ after multiplying $\cosh k(z+h)$.

$$-ikA\int_{-h}^{0}\cosh^2 k(z+h)dz = i\omega\int_{-h}^{0}\xi_0(z)\cosh k(z+h)dz \tag{3.24}$$

Thus,

$$\begin{aligned} A &= -\frac{\omega}{k}\frac{\int_{-h}^{0}\xi_0(z)\cosh k(z+h)dz}{\int_{-h}^{0}\cosh^2 k(z+h)dz} \\ &= -\frac{4\omega}{\sinh 2kh + 2kh}\int_{-h}^{0}\xi_0(z)\cosh k(z+h)dz \end{aligned} \tag{3.25}$$

While for the evanescent mode waves, ***B$_n$*** is given as:

$$\begin{aligned} B_n &= -\frac{i\omega}{k_n}\frac{\int_{-h}^{0}\xi_0(z)\cos k_n(z+h)dz}{\int_{-h}^{0}\cos^2 k_n(z+h)dz} \\ &= -\frac{4i\omega}{\sin 2k_nh + 2k_nh}\int_{-h}^{0}\xi_0(z)\cos k_n(z+h)dz \end{aligned} \tag{3.26}$$

3.1.2.2 Hydrodynamic Forces Acting on the Wavemaker. Piston-Type Case

The dynamic wave pressure ***p$_w$*** at the wavemaker (***x***=0) is

$$-\rho\frac{\partial\Phi}{\partial t}\bigg|_{x=0} = -i\rho\omega\phi|_{x=0}\, e^{i\omega t}$$

$$= -i\rho\omega[A cosh k\,(z+h) + \textstyle\sum_{n=1}^{\infty} B_n cos k_n(z+h)]\, e^{i\omega t} \tag{3.27}$$

For the piston-type wavemaker, the displacement at the board is constant, so let's consider $\xi_o(\,z) = d$ (=const.). Thus, from Eq. (3.25) and (3.26), ***A*** and ***B$_n$*** are expressed by Eqs. (3.28) and (3.29), respectively.

$$A\; = -\frac{4\omega}{\sinh 2kh + 2kh}\,\frac{d}{k}\,\sinh kh \tag{3.28}$$

$$B_n\; = -\frac{4i\omega}{\sin 2k_nh + 2k_nh}\,\frac{d}{k_n}\,\sin k_nh \tag{3.29}$$

Considering the above, the wave force ***F*** acting on the board of the wavemaker can be derived and rearranged as follows:

$$F = \int_{-h}^{0} p_w(-1)\, dz$$

$$= -i\rho\omega\left\{\frac{4\omega}{\sinh 2kh + 2kh}\,\frac{d}{k}\,\sinh kh \int_{-h}^{0}\cosh k(z+h)dz + \sum_{n=1}^{\infty}\frac{4i\omega}{\sin 2k_nh + 2k_nh}\,\frac{d}{k_n}\,\sin k_nh\int_{-h}^{0}\cos k_n(z+h)dz\right\} e^{i\omega t}$$

$$= -i\rho\omega\left\{\frac{4\omega}{\sinh 2kh + 2kh}\,\frac{d}{k}\,\sinh kh\,\frac{1}{k}\,\sinh kh + \sum_{n=1}^{\infty}\frac{4i\omega}{\sin 2k_nh + 2k_nh}\,\frac{d}{k_n}\,\sin k_nh\,\frac{1}{k_n}\,\sin k_nh\right\} e^{i\omega t}$$

$$= -4i\rho\omega^2 d\left\{\frac{\sinh^2 kh}{k^2(\sinh 2kh + 2kh)} + \sum_{n=1}^{\infty}\frac{i\,\sin^2 k_nh}{{k_n}^2(\sin 2k_nh + 2k_nh)}\right\} e^{i\omega t}$$

$$F = \frac{-4\rho\omega\, sinh^2 kh}{k^2(sinh\, 2kh + 2kh)}\left(i\omega d e^{i\omega t}\right) - 4\rho\sum_{n=1}^{\infty}\frac{sin^2 k_nh}{{k_n}^2(sin\, 2k_nh + 2k_nh)}\left(-\omega^2 d e^{i\omega t}\right) \tag{3.30}$$

The latest arrangement allows visualizing the first $\left(i\omega d e^{i\omega t}\right)$ and second $\left(-\omega^2 d e^{i\omega t}\right)$ derivatives of the board motion $\boldsymbol{\xi}$. Furthermore, for easier visualization, the elements associated with them are grouped and renamed as $\boldsymbol{N}$ and $\boldsymbol{M}$. Those terms are called hydrodynamic parameters: the "damping coefficient" and the "added mass", Eqs. (3.31) and (3.32) respectively. Hence, the force $\boldsymbol{F}$ can simply be written as in Eq. (3.33), where the negative sign represents that it is a reaction force. This form will be used for further derivations later in this chapter and the following chapter.

$$N = \frac{4\rho\omega \, sinh^2 \, kh}{k^2(sinh\,2kh + 2kh)} \tag{3.31}$$

$$M = 4\rho \sum_{n=1}^{\infty} \frac{sin^2 \, k_n h}{{k_n}^2(sin\,2k_n h + 2k_n h)} \tag{3.32}$$

$$F = -N\frac{d\xi}{dt} - M\frac{d^2\xi}{dt^2} \tag{3.33}$$

By using the dimensionless expression of the frequency in the dispersion equation, as in Eq. (3.20), the dimensionless forms of $\boldsymbol{N}$ and $\boldsymbol{M}$, as in Eqs. (3.34) and (3.35), provide insights into the physical meaning of such parameters and their application to the solution of real engineering problems.

$$\frac{N}{\rho\omega h^2} = \frac{4\,sinh^2 \, kh}{(kh)^2(sinh\,2kh + 2kh)} \tag{3.34}$$

$$\frac{M}{\rho h^2} = 4\sum_{n=1}^{\infty} \frac{sin^2 \, k_n h}{(k_n h)^2(sin\,2k_n h + 2k_n h)} \tag{3.35}$$

Figure 3.3 displays the dimensionless damping coefficient $\frac{N}{\rho\omega h^2}$ and dimensionless added mass $\frac{M}{\rho h^2}$ as functions of $\frac{\omega^2 h}{g}$. In this case, the two sides of the wavemaker board are considered; thus, the values are $2\frac{N}{\rho\omega h^2}$ and $2\frac{M}{\rho h^2}$.

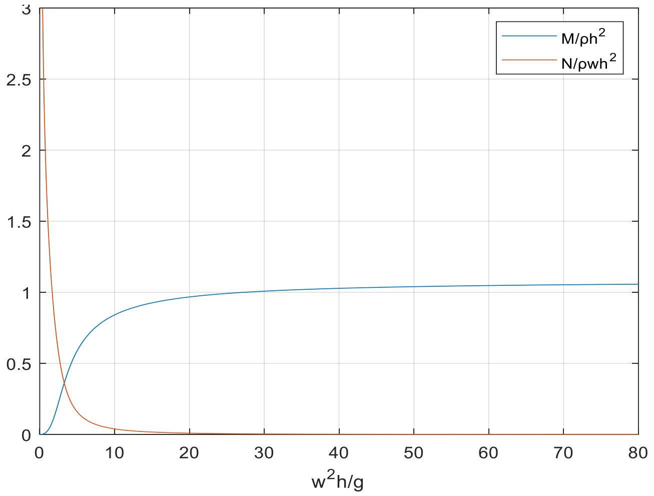

Figure 3.3. Dimensionless damping coefficient and added mass as functions of $\frac{w^2h}{g}$. (Fundora, 2021)

When frequency tends to be infinite, the damping coefficient $N_{(\omega\to\infty)} = 0$. It is not a surprise that the damping coefficient gets reduced to nullity. Since damping is the process of dissipating the energy from the radiated waves, it is reasonable that after a stroke of the board, an immediate damping process occurs, leading to a decrease in the amplitude of the oscillation until all the energy due to the stroke is dissipated.

On the other hand, the added mass at an infinite frequency is $M_{(\omega\to\infty)} = 1.0855\rho h^2$. The dimensionless value 1.0855 is obtained analytically by calculating the limit of the expression of added mass from Eq. (3.35) when the frequency ω tends to infinite. That value is considered as the "constant added mass", which hereafter will be related to the symbol $\boldsymbol{M}^\infty$. It is important to note that the direct output of the limit calculation is 0.54275, but the two sides of the wavemaker board are considered. This value corresponds to the 0.543 value first obtained by Cooker and Peregrine (1990) in their solution derivation for the two-dimensional boundary-value problem for water wave impact on a vertical wall. The term used in the mentioned study was 'momentum length for a semi-infinite wave’ and the nominalization was not by the same dimensions or properties as in this study, but it can be considered as an equivalent analysis.

Furthermore, following the dependence of the added mass to the geometry explained before, the constant added mass of 1.0855 is related to the board's shape: a rectangular prism or a rectangle in a two-dimensional analysis, in this case with a small width. However, from the second half of the 1990s, the inclusion of the added mass or hydrodynamic mass in the sliding calculation was extended by Oumeraci and Kortenhaus (1994). Aoki and Okube (1995) introduced the use of the dimensionless value 1.0855 and were followed by Shimosako and Takahashi (1998,2000), Miguel Esteban et al. (2007) and others. Before that, inertia was mainly considered only as the relation of the caisson mass in water or experimentally determined.

Besides the theoretical calculation of the constant added mass, a numerical verification was carried out in a previous study (Fundora, 2021). For example, for $\frac{\omega^2 h}{g}$ =500, around $\boldsymbol{\omega}$ =100 rad/s, $\boldsymbol{M}^{\infty}$ = 1.0811159564, demonstrating the tendency to the theoretical value.

3.1.2.3 Hydrodynamic Forces Expressed in Time-Domain. Components: Added Mass and Memory- Effect Function.

In section 3.1.2.2, the hydrodynamic force acting on the wave board (which can be applied to vertical walls, i.e., vertical caissons) is expressed by the damping coefficient $\boldsymbol{N}$ and the added mass $\boldsymbol{M}$, both of which are given as the function of wave frequency $\boldsymbol{\omega}$. However, when included in systems with only time-dependent parameters, frequency-domain parameters may present challenges. Thus, the translation to the time domain proves to be useful in such cases, which accounts for numerous engineering problems.

Then, if an arbitrary motion of the wavemaker board is considered as a succession of impulsive displacements, time-domain hydrodynamic forces can be expressed as the sum of the reaction forces caused by the impulsive motion of that board. An analogy of using the impulse response function in linear systems, as in Cummins (1962), is used for the below derivation.

Impulsive displacements $\varDelta\xi$ taking place in small durations $\varDelta t$ are expressed as:

$$\varDelta\xi = \frac{d\xi}{dt}\varDelta t \tag{3.36}$$

In the period of $\varDelta t$, it is assumed that the fluid motion has a velocity potential $\varPhi$ that is proportional to $\boldsymbol{v}$ i.e., $\varPsi\frac{d\xi}{dt}$, being $\varPsi$ any function for now unknown. After the impulsive movement, the water surface elevation induced by the impulsive displacement will decay and finally be still. By taking the velocity potential of the decaying wave expressed as $\varphi\varDelta\xi$; if such impulsive displacement is continuously generated, the velocity potential at the time t is defined as in Eq.(3.37). In there, if t refers to the time at which the output is observed, τ refers to the time at which the input is applied.

$$\varPhi(x,z,t) = \psi\frac{d\xi}{dt} + \int_{-\infty}^{t}\varphi(t-\tau)\frac{d\xi}{dt}(\tau)d\tau \tag{3.37}$$

The pressure is then given as:

$$p(x,z,t) = -\rho\frac{\partial\Phi}{\partial t} = -\rho\psi\frac{d^2\xi}{dt^2} + \int_{-\infty}^{t}\frac{\partial\varphi(t-\tau)}{\partial t}\frac{d\xi}{dt}(\tau)d\tau \tag{3.38}$$

And the force *F* acting on the board is obtained by integrating the pressure at *x*=0.

$$\begin{aligned} F(t) &= \int_{-h}^{0} p(-1)\,dz \\ &= \rho\int_{-h}^{0}\psi\frac{d^2\xi}{dt^2}dz + \rho\int_{-h}^{0}\left[\int_{-\infty}^{t}\frac{\partial\varphi(t-\tau)}{\partial t}\frac{d\xi}{dt}(\tau)d\tau\right]dz \end{aligned} \tag{3.39}$$

By letting the first and second terms be as in Eqs. (3.40) and (3.41), respectively,

$$\mu = -\rho\int_{-h}^{0}\psi dz \tag{3.40}$$

$$R(t) = -\rho \int_{-h}^{0} \frac{\partial \varphi(t)}{\partial t} dz \tag{3.41}$$

The force in Eq.(3.39) yields to Eq.(3.42). The latter can also be expressed as in Eq.(3.43).

$$F(t) = -\mu \frac{d^2\xi}{dt^2} - \int_{-\infty}^{t} R(t-\tau) \frac{d\xi}{dt}(\tau) d\tau \tag{3.42}$$

$$F(t) = -\mu \frac{d^2\xi}{dt^2} - \int_{0}^{\infty} R(\tau) \frac{d\xi}{dt}(t-\tau) d\tau \tag{3.43}$$

The above equation is for an arbitrary motion; thus, if we consider a sinusoidal displacement, $\xi = de^{i\omega t}$ can be substituted into it.

$$\begin{aligned} F &= -\mu(-\omega^2 d) - \int_0^\infty R(\tau)(i\omega d) e^{i\omega(t-\tau)} d\tau \\ &= \left[-\mu(-\omega^2 d) - \omega d \int_0^\infty R(\tau)\ \sin \omega\tau\, d\tau - i\omega d \int_0^\infty R(\tau)\ \cos \omega\tau\, d\tau \right] e^{i\omega t} \\ &= -(i\omega d e^{i\omega t}) \int_0^\infty R(\tau)\ \cos \omega\tau\, d\tau \\ &\quad - \left(-\omega^2 d e^{i\omega t}\right) \left[\mu - \frac{1}{\omega} \int_0^\infty R(\tau)\ \sin \omega\tau\, d\tau \right] \end{aligned} \tag{3.44}$$

When recalling the force's structure in Eq. (3.33), then ***N*** and ***M*** can also be expressed as:

$$N(\omega) = \int_0^\infty R(\tau)\, cos\ \omega\tau\, d\tau \tag{3.45}$$

$$M(\omega) = \mu - \frac{1}{\omega} \int_0^\infty R(\tau) \sin \omega\tau\, d\tau \tag{3.46}$$

While applying the inverse Fourier transform to the above equations are as below:

$$R(t) = \frac{2}{\pi} \int_0^\infty N(\omega) \cos \omega\tau\, d\tau \tag{3.47}$$

$$\mu = M(\omega') - \frac{1}{\omega'}\int_0^\infty R(\tau)\sin\omega'\tau\, d\tau \tag{3.48}$$

The ' symbol is used to underline that ω' and ω are different. When ω' tends to infinite, the second term of the right-hand side of Eq.(3.48) becomes zero; thus it is proper to say that:

$$\mu = M_{(\omega\prime=\infty)} \tag{3.49}$$

R(t) is referred to as the 'memory-effect function' or 'retardation function'. While ***μ*** is the 'constant added mass', which is not the function of ***ω*** and hereafter will be used the same symbol from the previous section: ***M***$^\infty$. Aoki and Okube (1995) expressed the memory-effect function of a regular breakwater not as a function of frequency ***ω*** but of a term **κ** as in Eq.(3.50) where **κ** **=** ***kh***. That is basically the rearrangement of Eq. (3.47) after substituting ***N(ω)*** for the expression of ***N*** in Eq. (3.34) to switch its dependence on frequency to the wave number ***k*** by introducing the derivation of frequency from the dispersion relation. They also presented a linear approximation, as seen in Eq.(3.51). The memory-effect function, as in Aoki and Okube (1995), was later used by researchers such as Takagi and Shibayama (2006). The output of the two versions can be seen in Figure 3.4.

$$R(t) = \frac{4\rho g h}{\pi}\int_0^\infty \frac{\tanh^2\kappa}{\kappa^2}\cos\left(\sqrt{\kappa\tanh\kappa}\sqrt{g/h}\,t\right)d\kappa \tag{3.50}$$

$$R(t) = \left(2.17 - 1.146\sqrt{\frac{g}{h}}t\right)\rho g h \tag{3.51}$$

Furthermore, another relationship is observed: dimensionless memory-effect function for ***t***=0 is $R^*_{(t^*=0)} = 2.1710$, and the dimensionless added mass for infinite frequencies is $M^*_{(\omega^*\to\infty)} = 1.0855$ for the case of regular caisson breakwaters.

$$M^*_{(\omega^*\to\infty)} = \frac{1}{2}R^*_{(t^*=0)} = 1.0855 \tag{3.52}$$

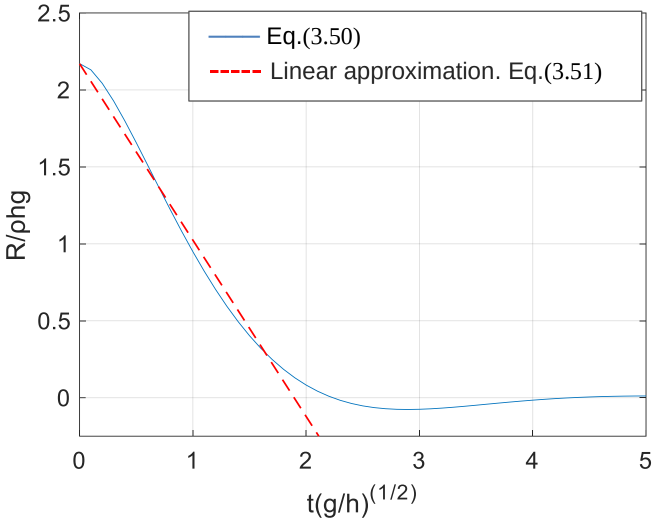

Figure 3.4. Dimensionless Memory- Effect Function

3.1.3 *Wave forces*

In Chapter 2, existing models for time-history wave loads on caisson breakwaters were discussed. For this study, the wave force in time-domain ***F(t)*** is determined by a triangle-shaped profile (Figure 3.5) used in Aoki and Okube (1995) for sliding calculation, which is similar to the model introduced by Shimosako and Takahashi (1994).

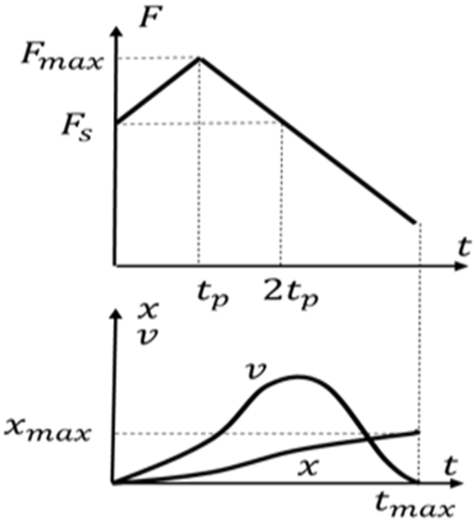

Figure 3.5. Diagrams for times series model of the wave force for sliding calculation and displacement-velocity time series.

The mathematical expression for the above model is as in Eq. (3.53) where $\boldsymbol{F_s}$ is the static frictional force (note that in the previous subsection, relation $\boldsymbol{F_s = F_f}$ was already established), $\boldsymbol{t}$ is time, $\boldsymbol{t_p}$ the wave force rising time and $\boldsymbol{\alpha}$ the wave force magnitude or rising coefficient. Following the model representing the physical phenomena, the caisson will slide when the wave force $\boldsymbol{F}$ exceeds the maximum static friction force $\boldsymbol{F_s}$. Thus, the model at time $\boldsymbol{t} = 0$ represents a wave force equal to the static frictional force $\boldsymbol{F(t=0) = F_s}$, and a maximum force $\boldsymbol{F_{max}}$ achieved at $\boldsymbol{t} = \boldsymbol{t_p}$ with a value shown in Eq.(3.54).

.

$$F(t) = \left\{ \begin{array}{ll} \dfrac{\alpha F_s}{t_p} t + F_s & (0 \le t \le t_p) \\ -\dfrac{\alpha F_s}{t_p} t + (1 + 2\alpha) F_s & (t_p \le t) \end{array} \right\} \tag{3.53}$$

$$F(t_p) = F_{max} = (1 + \alpha) F_s \tag{3.54}$$

Therefore, if $\boldsymbol{F_s}$ is known, the profile is determined using $\boldsymbol{\alpha}$ (the wave force magnitude) as a parameter. Furthermore, according to this figure, the maximum velocity $\boldsymbol{v_{max}}$ is obtained after the peak on the wave force, close to $\boldsymbol{t} = 2\boldsymbol{t_p}$ when $\boldsymbol{F(t)}$ is again lower than $\boldsymbol{F_s}$, but there is still energy from the precedent movement. From there, it reduces until reaching zero, when the wave force gets radically smaller with respect to $\boldsymbol{F_s}$. At that point, sliding stops, and the maximum value of displacement $\boldsymbol{x}$ is achieved.

3.1.4 *Equation of motion for regular caissons*

Accounting for the derivations in section 3.1.2, the motion of the wavemaker board is described by Eq.(3.55). It follows Newton's 2nd law, in which $\boldsymbol{m}$ is the mass of the caisson, $\frac{d^2\xi}{dt^2}$ term the acceleration, and $\boldsymbol{f}$ the summatory of forces acting on the caisson, including terms such as the added mass $\boldsymbol{M}$ and the velocity component $\frac{d\xi}{dt}$ with the damping coefficient $\boldsymbol{N}$. By applying the wavemaker theory to the breakwater caisson problem and using the memory-effect function, Eq.

(3.56) serves as an alternative to Eq.(3.55) and where the lower limit in the integration -∞ can be replaced by 0 when considering the wavemaker board (caisson) movement starting at t=0.

$$(m+M)\frac{d^2\xi}{dt^2}+N\frac{d\xi}{dt}=f \tag{3.55}$$

$$(m+\mu)\frac{d^2\xi}{dt^2}+\int_{-\infty}^{t}R(t-\tau)\frac{d\xi}{dt}(\tau)d\tau=f \tag{3.56}$$

Referring to the right-hand side of the above equations, the horizontal forces acting on the caisson during the sliding motion are shown in Figure 3.6, where $\boldsymbol{F}$ is the wave force, $\boldsymbol{F_f}$ *is* the frictional force, and $\boldsymbol{F_R}$ the resistance force. In this model, vertical forces such as the uplift forces are dismissed. In the simplified model of Aoki and Okube (1995) and the one proposed by Shimosako and Takahashi (2000), it is assumed that the friction coefficient takes a constant value corresponding to both the static $\boldsymbol{f_s}$ and the dynamic $\boldsymbol{f_f}$ coefficients. Since $\boldsymbol{f_s} = \boldsymbol{f_f}$, the dynamic frictional force $\boldsymbol{F_f}=\boldsymbol{f_f}*\boldsymbol{W_w}$ and the static frictional force $\boldsymbol{F_s}=\boldsymbol{f_s}*\boldsymbol{W_w}$ share the same value. That consistent assumption is made and followed. $\boldsymbol{W_w}$ is the weight of the structure in water and the product of $\boldsymbol{m_w g}$, where $\boldsymbol{m_w}$ is the mass of the caisson in water and $\boldsymbol{g}$ ***is*** the acceleration of gravity.

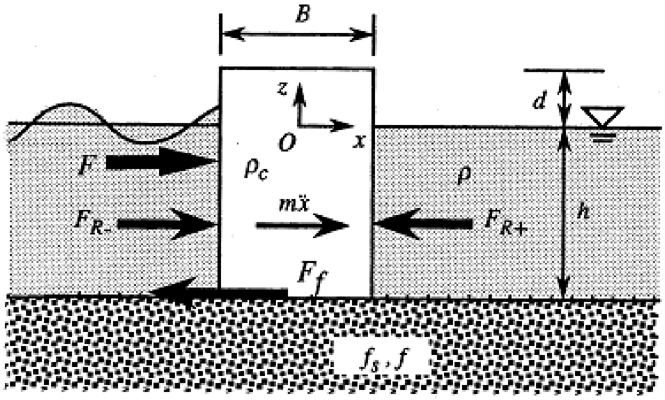

Figure 3.6. Forces acting on a vertical breakwater caisson (Aoki and Okube, 1995)

Consequently, Eq.(3.56) can be rewritten as Eq. (3.57) where $\boldsymbol{m}$ is the mass of the caisson, $\boldsymbol{F(t)}$ is the wave force in the time-domain, and $\boldsymbol{F_f}$ is the frictional force. As it was explained before, $\boldsymbol{M_\infty}$ refers to the added mass force generated by the water surrounding the caisson due to its motion, and the integration term refers to the wave-making damping. Furthermore, considering $\boldsymbol{x}$ the displacement or sliding, the terms $\dot{\boldsymbol{x}}$ and $\ddot{\boldsymbol{x}}$ are their first and second derivative with respect to time i.e., the motion's velocity and acceleration, respectively. Accordingly, the sliding distance of the caisson can be calculated by numerically integrating the below equation twice with respect to time.

$$(m + M_\infty)\ddot{x} + \int_0^t R(t-\tau)\dot{x}(\tau)d\tau = F(t) - F_f \tag{3.57}$$

Substituting the wave time-history load in Eq. (3.57), the motion equation can be rewritten as below, and it is the final form used in this study for vertical breakwaters with regular caissons.

$$(m_a + M_{xx}^\infty)\ddot{x} + \int_0^t R_{xx}(t-\tau)\dot{x}(\tau)d\tau = \begin{cases} \alpha f_s \dfrac{t}{t_p} m_w g & (0 \le t \le t_p) \\ \alpha f_s \left(2 - \dfrac{t}{t_p}\right) m_w g & (t_p \le t) \end{cases} \tag{3.58}$$

An example configuration with the characteristics and properties as in Aoki and Okube (1995) and Yoshihara (2019) is tested to obtain concrete values. The solution to the motion equation is shown in Figure 3.7.

Table 3-2. Geometrical characteristics and properties of an example configuration for the analytical model.

Characteristics / Properties	Symbol	Value
Water depth	$\boldsymbol{h}$	8 m
Caisson width	$\boldsymbol{B}$	6 m
Freeboard	$\boldsymbol{d}$	2 m
Friction coef.	$\boldsymbol{f, f_s}$	0.6
Rising time	$\boldsymbol{t_p}$	0.5 s
Wave force coef.	$\boldsymbol{\alpha}$	0.1
Water density	$\boldsymbol{\rho}$	1000 kg/ m3
Concrete density	$\boldsymbol{\rho_c}$	2150 kg/ m3

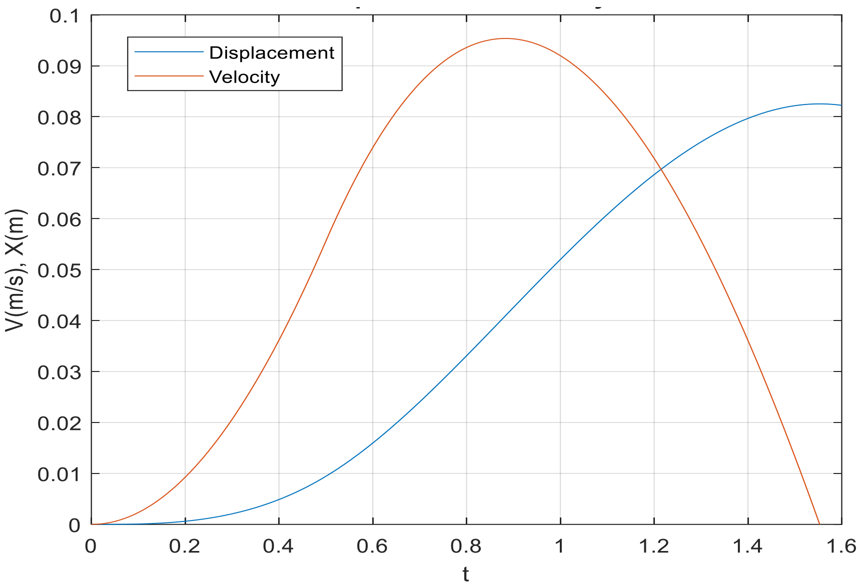

Figure 3.7 Displacement and velocity of the wavemaker board/caisson (for α=0.1, t_p=0.5, f=f_s=0.6)

3.2 MODEL DESCRIPTION AND GENERAL METHODOLOGY

The models used in the theoretical study represent caissons with horizontal plates on the harbor side. The derivation of the models is made to allow investigation of the effect of submerged horizontal plates on the performance of a vertical breakwater during the failure process by simulating the caisson sliding under impulsive wave loads. The analysis cases include caissons with a single plate at the surface, a single submerged plate, and twin plates with diverse plate lengths and arrangements that attend to submersion depth. A semi-analytical model developed by the author (Fundora and Aoki, 2023 and 2024) based on the piston-type wavemaker theory to estimate the hydrodynamic characteristics due to the fluid-structure interaction and simulate the sliding of the geometries object of study.

3.2.1 *Caisson with A Submerged Horizontal Plate.*

The structure consists of a semi-submerged caisson of width ***B*** and freeboard ***d***, with a rear submerged horizontal plate of longitude ***l***, as shown in Figure 3.8. In this study, the horizontal axis is at the sea surface level, and the vertical axis corresponds to the rear wall of the caisson. The seabed is considered parallel to the sea surface; thus, the water depth ***h*** is constant.

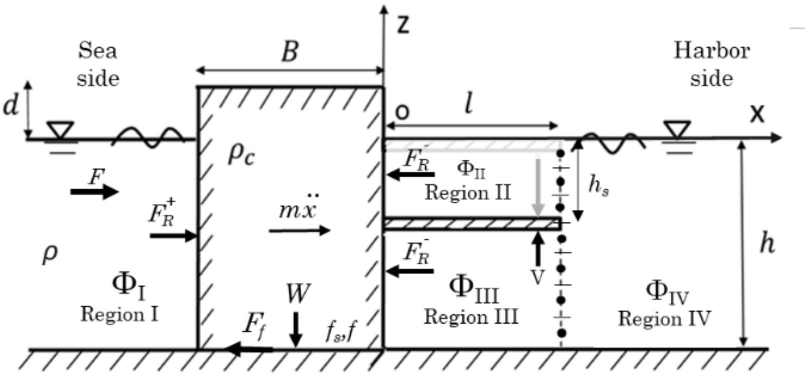

Figure 3.8. Model representation of a caisson with a submerged horizontal plate.(Fundora and Aoki, 2024)

The fluid is divided into four sub-domains with different velocity potentials $\boldsymbol{\Phi}$. For the analysis, $\boldsymbol{F}$: wave force, $\boldsymbol{F_R}$: horizontal reaction force, $\boldsymbol{V}$: vertical reaction force, and $\boldsymbol{F_f}$: frictional force; $\boldsymbol{m}$: caisson mass, $\boldsymbol{W}$: caisson weight, and $\boldsymbol{h_s}$: submerged depth. General materials properties are given by the hydrodynamic and static frictional coefficients $\boldsymbol{f}$ and $\boldsymbol{f_s}$, respectively, water density $\boldsymbol{\rho}$, and concrete density $\boldsymbol{\rho_c}$.

3.2.2 *Caisson with Twin Plates*

The initial hypothesis of the influence of water constriction on incrementing hydrodynamic coefficients, such as added mass, was presented before. Nevertheless, to further investigate the effects of the added mass, but also the damping on the general sliding of the caisson, a twin plate arrangement model is also derived.

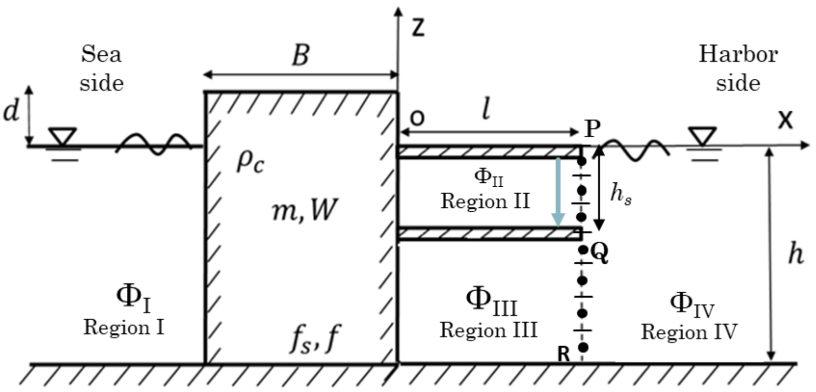

Figure 3.9. Model representation of a caisson with twin plates.

The twin plates arrangement keeps one plate at the water surface and the second one is submerged at ½ of the water depth. Although different submersion depth can be analyzed with the derived model and methodology, a single location is enough to validate the hypothesis for this section. Water depth and properties of the medium remain, as in the case with a single plate.

3.2.3 *Methodology*

A semi-analytical model for the sliding simulation of caissons with submerged plates, which includes the special case of a plate at the surface (Fundora and Aoki, 2023) and twin plates, is developed based on the linear wavemaker theory (Dean and Dalrymple, 1984) and potential theory the sliding calculation method from Aoki and Okube (1995).

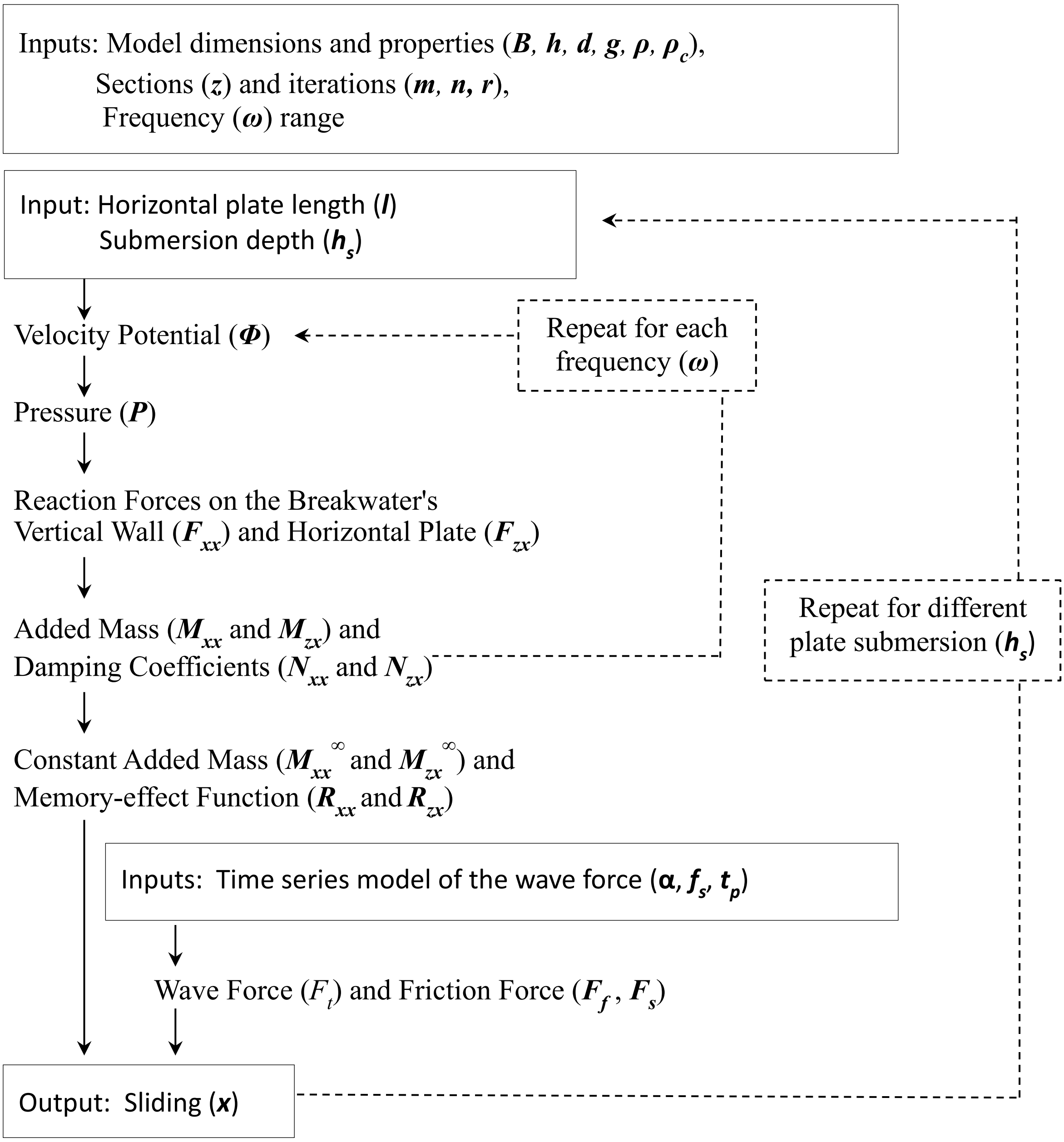

Figure 3.10. Sliding Calculation Flow (Fundora and Aoki, 2024)

The Boundary Point Selection method (BPSM) (Fundora and Aoki, 2023; Yoshida et al., 1990) is used to solve the boundary problem of the fluid-structure interaction. The simulation model includes vertical forces (represented by the vertical added mass $\boldsymbol{M_{zx}}$ and the memory-effect function $\boldsymbol{R_{zx}}$). Initially, the caisson sliding simulation is performed using the same parameters from previous studies to validate the model with the solutions by the conventional potential method for a regular caisson (Yoshihara, 2019) and a caisson with a horizontal plate of different lengths (Fundora and Aoki, 2023). Simulations for different plate lengths and submersion depths are performed using a MATLAB code written to solve the theoretical formulations.

3.3 GOVERNING EQUATIONS. BOUNDARY AND CONTINUITY CONDITIONS.

Determining the velocity potential in each region is the starting point of the methodology. According to wave theory, its general form is expressed as Eq.(3.59), where $\boldsymbol{\phi_j}$ is a superposition of the progressive wave and the decaying wave (evanescent mode wave), $\boldsymbol{\omega}$ is frequency, $\boldsymbol{t}$ is time, and subscript $\boldsymbol{j} = \boldsymbol{I}, \boldsymbol{II}, \boldsymbol{III}, \boldsymbol{IV}$ indicates the regions of the model.

$$\Phi_j(x,z,t) = \phi_j(x,z)e^{i\omega t} \tag{3.59}$$

3.3.1 *Caisson with A Submerged Horizontal Plate*

For the model of the caisson with a submerged horizontal plate, Region I is the free surface in the seaside of the caisson, Region II is the fluid area behind the harborside wall within the water surface and the submerged plate, Region III is the fluid area between the submerged plate and the seabed, while Region IV is the harborside area located after the plate. This model can also be applied to a plate at the surface by making $\boldsymbol{h_s}$ equal to zero and dismissing Region II in the analysis.

3.3.1.1 Boundary and Continuity Conditions

Linked to the analytical derivation of the velocity potentials and the solution of the boundary problem itself, the boundary and continuity conditions must first be stated. Based on the wavemaker theory (Dean and Dalrymple, 1984), the "sinusoidal motion" of the breakwater is given by Eq.(3.60) as the vertical boundary condition considering $d(\text{constant}) = \xi_0(\mathrm{z})$ where ξ_0 is the initial deformation or displacement. The horizontal conditions at the bottom and the plate are presented by Eq.(3.61) while the continuity or Laplace's equation for the regions is expressed in Eq.(3.62). Furthermore, regions II and III share a physical boundary with region IV at $\boldsymbol{x}=\boldsymbol{l}$. Thus, accounting for the continuity of the horizontal fluid velocities and the wave pressure fluctuations due to continuities of mass and energy flux through the boundary is required and expressed by Eqs. (3.63), (3.64), (3.65) and (3.66). This is a resume of the boundary and continuity condition; nonetheless, each region's particularities will be described in the following subsections.

$$\frac{\partial \phi_j}{\partial x} = i\omega d\,;\;\; x = -B\ (j = I);\; x = 0\ (j = II, III) \tag{3.60}$$

$$\frac{\partial \phi_j}{\partial z} = 0 \;\;;\;\; z = -h_s\ (j = II, III);\; z = -h\ \ (j = III) \tag{3.61}$$

$$\frac{\partial^2 \phi_j}{\partial x^2} + \frac{\partial^2 \phi_j}{\partial z^2} = 0 \;\;;\;\; (j = II, III, IV) \tag{3.62}$$

$$\phi_{\mathrm{IV}}(l, z) = \begin{cases} \phi_{\mathrm{II}}(l, z) & (0 \geq z \geq -h_s) \quad (3.63) \\ \phi_{\mathrm{III}}(l, z) & (-h_s \geq z \geq -h) \quad (3.64) \end{cases}$$

$$\frac{\partial \phi_{\mathrm{IV}}(l, z)}{\partial x} = \begin{cases} \dfrac{\partial \phi_{\mathrm{II}}(l, z)}{\partial x} & (0 \geq z \geq -h_s) \quad (3.65) \\ \dfrac{\partial \phi_{\mathrm{III}}(l, z)}{\partial x} & (-h_s \geq z \geq -h) \quad (3.66) \end{cases}$$

3.3.1.2 Velocity potential and boundary condition in Region I

The general form of the velocity potential in Region I is expressed as:

$$\Phi_{\mathrm{I}}(x,z,t) = \phi_{\mathrm{I}}(x,z)e^{i\omega t} \tag{3.67}$$

where ϕ_{I} is a superposition of the progressive wave and the decaying wave (evanescent mode wave). The caisson width $\boldsymbol{B}$ is added since the axis origin is in the shoreward surface of the breakwater.

$$\phi_{\mathrm{I}}(x,z) = A^{\mathrm{I}+} coshk\,(z+h)e^{ik(x+B)} + \sum_{n=1}^{\infty} B_n^{\mathrm{I}+} cosk_n(z+h)e^{k_n(x+B)} \tag{3.68}$$

$\boldsymbol{A^{\mathrm{I}+}}$ and $\boldsymbol{B_n^{\mathrm{I}+}}$ are unknown coefficients, while $\boldsymbol{k}$ and $\boldsymbol{k_n}$ are eigenvalues determined by the expressions below where the first equality is the dispersion relation. The subscript and superscript $\boldsymbol{j}$ refer to the region's notation, although in regions **I** and **IV** it will not be utilized since the region's height coincides with the water depth $\boldsymbol{h}$. Thus, for simplicity, $\boldsymbol{h_I} = \boldsymbol{h_{IV}} = \boldsymbol{h}$ and $\boldsymbol{k^I} = \boldsymbol{k^{IV}} = \boldsymbol{k}$.

$$\frac{\omega^2 h_j}{g} = kh \tanh k^j h_j = -k_n^j h_j \tan k_n^j h_j \qquad ;(j = I, II, IV) \tag{3.69}$$

The "sinusoidal motion" of the breakwater is given by Eq. (3.70) as the vertical boundary condition, with $\boldsymbol{\xi_0}$ as the initial deformation/displacement.

$$\frac{\partial \phi_{\mathrm{I}}(-B,\ z)}{\partial x} = i\omega\xi_0(z) \qquad \text{at} \quad x = -B \tag{3.70}$$

Substituting Eq.(3.68) into Eq.(3.70) and taking the consideration $\boldsymbol{\xi_0(z)} = \boldsymbol{d}$ constant, the following expression is obtained.

$$ikA^{\mathrm{I}+} coshk\,(z+h) + \sum_{n=1}^{\infty} k_n B_n^{\mathrm{I}+} cosk_n(z+h) = i\omega d \tag{3.71}$$

3.3.1.3 Velocity potential in the region over the horizontal plate (II): x < l

The general form of the velocity potential for the region over the plate is expressed as:

$$\Phi_{\mathrm{II}}(x,z,t) = \phi_{\mathrm{II}}(x,z)e^{i\omega t} \tag{3.72}$$

The terms of $\boldsymbol{\phi_{II}}$ are similar to the ones in Eq.(3.68) but with the axis origin in the shoreward surface of the breakwater and with the particular of using $\boldsymbol{h_{II} = h_s}$ as water depth. Additionally, an extra term is included, representing the form of the wave moving as a response to the *x*-movement (a sort of reflection). Notice that although the general form is alike, the coefficients are different. $A^-$and A^+ are complex constants representing the incident and reflected waves, respectively. B_n^- and B_n^+ represent the evanescent mode of such waves which vanish at $\boldsymbol{x} \rightarrow \infty$.

$$\begin{aligned}\phi_{\mathrm{II}}(x,z) = A^- \cosh k^{II}(z+h_{II})\, e^{-ik^{II}x} + \sum_{n=1}^{\infty} B_n^- \cos k_n^{II}(z+h_{II})\, e^{-k_n^{II}x} \\ + A^+ \cosh k^{II}(z+h_{II})\, e^{ik^{II}\mathrm{x}} + \sum_{n=1}^{\infty} B_n^+ \cos k_n^{II}(z+h_{II})\, e^{k_n^{II}x}\end{aligned} \tag{3.73}$$

The governing equation and boundary conditions are:

$$\frac{\partial^2\phi_{\mathrm{II}}}{\partial x^2} + \frac{\partial^2\phi_{\mathrm{II}}}{\partial z^2} = 0 \tag{3.74}$$

$$\frac{\partial\phi_{\mathrm{II}}}{\partial x} = i\omega d \qquad \text{at } x = 0 \tag{3.75}$$

$$\frac{\partial\phi_{\mathrm{II}}}{\partial z} = 0 \qquad \text{at } z = -h_s \tag{3.76}$$

Thus, substituting Eq. (3.73) in Eq.(3.75), the following expression is obtained.

$$\begin{aligned}-ik^{II}A^- coshk^{II}\,(z+h_{II}) \\ + \sum_{n=1}^{\infty} -k_n^{II}B_n^- cosk_n^{II}(z+h_{II}) + ik^{II}A^+ coshk^{II}\,(z+h_{II}) \\ + \sum_{n=1}^{\infty} k_n^{II}B_n^+ cosk_n^{II}(z+h_{II}) = i\omega d\end{aligned} \tag{3.77}$$

3.3.1.4 Velocity potential in the region under the horizontal plate (III): x < l

The general form of the velocity potential is expressed as:

$$\Phi_{\mathrm{II}}(x,z,t) = \phi_{\mathrm{II}}(x,z)e^{i\omega t} \tag{3.78}$$

The governing equation and boundary conditions are:

$$\frac{\partial^2\phi_{\mathrm{III}}}{\partial x^2} + \frac{\partial^2\phi_{\mathrm{III}}}{\partial z^2} = 0 \tag{3.79}$$

$$\frac{\partial\phi_{\mathrm{III}}}{\partial x} = i\omega d \qquad \text{at } x = 0 \tag{3.80}$$

$$\frac{\partial\phi_{\mathrm{III}}}{\partial z} = 0 \qquad \text{at } z = -h \text{ and } z = -hs \tag{3.81}$$

To obtain the general form of $\boldsymbol{\phi}_{III}$, which satisfies the above equation, Fourier cosine expansion with respect to z is used as below. Note that ***m*** is the series terms, and it is not related to the same symbol used as mass of the caisson.

$$\phi_{\mathrm{III}}(x,z) = \frac{1}{h_{III}}\tilde{\phi}_0{}^{III}(x) + \frac{2}{h_{III}}\sum_{m=1}^{\infty}\tilde{\phi}_m{}^{III}(x)\cos\frac{m\pi}{h_{III}}(z+h) \tag{3.82}$$

where $\tilde{\boldsymbol{\phi}}_{\boldsymbol{m}}{}^{\boldsymbol{III}}(\boldsymbol{x})$ is given as in Eq.(3.83).

$$\tilde{\phi}_m{}^{III}(x) = \int_{-h}^{-h_s}\phi_{\mathrm{III}}(x,z)\cos\frac{m\pi}{h_{III}}(z+h)dz \ \ ; \ \ (m = 0,1,2,\dots) \tag{3.83}$$

The value of $\boldsymbol{z}$ is taken globally, i.e., measured from the water surface, and the governing equation should be satisfied at the region boundaries. Notice that $\boldsymbol{h_{III}} = \boldsymbol{h}\text{-}\boldsymbol{h_s}$, which can be used to simplify the calculations. Next, to derive the differential equation for $\tilde{\boldsymbol{\phi}}_{\boldsymbol{m}}{}^{\boldsymbol{III}}(\boldsymbol{x})$, Fourier cosine transform is applied to Eq.(3.79).

For the first term,

$$\int_{-h}^{-h_s} \frac{\partial^2 \phi_{\mathrm{III}}}{\partial x^2} \cos \frac{m\pi}{h_{III}} (z+h) dz$$

$$= \frac{\partial^2}{\partial x^2} \int_{-h}^{-h_s} \phi_{\mathrm{III}} \cos \frac{m\pi}{h_{III}} (z+h) dz$$

$$= \frac{d^2 \tilde{\phi}_m{}^{III}}{dx^2} \tag{3.84}$$

For the second term,

$$\int_{-h}^{-h_s} \frac{\partial^2 \phi_{\mathrm{III}}}{\partial z^2} cos \frac{m\pi}{h_{III}} (z+h)\, dz$$

$$= \left[\frac{\partial \phi_{\mathrm{III}}}{\partial z}\ cos \frac{m\pi}{h_{III}} (z+h) \right]_{-h}^{-h_s} + \int_{-h}^{-h_s} \frac{\partial \phi_{\mathrm{III}}}{\partial z} \frac{m\pi}{h_{III}} sin \frac{m\pi}{h_{III}} (z+h)\, dz$$

$$= \left[\phi_{\mathrm{III}}\ \frac{m\pi}{h_{III}} sin \frac{m\pi}{h_{III}} (z+h) \right]_{-h}^{-h_s}$$

$$- \int_{-h}^{-h_s} \phi_{\mathrm{III}} \left(\frac{m\pi}{h_{III}} \right)^2 cos \frac{m\pi}{h_{III}} (z+h)\, dz$$

$$= -\left(\frac{m\pi}{h_{III}} \right)^2 \int_{-h}^{-h_s} \phi_{\mathrm{III}}\, cos \frac{m\pi}{h_{III}} (z+h)\, dz$$

$$= -\left(\frac{m\pi}{h_{III}} \right)^2 \tilde{\phi}_m{}^{III} \tag{3.85}$$

Thus, Eq.(3.79) yields the following ordinary differential equation for $\boldsymbol{\tilde{\phi}_m}$:

$$\frac{d^2 \tilde{\phi}_m{}^{III}}{dx^2} - \left(\frac{m\pi}{h_{III}} \right)^2 \tilde{\phi}_m{}^{III} = 0 \quad ; \quad (m = 0,1,2,\dots) \tag{3.86}$$

And the general solution to the above equation are Eqs.(3.87) and (3.88) where C_o, D_o, C_m, D_m (m=0, 1, 2, …) are unknown coefficients.

$$\tilde{\phi}_0{}^{III}(x) = C_0 + D_0 x \ \ ; \ \ (m = 0) \tag{3.87}$$

$$\tilde{\phi}_m{}^{III} = C_m \cosh \frac{m\pi}{h_{III}} x + D_m \sinh \frac{m\pi}{h_{III}} x \quad ; \ \ (m = 1,2,3,\dots) \tag{3.88}$$

Substituting the preceding terms in Eq. (3.82), the general solution of ϕ_{III} is as below:

$$\phi_{\mathrm{III}}(x,z) = \frac{1}{h_{III}}(C_0 + D_0 x)$$
$$+\frac{2}{h_{III}}\sum_{m=1}^{\infty}\left\{\left(C_m \cosh\frac{m\pi}{h_{III}}x + D_m \sinh\frac{m\pi}{h_{III}}x\right)\cos\frac{m\pi}{h_{III}}(z+h)\right\} \tag{3.89}$$

Then, the application of the vertical boundary condition expressed by Eq.(3.80) yields to:

$$\frac{D_0}{h_{III}} + \frac{2}{h_{III}}\sum_{m=1}^{\infty} D_m \frac{m\pi}{h_{III}}\cos\frac{m\pi}{h_{III}}(z+h) = i\omega d \tag{3.90}$$

3.3.1.5 *Velocity potential in the region after the horizontal plate (IV): x > l*

Region IV is located after the horizontal plate. The velocity potential $\Phi_{\mathrm{IV}}(x,z,t) = \phi_{\mathrm{IV}}(x,z)e^{i\omega t}$ in the region $\boldsymbol{l} < \boldsymbol{x}$ has the same structure as Eq.(3.68), except that the origin of the x-axis is shifted by $\boldsymbol{l}$. Thus, ϕ_{IV} is expressed as:

$$\phi_{\mathrm{IV}}(x,z) = E^- \cosh k(z+h)\, e^{-ik(x-l)} + \sum_{r=1}^{\infty} F_r^- \cos k_r(z+h)\, e^{-k_r(x-l)} \tag{3.91}$$

Where $\boldsymbol{E^-}$and $\boldsymbol{F_r^-}$ ($\boldsymbol{r}$=1, 2, …) are unknown coefficients. Note that a similar equation with a different origin was used in Region I; Since Region IV shares a physical boundary with regions II and III, the method and solution for the coefficients $\boldsymbol{E^-}$ and $\boldsymbol{F_r^-}$ will be explained in the following subsection.

3.3.1.6 *Final Analytical Expression for the Boundary-value Problem*

As stated in the previous subsection, Region IV shares a physical boundary with regions II and III in $\boldsymbol{x}$=$\boldsymbol{l}$. Thus, accounting for the continuity of the horizontal fluid velocities and the wave pressure fluctuations due to mass and energy flux continuities through the boundary is required. Furthermore, determining the final solution of the velocity potential for each region is linked. The undetermined coefficients of the velocity potential of each region are determined by the continuity conditions for the velocity potential and its derivative at the boundary surface of the adjacent regions. Continuity conditions at the boundary ***x*=*l*** (depending on the case) were described in Eqs. (3.63), (3.64), (3.65) and (3.66).

For the analysis, the plate thickness has been disregarded. The cross-section dimensions and mass of the plate are considered infinitesimal inferior to one of the caissons. Furthermore, this is a useful and common simplification when considering analytical solutions. It allows the analysis to focus on the essential behavior of the system without being deterred by the details of individual element thicknesses. By doing so, arriving at more manageable and insightful results is often the output.

Boundary between regions II and IV: Substituting Eqs.(3.73) and (3.91) into the conditions $\phi_{\mathrm{II}}(l,z)=\phi_{\mathrm{IV}}(l,z)$ and $\frac{\partial\phi_{\mathrm{II}}(l,z)}{\partial x}=\frac{\partial\phi_{\mathrm{IV}}(l,z)}{\partial x}$ in Eqs. (3.63) and (3.65), respectively, the follow relationships are obtained for $(-\boldsymbol{h_s}\leq \boldsymbol{z}\leq 0)$.

$$\begin{aligned}
&A^-\cosh k^{II}(z+h_{II})\,e^{-ik^{II}l}+\sum_{n=1}^{\infty}B_n^-\cos k_n^{II}(z+h_{II})\,e^{-k_n^{II}l}\\
&\quad+A^+\cosh k^{II}(z+h_{II})\,e^{ik^{II}l}+\sum_{n=1}^{\infty}B_n^+\cos k_n^{II}(z+h_{II})\,e^{k_n^{II}l}\\
&\quad=E^-\cosh k(z+h)+\sum_{n=1}^{\infty}F_n^-\cos k_n(z+h)
\end{aligned}\tag{3.92}$$

$$\begin{aligned}
&-ik^{II}A^-coshk^{II}\,(z+h_{II})e^{-ik^{II}l}+\sum_{n=1}^{\infty}-k_n^{II}B_n^-cosk_n^{II}(z+h_{II})e^{-k_n^{II}l}\\
&\quad+\ ik^{II}A^+coshk^{II}(z+h_{II})e^{ik^{II}l}\\
&\quad+\sum_{n=1}^{\infty}k_n^{II}B_n^+cosk_n^{II}(z+h_{II})e^{k_n^{II}l}\\
&\quad=-ikE^-\cosh k(z+h)+\sum_{n=1}^{\infty}-k_nF_n^-\cos k_n(z+h)
\end{aligned}\tag{3.93}$$

Boundary between regions III and IV: Substituting Eqs.(3.89) and (3.91) into the conditions

$\phi_{\mathrm{III}}(l,z) = \phi_{\mathrm{IV}}(l,z)$ and $\frac{\partial\phi_{\mathrm{III}}(l,z)}{\partial x} = \frac{\partial\phi_{\mathrm{IV}}(l,z)}{\partial x}$ in Eqs.(3.64) and (3.66), respectively, the follow relationships are obtained for ($-\boldsymbol{h} \leq \boldsymbol{z} \leq -\boldsymbol{h_s}$).

$$\frac{1}{h_{III}}(C_0 + D_0 l) + \frac{2}{h_{III}}\sum_{m=1}^{\infty}\left\{\left(C_m \cosh\frac{m\pi}{h_{III}}l + D_m \sinh\frac{m\pi}{h_{III}}l\right)\cos\frac{m\pi}{h_{III}}(z+h)\right\}$$

$$= E^- \cosh k(z+h) + \sum_{n=1}^{\infty} F_n^- \cos k_n(z+h) \tag{3.94}$$

$$\frac{D_0}{h_{III}} + \frac{2}{h_{III}}\sum_{m=1}^{\infty}\left\{\left(C_m \sinh\frac{m\pi}{h_{III}}l + D_m \cosh\frac{m\pi}{h_{III}}l\right)\frac{m\pi}{h_{III}}\cos\frac{m\pi}{h_{III}}(z+h)\right\}$$

$$= -ikE^- \cosh k(z+h) + \sum_{n=1}^{\infty} -k_n F_n^- \cos k_n(z+h) \tag{3.95}$$

Final equation system: By assembling and arranging the equations derived in this section, the below system of equations is finally presented.

For $-\boldsymbol{h_s} \leq \boldsymbol{z} \leq 0$:

$$(A^- e^{-ik^{II}l} + A^+ e^{ik^{II}l}) cosh k^{II}\,(z+h_{II})$$
$$+ \sum_{n=1}^{\infty}(B_n^- e^{-k_n^{II}l} + B_n^+ e^{k_n^{II}l}) cos k_n^{II}(z+h_{II})$$
$$= E^- \, cosh\, k(z+h) + \sum_{r=1}^{\infty} F_r^- \, cos\, k_r(z+h)$$

(I)

$\phi_{II} = \phi_{IV}$

at $\boldsymbol{x} = \boldsymbol{l}$

Ref. to Eq.(3.92)

$$\left(-A^- e^{-ik^{II}l} + A^+ e^{ik^{II}l}\right) ik^{II} cosh k^{II}\,(z+h_{II})$$
$$+ \sum_{n=1}^{\infty}(-B_n^- e^{-k_n^{II}l} + B_n^+ e^{k_n^{II}l}) k_n^{II} cos k_n^{II}(z+h_{II})$$
$$= -ikE^- \cosh k(z+h) + \sum_{r=1}^{\infty} -k_r F_r^- \cos k_r(z+h)$$

(II)

$$\frac{\partial\phi_{II}}{\partial x} = \frac{\partial\phi_{IV}}{\partial x}$$

at $\boldsymbol{x} = \boldsymbol{l}$

Ref. to Eq. (3.93)

$$(-A^{-} + A^{+})ik^{II}coshk^{II}\,(z + h_{II}) + \sum_{n=1}^{\infty}(-B_n^{-} + B_n^{+})\,k_n^{II}cosk_n^{II}(z + h_{II}) = i\omega d$$

(III)

at $\boldsymbol{x} = \boldsymbol{l}$

$$\frac{\partial \phi_{II}}{\partial x} = i\omega d$$

Ref. to Eq. (3.77)

For $-\boldsymbol{h} \leq \boldsymbol{z} \leq -\boldsymbol{h}_{\boldsymbol{s}}$:

$$\frac{1}{h_{III}}(C_0 + D_0 l) + \frac{2}{h_{III}}\sum_{m=1}^{\infty}\left\{\left(C_m \cosh\frac{m\pi}{h_{III}}l + D_m \sinh\frac{m\pi}{h_{III}}l\right)\cos\frac{m\pi}{h_{III}}(z + h_{III})\right\} = E^{-} \cosh k(z + h) + \sum_{r=1}^{\infty} F_r^{-} \cos k_r(z + h)$$

(IV)

$$\phi_{III} = \phi_{IV}$$

at $\boldsymbol{x} = \boldsymbol{l}$

Ref. to Eq. (3.94)

$$\frac{D_0}{h_{III}} + \frac{2}{h_{III}}\sum_{m=1}^{\infty}\left\{\left(C_m \sinh\frac{m\pi}{h_{III}}l + D_m \cosh\frac{m\pi}{h_{III}}l\right)\frac{m\pi}{h_{III}}\cos\frac{m\pi}{h_{III}}(z + h_{III})\right\} = -ikE^{-} \cosh k(z + h) + \sum_{r=1}^{\infty} -k_r F_r^{-} \cos k_r(z + h)$$

(V)

$$\frac{\partial \phi_{III}}{\partial x} = \frac{\partial \phi_{IV}}{\partial x}$$

at $\boldsymbol{x} = \boldsymbol{l}$

Ref. to Eq.(3.95)

$$\frac{D_0}{h_{III}} + \frac{2}{h_{III}}\sum_{m=1}^{\infty} D_m \frac{m\pi}{h_{III}} cos\frac{m\pi}{h_{III}}(z + h_{III}) = i\omega d$$

(VI)

at $\boldsymbol{x} = 0$

$$\frac{\partial \phi_{III}}{\partial x} = i\omega d$$

Ref. to Eq.(3.90)

Where A^{-}, A^{+} and E^{-} are the complex constants which represent the incident, reflected and transmitted waves, respectively. B_n^{-}, $B_n^{+}$and F_r^{-} represent the evanescent mode of such waves which vanish at $\boldsymbol{x}$ → ∞. On the other hand, C_0, C_m, D_0 and D_m are complex constants to be determined by applying a numerical method to solve the boundary problem, which will be discussed in the upcoming section.

3.3.2 *Caisson with Twin Horizontal Plates*

The velocity potential for the caisson with twin plates follows the general form for the velocity potential defined by Eq.(3.59), where $\boldsymbol{\phi_j}$ is a superposition of the progressive wave and the decaying wave (evanescent mode wave), and subscript ***j*** = ***I***, ***II***, ***III***, ***IV*** indicates the regions of the model. For this case: Region I is the free surface in the seaside of the caisson, Region II is the fluid area within the plate at the surface and the submerged plate, Region III is the fluid area between the submerged plate and the seabed, while Region IV is the harborside area located after the plate.

3.3.2.1 Boundary and Continuity Conditions.

According to the wavemaker theory explained in the previous sections, the condition of movement of the caisson is defined by the boundary at the caisson walls as in Eq.(3.60), while the conditions at the bottom and under and above the plate are shown in Eq.(3.96). Laplace equation for the regions is defined in Eq. (3.62), and the continuity conditions in the horizontal plane between regions are expressed from Eq. (3.63) to Eq. (3.66).

$$\frac{\partial \phi_j}{\partial x} = i\omega d\,;\;\; x = -B\ (j = I);\; x = 0\ (j = II, III)$$

Ref. to Eq.(3.60)

$$\frac{\partial \phi_j}{\partial z} = 0\ \ ;\ \ z = 0\ (j = II) z = -h_s\ (j = II, III);\; z = -h\ \ (j = III)$$

(3.96)

$$\frac{\partial^2 \phi_j}{\partial x^2} + \frac{\partial^2 \phi_j}{\partial z^2} = 0\ \ ;\ \ (j = II, III, IV)$$

Ref. to Eq.(3.62)

$$\phi_{\mathrm{IV}}(l, z) = \begin{cases} \phi_{\mathrm{II}}(l, z) & (0 \geq z \geq -h_s) \\ \phi_{\mathrm{III}}(l, z) & (-h_s \geq z \geq -h) \end{cases}$$

Ref. to Eq.(3.63) Eq.(3.64)

$$\frac{\partial \phi_{\mathrm{IV}}(l,z)}{\partial x} = \begin{cases} \dfrac{\partial \phi_{\mathrm{II}}(l,z)}{\partial x} & (0 \geq z \geq -h_s) \\ \dfrac{\partial \phi_{\mathrm{III}}(l,z)}{\partial x} & (-h_s \geq z \geq -h) \end{cases}$$

Ref. to
Eq.(3.64)
Eq.(3.65)

3.3.2.2 *Final Analytical Expression for the Boundary-value Problem*

The derivation of the velocity potential for Regions I and III remains the same as in section 0. In contrast, the new Region II has the same conditions as Region III; thus, the velocity potential is defined as in Region III as well. Please notice that in this case, the unknown coefficients have the superscript ***j*** as a note that they are not the same values.

Then, for all *0 ≥ **z** ≥ -**h**ₛ*, the system of equations is determined by Eqs. (3.97), (3.98) and (3.99), where ***j****=II, III* representing Regions II and III for a total of six general expressions. Notice that ***z*** is globally measured from water surface to seabed even if is within the expression of velocity potential for a region with water depth smaller than the overall water depth. Furthermore, parameters in Region IV are not defined with superscripts since they match the ones related to total free surface water depth.

$$\frac{1}{h_j}\left(C_0^j + D_0^j l\right) + \frac{2}{h_j}\sum_{m=1}^{\infty}\left(C_m^j \cosh\frac{m\pi}{h_j} l + D_m^j \sinh\frac{m\pi}{h_j)} l\right)\cos\frac{m\pi}{h_j}(z+h_j)$$
$$= E^- \cosh k(z+h) + \sum_{n=1}^{\infty} F_n^- \cos k_n(z+h)$$

(3.97)
at $x = l$
(I and IV)

$$\frac{D_0^j}{h_j} + \frac{2}{h_j}\sum_{m=1}^{\infty}\left(C_m^j \sinh\frac{m\pi}{h_j} l + D_m^j \cosh\frac{m\pi}{h_j} l\right)\frac{m\pi}{h_j}\cos\frac{m\pi}{h_j}\left(z+h_j\right)$$
$$= -ikE^- \cosh k(z+h) + \sum_{n=1}^{\infty} -k_n F_n^- \cos k_n(z+h)$$

(3.98)
at $x = l$
(II and V)

$$\frac{D_0^j}{h_j} + \frac{2}{h_j}\sum_{m=1}^{\infty} D_m^j \frac{m\pi}{h_j}\cos\frac{m\pi}{h_j}\left(z+h_j\right) = i\omega d$$

(3.99)
at $x = 0$
(III and VI)

3.4 SOLUTION OF THE BOUNDARY-VALUE PROBLEM. BOUNDARY-POINT SELECTION METHOD

[Enhanced subsection based on the previous work of the author in Fundora (2021) and Fundora and Aoki (2023)]

The Boundary Point Selection Method BPSM (Yoshida et al., 1990) is used to solve the velocity potential in each region (Fundora and Aoki, 2023, 2024), i.e., determine the values of the unknowns presented in the preceding section: A^-, A^+, B_n^-, B_n^+, C_0, D_0, C_m, D_m, E^- and F_r^-. The examples of unknowns and equations in this subsection refer to the single submerged plate as a reference, but it can also be applied to the twin plates model. The application of the method replaces integral and differential calculus with solutions expressed as algebraic equations. By specifying that the potential equations for the regions with shared boundaries and their derivatives hold (converge) on the calculation points, a linear relational expression with respect to the unknown coefficients is obtained, allowing the determination of the value for such coefficients.

The *potential connection* method, *regional division* method, or *collocation method* (it has been diversely named) was one of the leading analysis methods for the boundary value problem of waves, according to Ijima et al. (1971). It is due to some advantages that will be explained further in this section that it has been used by researchers such as the same Ijima et al. (1971), Black et al. (1971), Goda et al. (1976), Mcluver (1986), Wu and Liu (1988), and Yoshida et al. (1989) for the wave-proofing function of coastal structures and the analysis of floating structures.

For the practical application of the BPSM, the physical boundary $\mathbf{x} = \boldsymbol{l}$ is divided into sections, a point within each section is selected (see a representation in Figure 3.8), and the six main equations of the system resumed in subsections are set to be satisfied in those points: Eqs. (3.92), (3.93) and (3.77) for $(0 \geq z \geq -h_s)$ and Eqs. (3.94), (3.95) and (3.90) for $(-h_s \geq z \geq -h)$.

Each selected point (z) gets associated the number of initial equations and several unknowns depending on the maximum value of $\boldsymbol{m}$, $\boldsymbol{n}$ and $\boldsymbol{r}$, i.e., series term truncation in $\boldsymbol{\phi}_{\mathbf{II}}$, $\boldsymbol{\phi}_{\mathbf{III}}$ and $\boldsymbol{\phi}_{\mathbf{IV}}$, respectively. The truncation is such that the number of final equations obtained along the water depth $\boldsymbol{h_j}$ matches the number of final unknowns, leading to the solution of the equation system.

From applying the method to submerged plates, the following relations arise $\boldsymbol{n} + \boldsymbol{m} = \boldsymbol{r} - 1$ and $\boldsymbol{n} + \boldsymbol{m} + \boldsymbol{2} = \boldsymbol{Z_{II}} + \boldsymbol{Z_{III}}$, where $\boldsymbol{Z_j}$ is the total number of points selected in a region. However, although such relations should hold for all-natural $\boldsymbol{n}$, $\boldsymbol{m}$ and $\boldsymbol{r}$, errors or unstable solutions are obtained for some combinations. Thus, the best approach has been proven by applying $\boldsymbol{n} = \boldsymbol{Z_{II}} - 1$, $\boldsymbol{m} = \boldsymbol{Z_{III}} - 1$ and $\boldsymbol{r} = \boldsymbol{Z_{IV}} - 1$. This is consistent with Yoshida et al. (1990), who concluded that: "(…) if the number of series terms in each region is taken as the number of calculation points on the boundary, the square error is the smallest and a good solution is obtained; adding that it is enough to take a series term corresponding to the number of calculation points determined by the interval".

When applying the BPS method, taking the initial or/and final point of a section is also possible, and it does not constitute a problem in this initial setup. However, in Yoshida et al. (1990), different arrangements were tested for various problems (Figure 3.11). Also, although results were the same in almost all cases, taking initial points when others submerged in-line structures were analyzed (case A-2) outputted inaccurate results. Thus, since the inclusion of submerged structures is planned in this study's further stages, stable results for such variations and inclusions are needed. Then, the midpoints are taken for analysis.

Additionally, to test the influence of the number of selected points (**Z**) on the accuracy and suitability of the method, the analysis was made for a different number of points (**Z**=10,20,30,40,80). As expected, a higher number of **Zs** led to more accurate values (compared with the respective analytical solution). However, in cases where the section's length became a number with infinite or repeating decimal (e.g., $\mathbf{Z}$=30 with a section length of $0.26\overline{6}$), the solution was inaccurate. That adds another recommendation: Section's length $\notin$ Q repeating decimal.

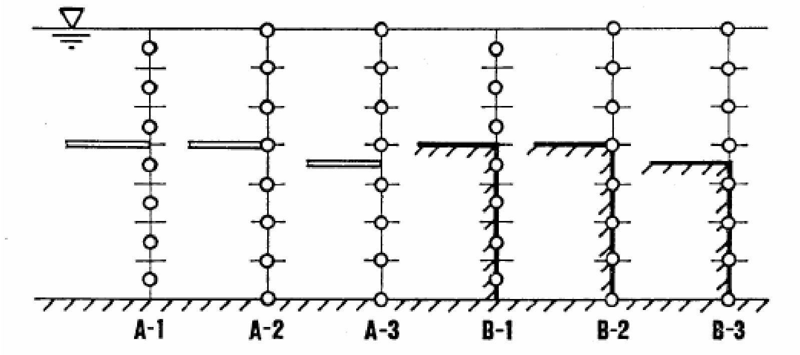

Figure 3.11. Arrangement of calculation points in the point selection method for an isolated plate and a submerged wall. (Yoshida et al., 1990)

Although it is reasonable to think that applying a more significant number of selected $\boldsymbol{z}$, $\boldsymbol{m}$, $\boldsymbol{n}$ and $\boldsymbol{r}$ will better approximate the exact solution of the velocity potentials $\boldsymbol{\phi}$; this practice leads to unstable and inaccurate solutions. However, selecting many points is unnecessary since relatively small ratios of the section's length to the water's depth $\boldsymbol{h_s/h}$ and $\boldsymbol{(h-h_s)/h}$, such as 1/10 or 1/20, lead to accurate solutions.

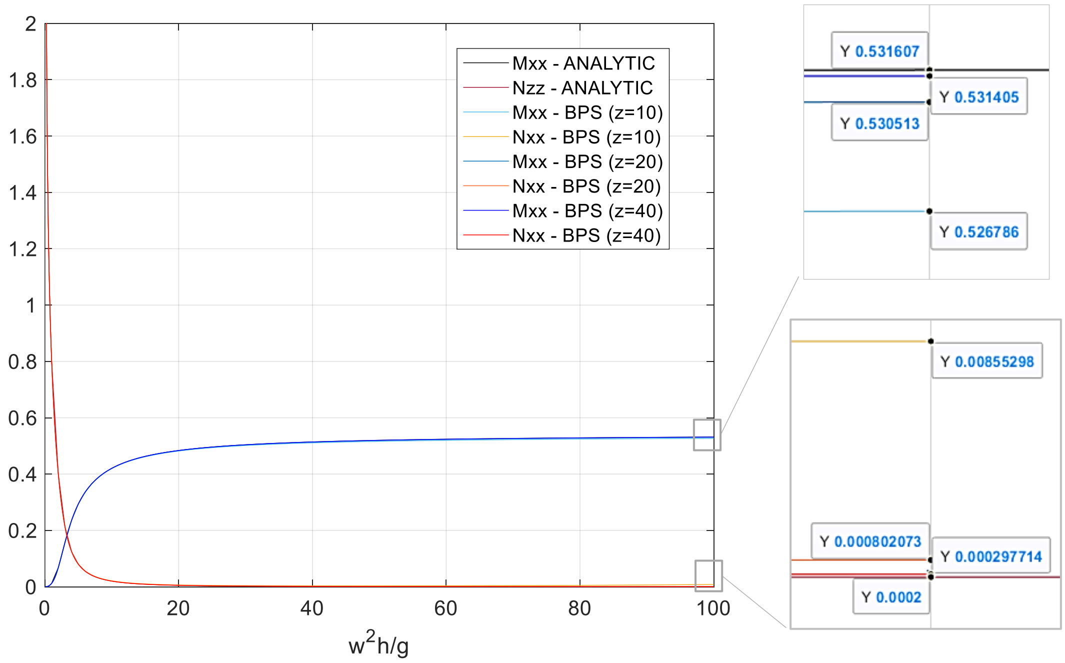

Figure 3.12. Comparison between the solutions by conventional and by BPS method in region III ($\boldsymbol{l}$=0). (Fundora, 2021)

An example of its suitability and accuracy is that the BPSM solutions in Region I of the study case match the conventional (analytical) method solutions. Low Root Mean Square errors RMSE indicating good fits, especially for **Z_{IV}** ≥ 20, can be seen in Figure 3.12. Comparisons are made with the conventional method applied in Aoki et al.(1995) for Region I and with solutions in Yoshihara (2019) for Region II (case *l/h≈0, l/h=0.0001*, i.e., *l* = 1cm for the case of *h*=8m). More so, in analyzing R-squared errors, values of approximately 1 are the rule as in Table 3-3, which implies an almost perfect match or prediction. Even though the suitability and accuracy of the method are initially tested in Region I and III (for ***l***=0, noticed in that area, the conventional analysis is easy; thus, the application of the BPSM is not particularly necessary. On the other hand, the traditional method is tedious and difficult in Region II, III and IV due to evaluating the integrals related to the eigenfunctions. Therefore, in those regions, the BPS method became helpful and practical.

Table 3-3. RMSE and R-squared for solutions applying BPSM with different points number (Z) in Region I and II (l/h=0). Comparison with results by the conventional method. (Fundora, 2021)

		RMSE		R^2			RMSE		R^2	
Z		M_{xx}	N_{xx}	M_{xx}	N_{xx}		M_{xx}	N_{xx}	M_{xx}	N_{xx}
10	REGION I	2.E-03	3.E-03	0.99996	0.99998	REGION II	2.E-03	5.E-04	0.99996	1.00000
20		5.E-04	3.E-04	1.00000	1.00000		2.E-04	3.E-04	1.00000	1.00000
40		9.E-05	7.E-05	1.00000	1.00000		5.E-05	3.E-04	1.00000	1.00000
80		2.E-05	1.E-05	1.00000	1.00000		9.E-05	3.E-04	1.00000	1.00000

In general, the application of the method leads to a good match with analytical solutions. The advantages include simplifying the theoretical formulations and computer programming, lower computer memory required for the numerical calculation, and short calculation time. However, this method is limited to cases where the flow area can be divided into rectangular shapes. That is a disadvantage if compared to the finite difference (FDM), boundary element (BEM), or finite element (FEM) methods.

An admissible error of 1.E-03 is settled; thus, the analysis for the cases of study is made by applying the BPSM with 20 sections or points (Z=20), i.e., $\boldsymbol{Z_{IV}} = 20$, while $\boldsymbol{Z_{II}}$ and $\boldsymbol{Z_{III}}$ will depend on the submersion depth $\boldsymbol{h_s}$. The previous statements apply to the caisson with the plate at the surface and to single submerged plates at more than ¼ of the total water depth. For the case of single submerged plates with small submersion depths, the application of the method does not yield a solution. The reason is that the BPSM is basically a numerical technique; thus, when there is low free water surface depth on top, there is a smaller number of calculation points in that region over the plate and fewer series terms, making it more difficult to the whole system to converge a solution for the number of unknowns. Accordingly, a total of 40 points ($\boldsymbol{Z_{IV}} = 40$) will be used for the cases where the plate is located over such depth. This effect is not seen in the no-free surfaces, i.e., region under the plate, since the boundary conditions determine a more stable flux. There, the governing equations are derived so that the terms within the series are not directly frequency dependent, which translates to no wave number values in the velocity potential equations under the plate.

Furthermore, to simplify the procedure, the initial deformation d in the equation system is selected as unitarian, i.e., $d = 1$. This means that the obtained coefficients and results are divided by d. When not working dimensionless, to get the real value of the coefficients, the values obtained directly from the application of the method (elements with superscript *'calc'*) should be multiplied by d. ($A = dA^{cal}$, $B_n = dB_n^{cal}$, $C_o = dC_o^{cal}$, $D_o = dD_o^{cal}$, $C_m = dC_m^{cal}$, $D_m = dD_m^{cal}$).

Resuming the main recommendations for the application of the method:

a) Selecting sections' midpoints as calculation points to avoid inconsistent results. b) Taking the number of series terms in each region as the number of calculation points on the region boundary. c) Avoiding sections' length with repeating decimal values. d) Using ratios of section's length to water's depth $\boldsymbol{h_s / h}$, such as 1/10 or 1/20, that, although relatively small, lead to accurate solutions. e) Redefining the sections’ length to $\boldsymbol{h}$ /40 for regions over the plate with free water surface around a quarter of the water depth and a small number of calculation points.

3.5 PRESSURE, FORCES AND HYDRODYNAMIC COEFFICIENTS.

If the boundary-value problem is solved, the velocity potential for each region is obtained; thus, physical properties such as pressure and forces can be derived from it. From the latter's breakdown, the hydrodynamic coefficient can be obtained and used in the sliding simulation.

3.5.1.1 *Pressures and Forces*

The general expression for the pressure in the regions of the model applying Eq. (3.59) for the velocity potential $\Phi_j(x,z,t) = \phi_j(x,z)e^{i\omega t}$ is defined by Eq.(3.100). Since the solution for velocity potential derived in sections 3.3 and 3.4 is $\phi_{j(x,z)}$, then the general expression for the pressure is given by Eq.(3.101). The sign implies the direction of the acting pressure. Considering for the horizontal pressure acting on the wall, a negative value in the direction against the movement as a reaction, and for the vertical pressure on the plate: negative upwards and positive downwards.

$$p_{j(x,z,t)} = -\rho\frac{\partial\Phi_j(x,z,t)}{\partial t} = -\rho\frac{\partial\phi(x,z)e^{i\omega t}}{\partial t} = -i\rho\omega\phi_{j(x,z)}e^{i\omega t} \tag{3.100}$$

$$p_{j(x,z)} = \pm i\rho\omega\phi_{j(x,z)} \tag{3.101}$$

$$F_{xx}|_{(x=-B)} = \int_{-h}^{0} p_{(-B,z)}dz \tag{3.102}$$

$$F_{xx}{}^{II}|_{(x=0)} = -\int_{-h_s}^{0} p_{II\,(0,z)}dz \tag{3.103}$$

$$F_{xx}{}^{III}|_{(x=0)} = -\int_{-h}^{-h_s} p_{III\,(0,z)}dz \tag{3.104}$$

$$F_{zx}{}^{j}|_{(z=-h_s)} = \int_{0}^{l} p^{j}{}_{(x,-h_s)}dx \quad ;j = II, III \tag{3.105}$$

Accordingly, and as an example, the pressure for Region III under the horizontal plate at the surface can be expressed as Eq.(3.106). Thus, the pressure acting horizontally on the vertical wall (*x*=0) and the pressure acting vertically below the horizontal plate (z=0) is determined by Eqs. (3.107) and (3.108), respectively.

$$p_{III(x,z)} = -i\rho\omega\left\{\frac{1}{h_{III}}(C_0 + D_0 l) + \frac{2}{h_{III}}\sum_{m=1}^{\infty}\left[\left(C_m \cosh\frac{m\pi}{h_{III}}l + D_m \sinh\frac{m\pi}{h_{III}}l\right)\cos\frac{m\pi}{h_{III}}(z + h_{III})\right]\right\}e^{i\omega t} \tag{3.106}$$

$$p_{III(0,z)} = -\frac{i\rho\omega}{h_{III}}\left\{C_0 + 2\sum_{m=1}^{\infty} C_m cos\frac{m\pi}{h}(z + h_{III})\right\}e^{i\omega t} \tag{3.107}$$

$$p_{III(0,z)} = -\frac{i\rho\omega}{h_{III}}\left[(C_0 + D_0 x) + 2\sum_{m=1}^{\infty}(C_m cosh\frac{m\pi}{h}x + D_m sinh\frac{m\pi}{h}x)cosm\pi\right]e^{i\omega t} \tag{3.108}$$

Accordingly, the force acting on the vertical wall (*x*=0) can be expressed as Eq.(3.109) and since $\boldsymbol{m} \in \mathbb{N}$, $\sin m\pi = 0$, thus the second term of the sum is canceled, yielding to Eq.(3.110). On the other hand, Eqs. (3.111) and (3.112) define the forces acting below the horizontal plate at the surface.

$$F_{xx} = -\int_{-h}^{0} p_{(0,z)}dz = i\rho\omega\left(C_0 + \frac{2}{\pi}\sum_{m=1}^{\infty}\frac{C_m}{m}\sin m\pi\right)e^{i\omega t} \tag{3.109}$$

$$F_{xx} = i\rho\omega C_0 e^{i\omega t} \tag{3.110}$$

$$F_{zx} = \int_{0}^{l} p_{(x,0)}dx \tag{3.111}$$

$$F_{zx} = \left[-\frac{i\rho\omega}{h}\left(C_0 l + \frac{1}{2}D_0 l^2\right) - \frac{2i\rho\omega}{\pi}[\frac{C_m}{m}sinh\frac{m\pi}{h}l + \frac{D_m}{m}(cosh\frac{m\pi}{h}l - 1)]cosm\pi\right]e^{i\omega t} \tag{3.112}$$

The above derivation for the case of a caisson with a single plate at the surface proves useful as an explanation. However, there are other cases with all the regions involved in the analysis and the derivation can become overwhelming. That's when the numerical techniques become handy. The application of the BPSM yields to the numerical obtention of the unknown coefficient of the velocity potentials. Therefore, directly inputting the expressions of the velocity potential in the general equations for pressures and forces, recalling the values for the coefficients now known and doing the mathematical integrations over the limits for each region proves to be more efficient without further derivations.

3.5.1.2 Hydrodynamic coefficients: Added Mass, Damping Coefficient and Memory-effect Function.

Added Mass and Damping Coefficient

The force expression in Eq.(3.33) displays the direct relation between additional mass *M* and damping coefficient ***N*** with acceleration and velocity, respectively. Accordingly, since $\boldsymbol{\xi = de^{i\omega t}}$, it is possible to obtain the additional mass ***M*** by dividing the Real part of the force by $\boldsymbol{\omega^2 d}$; while the division of the Imaginary part of the force value by $\boldsymbol{-d\omega}$ yields to the damping coefficient ***N***.

$$F = -N\frac{d\xi}{dt} - M\frac{d^2\xi}{dt^2} \qquad \text{Ref. to Eq.(3.33)}$$

$$\frac{d\xi}{dt} = i\omega d e^{i\omega t} \tag{3.113}$$

$$\frac{d^2\xi}{dt^2} = -\omega^2 d e^{i\omega t} \tag{3.114}$$

Equivalent to the final derivation of the unknown coefficient in the velocity potential equations, as stated at the end of subsection 3.4, from the direct application of the BPSM using $\boldsymbol{d}$ =1, the final values of the force are $\boldsymbol{F=F^{calc}*d}$. Thus, in practical calculations of added mass ***M*** and damping ***N*** coefficients, the value of a real ***d*** is eliminated, and the analysis is made with the real and imaginary parts of $\boldsymbol{F^{calc}}$.

$$M = \frac{Re(F)}{\omega^2 d} \quad \text{i.e.} \quad M = \frac{Re(F^{calc})}{\omega^2} \tag{3.115}$$

$$N = \frac{Im(F)}{-\omega d} \quad \text{i.e.} \quad N = \frac{Im(F^{calc})}{-\omega} \tag{3.116}$$

Memory-effect Function

For the derivation of the memory-effect function ***R(t)***, or its dimensionless equivalent, let's first recall the equation for the memory-effect function from Eq.(3.47) reflecting the effect of the caisson's initial motion on the fluid force after a time ***t***, to see the direct dependence on the damping coefficient.

$$R(t) = \frac{2}{\pi}\int_0^\infty N(\omega)\cos\omega t\, dt$$

Ref. to Eq.(3.47)

Thus, two approaches can be utilized for its derivation: one based on the values of ***N(ω)*** itself or directly substituting the expression of its curve. In the first approach, the ***N*** values for each frequency ***ω*** obtained in the previous steps are used to calculate the exact value of ***R(t)***. However, the values for the integration are limited by the frequency range utilized. This can be solved by using a wide range of frequencies; in this study, values of dimensionless frequency ***ω**** = [0,100] provided a good match. For the second approach, a fitting curve tool is utilized to represent and predict the behavior of ***N(ω)*** and obtain the expression of its curve. The damping coefficient curves follow the representation of Gaussian functions. Thus, such a fitting curve is used. The general expression can be seen in Eq.(3.117).

$$f(x) = \sum_{1}^{n} a_n e^{-\left[\frac{(x-b_n)}{c_n}\right]^2} \tag{3.117}$$

Where a_n represents the height of the curve's peak, b_n the position of the center of the peak, c_n the standard deviation, ***e*** the Euler's number, and ***x*** the integer (in this case, the frequency). The advantages of this approach are that it covers infinite values of ***N(ω)*** and represents less workload for the process, while the con is that fitting curves are approximations, although with minimal errors. Therefore, the latest approach will be used. The fitting curve tool embedded in MATLAB will be used with this end.

Total Hydrodynamic Coefficients

Furthermore, although independent values will be analyzed to understand the physical phenomenon, the total value of the hydrodynamic parameters will be utilized for the practical solution and defined as below.

$$M(\omega)^{total} = \sum_{j=I}^{III} M_{xx} + f\sum_{j=I}^{III} M_{xz} \tag{3.118}$$

$$M\infty^{total} = \lim_{\omega\to\infty} M(\omega)^{total} \tag{3.119}$$

$$N(\omega)^{total} = \sum_{j=I}^{III} N_{xx} + f\sum_{j=I}^{III} N_{xz} \tag{3.120}$$

$$R(t)^{total} = \frac{2}{\pi}\int_0^{\infty} N(\omega)^{total} \cos\omega t \, dt \tag{3.121}$$

3.6 SLIDING

The sliding model is an idealized 2D lumped system with one degree of freedom: horizontal translation. The equation describing the motion of a regular breakwater (without a horizontal plate) was defined as $(m + M_\infty)\ddot{x} + \int_0^t R(t-\tau)\dot{x}(\tau)d\tau = F(t) - F_f$ in subsection 3.1.4. Such expression was used to determine the sliding of the caisson taking constant added mass M_{xx}^{∞} as $1.0855\rho h^2$. Furthermore, many researchers also dismissed the parameters related to the motion velocity for that geometry. Besides, even considering the full expression, only $\boldsymbol{M_{xx}}$ and $\boldsymbol{N_{xx}}$ for $\boldsymbol{R_{xx}}$ were used, as shown in Eq.(3.122), since vertical forces were dismissed in the analysis.

$$(m + M_{xx}^{\infty})\ddot{x} + \int_0^t R_{xx}(t-\tau)\dot{x}(\tau)d\tau = F(t) - F_f \tag{3.122}$$

However, with the addition of the horizontal plate, uplift or vertical forces are more influential in the system, and the friction force is not constant. Thus, $\boldsymbol{M_{zx}}$ and $\boldsymbol{N_{zx}}$-$\boldsymbol{R_{zx}}$ from those forces are introduced in the motion equation as part of the friction force. In the case of the regular caisson, the frictional force is equal to $\boldsymbol{F_f} = \boldsymbol{f_f} * \boldsymbol{W_w}$. That force for the caisson with the horizontal plate is expressed by Eq.(3.123), whereas the uplift force $\boldsymbol{V}$ is given by Eq.(3.124).

$$F_f = f_f(W_w - V) \tag{3.123}$$

$$V = M_{zx}\,\ddot{x} + N_{zx}\dot{x} \tag{3.124}$$

$$F_f = f_s(m_w g + M_{zx}^{\infty}\,\ddot{x} + N_{zx}\dot{x}) \tag{3.125}$$

Substituting the above equations into Eq.(3.122), the final expression for the motion is defined below. Therefore, our final parameter of interest, the displacement ($\boldsymbol{x}$ term), can be obtained in a time range by solving Eq.(3.126) employing a numerical solver that applies the Runge-Kutta technique to solve the system of differential equations.

$$(m_a + M_{xx}^{\infty} - f_s M_{zx}^{\infty})\ddot{x} + \int_0^t [R_{xx}(t-\tau) - f_s R_{zx}(t-\tau)]\dot{x}(\tau)d\tau = \begin{Bmatrix} \alpha F_s \dfrac{t}{t_p}; & (0 \le t \le t_p) \\ \alpha F_s\left(2 - \dfrac{t}{t_p}\right); & t_p \le t \end{Bmatrix} \tag{3.126}$$

Chapter 4. ANALYTICAL STUDY: PRACTICAL IMPLEMENTATION AND DISCUSSION.

OUTLINE

A practical implementation and results analysis of the theoretical development derived in Chapter 3 is conducted in the following chapter to investigate the effect of horizontal plates on the performance of a vertical breakwater during the failure process by simulating the caisson sliding under impulsive wave loads. It includes outputs and discussion on pressure distributions, hydrodynamic coefficients (added mass, damping coefficient and memory effect function), and caisson sliding due to different arrangements of plates according to location, length, and submersion depth. The analysis is mainly divided into cases of caissons with a single horizontal plate (at the water surface and submerged) and with twin plates, including the comparison with the results from the absence of a plate (typical vertical caisson) with the objective of determining differences on models results and effectiveness of the different arrangements.

4.1 CAISSON WITH A SINGLE HORIZONTAL PLATE. COMPARISON

The effect of the single horizontal plate on the estimation of the hydrodynamic characteristics due to fluid-structure interaction and sliding of caissons with a single plate is presented and analyzed in this subsection. The first focus is on the influence of the plate length, which is analyzed for caisson with a single plate at the surface. Using the latter's best performances, the plate's submersion depth is then analyzed. All the analyses include the comparison with the regular caisson (without plate).

The model described in Chapter 3, representing a breakwater with a single horizontal plate, is used for the analysis. The length of the plate is initially tested on the plate at the surface, where a more extensive water body is compressed. Four lengths of the plate will be analyzed based on the ratio ‘plate length’ to ‘water depth’ $\boldsymbol{l/h}$ = 0, 0.25, 0.5, 0.75 and 1. The ratio $\boldsymbol{l/h}$ = 0 corresponds to the case of regular caisson (without plate). For the plate submersion analysis, another three submersion depths are added, and the following ratio of 'submersion depth' to 'water depth' $\boldsymbol{h_s}/\boldsymbol{h}$ from 0 to 1 with a step of 0.1 including the locations $\boldsymbol{h_s} = 0.25\boldsymbol{h}$ and $\boldsymbol{h_s} = 0.75\boldsymbol{h}$. For the submersion analysis, the ratio $\boldsymbol{h_s}/\boldsymbol{h} = 0$ corresponds to a selected case from the plate length analysis and $\boldsymbol{h_s}/\boldsymbol{h} = 1$ to a regular caisson (without plate). Refer to Figure 4.1.

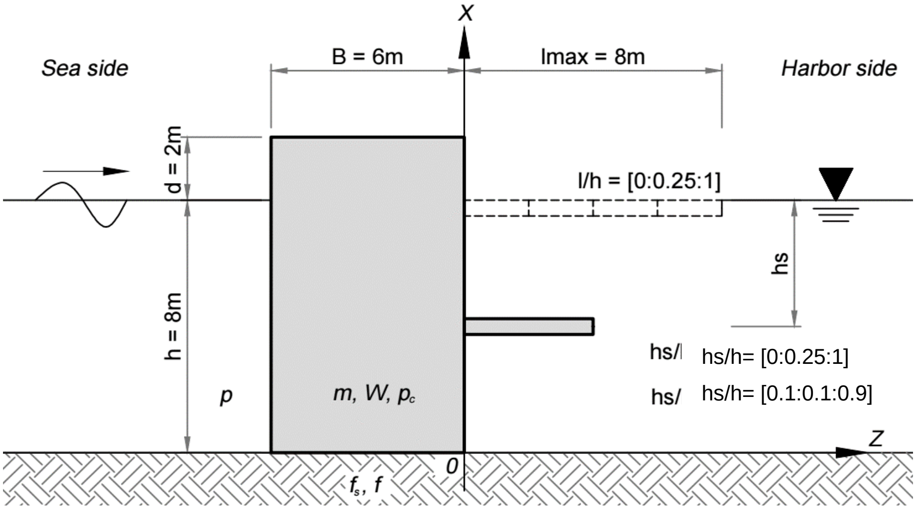

Figure 4.1. Representation of the single plate model with the cases of analysis for plate length and submersion depth.

A dimensional analysis is made based on the purpose of obtaining concrete values. The model dimensions and properties, as well as the initial parameters for the sliding calculations, correspond to those used for the BPS method in Chapter 3, but are reminded below.

$\boldsymbol{h} = 8\text{m} \quad \boldsymbol{B} = 6\text{m} \quad \boldsymbol{d} = 2\text{m} \quad \boldsymbol{\rho} = 1000\text{kg/m}^3$

$\boldsymbol{\rho_c} = 2150\text{kg/m}^3 \quad \boldsymbol{f}=\boldsymbol{f_s}=0.6 \quad \boldsymbol{\alpha}=0.1 \quad \boldsymbol{t_p}=0.5\text{s}$

where $\boldsymbol{\rho}$ and $\boldsymbol{\rho_c}$ are water and concrete density, respectively; $\boldsymbol{\alpha}$ the wave force magnitude; $\boldsymbol{fs}$ and $\boldsymbol{f}$ the static and dynamic frictional coefficient, respectively; and $\boldsymbol{t_p}$ the time instant where the maximum external force $\boldsymbol{F_{max}}$ is reached. However, a dimensionless analysis is made as a rule for easier comparisons. The parameters to be used and their dimensionless expressions are displayed in Table 4-1.

Table 4-1. Parameters related to linear wave theory and dimensionless expressions.

Parameter	**Symbol**	**Dimensionless expression**
Mass	m	$m^* = \frac{m}{\rho h^2}$
Weight	W	$W^* = \frac{W}{\rho h^2 g}$
Displacement	X	$X^* = \frac{X}{h}$
Time	t	$t^* = \sqrt{\frac{g}{h}}t$; $t_p{}^* = \sqrt{\frac{g}{h}}t_p$; $\tau^* = \sqrt{\frac{g}{h}}\tau$
Frequency	ω	$\omega^* = \omega^2 \frac{h}{g}$; $\omega^* = \omega\sqrt{\frac{h}{g}}$
Added Mass	M	$M^* = \frac{M}{\rho h^2}$
Damping Coefficient	N	$N^* = \frac{N}{\rho\omega h^2}$; $N(\omega^*)^* = \frac{N(\omega\ )}{\rho\sqrt{gh^3}}$
Memory-effect Function	R	$R(t^*)^* = \frac{R(t)}{\rho g h}$

Note: In the analysis below, ω^* is referring to the form $\omega^2 \frac{h}{g}$

4.1.1 *Pressure Analysis*

The frequency range for applying the methodology is ω* = [0 - 100]. While the estimation for the hydrodynamic parameters is ω* →∞. However, in order to easily observe and understand the pressure behavior on the plate and the caisson wall, a reduced number of frequencies will be used for the pressure distribution comparison, that is the case of ω* = [0.1, 5, 10, 15, 20]. The geometric range of analysis is along all water depth ***z*** = [0~1]***h*** and all the plate lengths for each case ***x*** = [0~1]***l***. Furthermore, the analysis will include comparisons taking into account the complex value of the pressure, as well as only the real component to better define the behavior.

Single plate at the surface (Plate Submersion: $\boldsymbol{h_s}$*=0. Plate length:* ***l/h****=0.5)*

(Real and imaginary components of the pressures)

The pressure distribution on the wall (Figure 4.2 - left) displays more uniformity for lower frequencies. Higher values of pressure correspond to higher frequencies. Furthermore, the

Imaginary part (related to damping) is more relevant for small frequencies and tends to zero for higher frequencies.

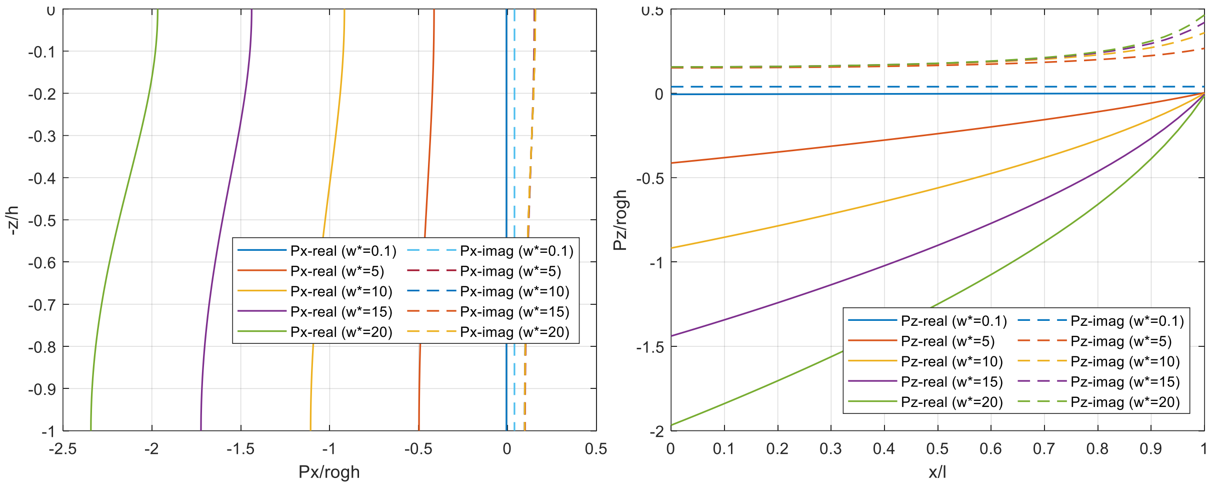

Figure 4.2. Pressure distribution acting on the wall(left) and the plate(right) for different frequencies. Single plate at z=0. (Complex arguments)

The pressure distribution under the plate (Figure 4.2 - right) exhibits more significant pressures near the wall while tending to 0 when reaching the plate tip. The imaginary part slightly increases near the tip; this is related to the fact that in that zone, there are more effects related to the damping process due to the change of boundary conditions, so the impact of the fluid in the region behind the plate affects it more.

Submerged Plate (Plate Submersion: $\mathbf{h_s}$*=0.5. Plate length:* ***l/h****=0.5)*

(Real and imaginary components of the pressures)

The overall pressure distribution on the wall (Figure 4.3) is interrupted due to the plate and variates due to the different boundary conditions. The distribution over the plate corresponds to the ones for a monolithic caisson (no plate-free surface). An almost uniform distribution is seen under the plate with higher pressure values than the upper region (more than double). Additionally, the imaginary part of the pressures is more representative near the surface.

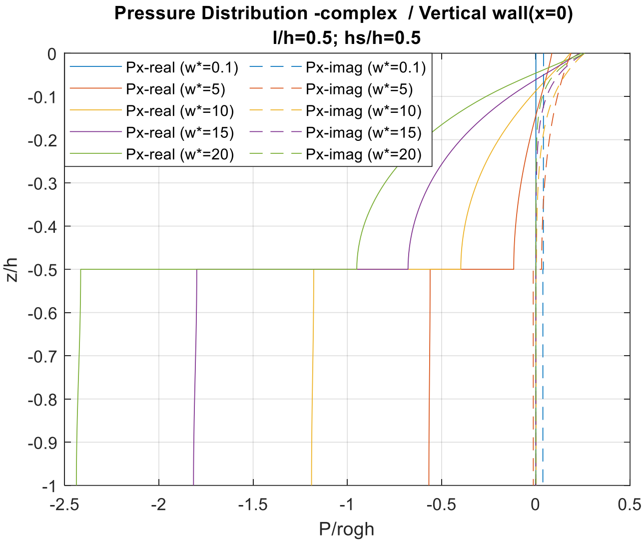

Figure 4.3. Pressure distribution acting on the wall for different frequencies. Single plate at z=h/2. (Complex argument)

The pressure distribution on the plate (region II) and under it (region III) and the total pressure are seen in Figure 4.4. When analyzing the horizontal distribution on the wall (per region), the pressures under the plate double the pressures over it, presenting a more linear distribution. The pressures over the plate are slightly higher near the wall and show a sort of parabolic behavior, increasing at the tip (without reaching those at ***x***=0).

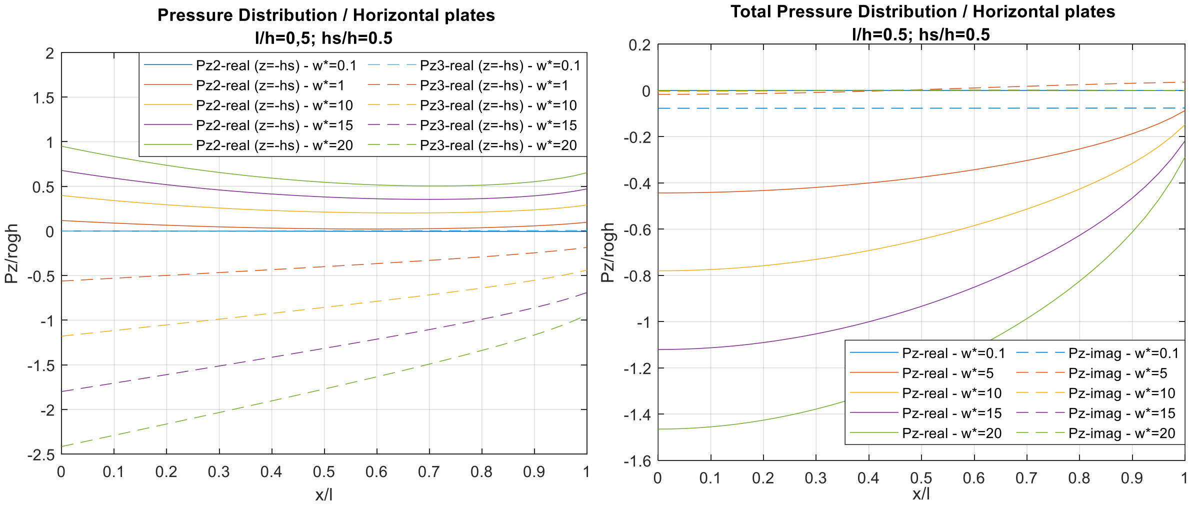

Figure 4.4. Pressure distribution acting on the plate(right) for different frequencies total(right) and per region (left). Single plate of l=h/2 at z=h/2. (Real arguments only)

The pressures over the plate are slightly higher near the wall and show a sort of parabolic behavior, increasing at the tip (without reaching those at ***x***=0). The addition of the influence of both regions shows the total horizontal distribution on the plate (Figure 4.4- right). In there, larger pressures due to higher frequencies are confirmed, and pressures tend to be 0 for areas near the tip, although it does not reach 0 at the tip as the case with the plate at the surface due to a mix of hydrodynamic phenomena in that area.

For different plate length (Plate Submersion: $\boldsymbol{h_s}$*=0. Plate length:* ***l/h****=0, 0.5, 1).*

(Only real component of the pressures)

The pressure distribution on the wall for different plate lengths (Figure 4.5 – left) exhibits that longer plates produce higher pressures but also more uniform distributions on the back wall. The pressure distribution under the plate displays that longer plates result in higher uplift pressures and more significant pressures due to higher frequencies. Furthermore, the length does not influence the tendency to 0 at the tip.

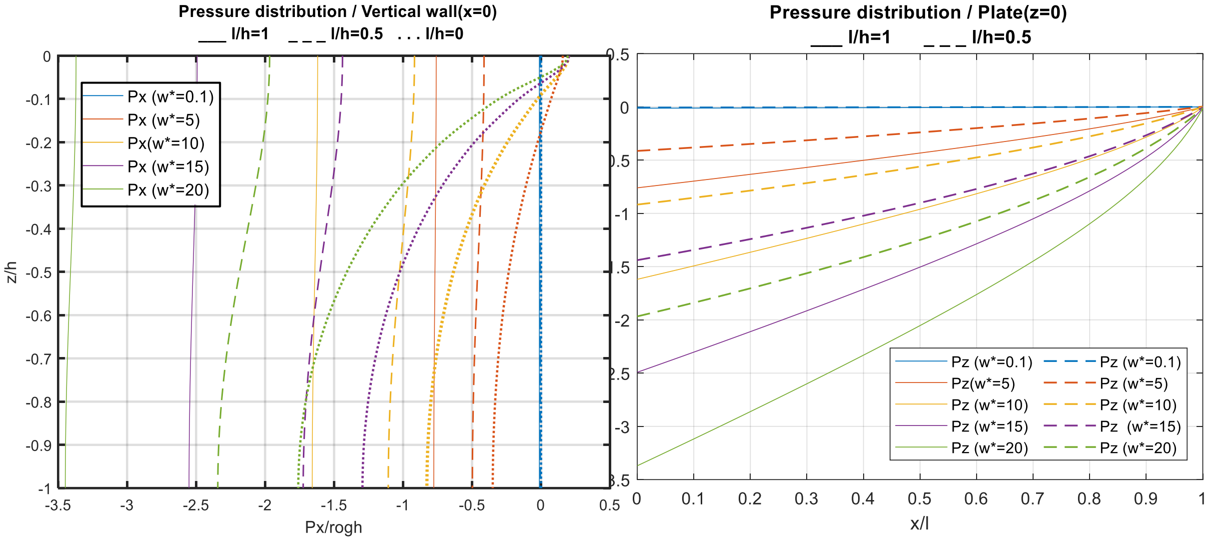

Figure 4.5. Pressure distribution acting on the wall(left) and the plate(right) for different frequencies. Single plate at z=0. (Real arguments only)

*For different submersion depth (Plate Submersion: $\boldsymbol{h_s}$=0, 0.5, 1. Plate length: **l**/**h**=0.5)*

(Only real component of the pressures)

When analyzing the pressures on the structure, it is confirmed that the plate produces higher pressures along the wall of the region under it. Still, its submersion also makes the pressure distribution uniform on the wall and less steep along the plate. Figure 4.6 (left and right) share the same legend and show only the real part of the pressure values. The negative sign in *Px* represents the direction against the movement, while $\boldsymbol{P_z}$ represents the uplift direction. Higher pressures are reached for $\boldsymbol{h_s}$ = 0 (plate at the surface), while higher pressure values correspond to higher frequencies in both cases. Maximum horizontal pressures ($\boldsymbol{P_x^{max}}$) occur at the bottom of the wall, and vertical ones ($\boldsymbol{P_z^{max}}$) at the beginning of the plate. $\boldsymbol{P_x^{max}}$ increases for a submerged plate. Additionally, $\boldsymbol{P_z^{max}}$ increases for low frequencies and decreases for higher ones Pressures at the plate tip increase due to the confluence of diverse regions flows in that zone.

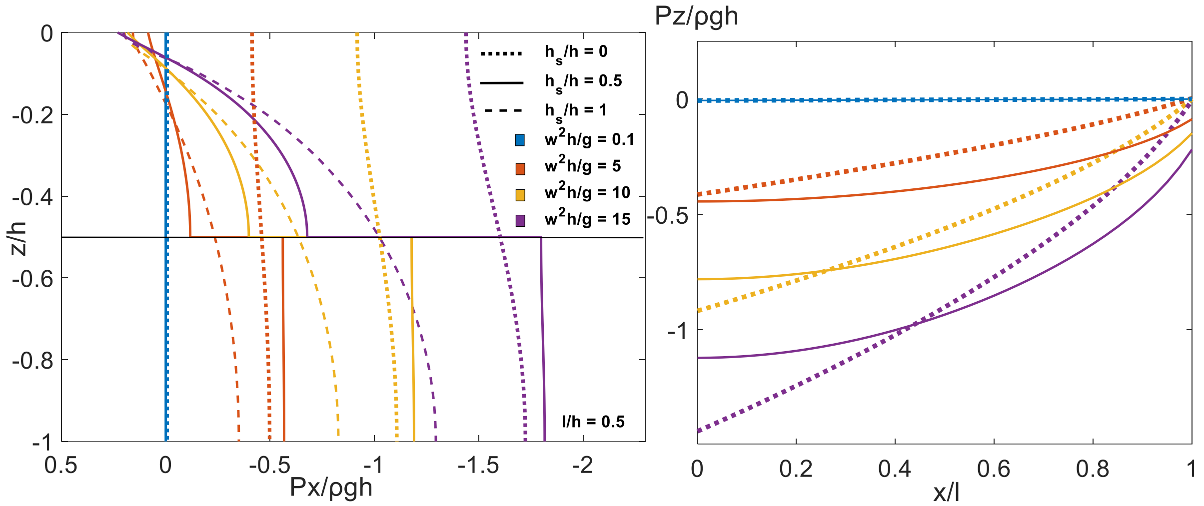

Figure 4.6. Total pressure distribution acting on the wall (left) and the plate(right) for different submersion depths and frequencies. Single plate of **l**=**h**/2 at **z**=(0, **h**/2, **h**). (Real arguments only)

4.1.2 *Hydrodynamic Parameters Analyses.*

In most cases, in order to understand the phenomena, the parameters in each region (II over the plate and III under the plate) will be analyzed, as well as their total values at the wall (with subscript $\boldsymbol{xx}$) and at the plate (with subscript $\boldsymbol{zx}$). As mentioned, the total values are the summation of the regions implied in each analysis, which translates to the expressions below.

$$M_{xx} = M_{xx}^{I} + M_{xx}^{II} + M_{xx}^{III}$$
$$M_{zx} = M_{zx}^{II} + M_{zx}^{III}$$

$$N_{xx} = N_{xx}^{I} + N_{xx}^{II} + N_{xx}^{III}$$
$$N_{zx} = N_{zx}^{II} + N_{zx}^{III}$$

4.1.2.1 Added Mass

Besides the investigation in each region, the added mass and damping coefficients study is divided into their variation according to different plate lengths and submersion depths.

For different plate lengths

[This part of the subsection is an enhanced version of a previous work of the author (Fundora, 2021) and Fundora and Aoki (2023)]

The plate length is analyzed for the plate at the surface $\boldsymbol{h_s}$= 0 and for plate lengths $\boldsymbol{l}$ = [0:0.25:1]$\boldsymbol{h}$, including the case where the cases $\boldsymbol{l}$ = 0 or $\boldsymbol{l/h}$=0 corresponds to the no-plate case.

It is evident that the added mass, both horizontal $\boldsymbol{M_{xx}}$ and vertical $\boldsymbol{M_{zx}}$, increases as the horizontal plate becomes larger, and in all cases, the behavior becomes asymptotic to a particular value (see Table 4-2). The value of $\boldsymbol{M_{zx}}$ refers to the parameter in region III, noticing that region II is eliminated from the model when the plate is at the surface, as is the case. To obtain that value of added mass when the frequency tends to be infinite, i.e., constant added mass $\boldsymbol{M}^{\infty}$ ($\boldsymbol{M}_{\boldsymbol{xx}}^{\infty}$ and

$\boldsymbol{M}_{zx}^{\infty}$); the limit of the curves' expressions is determined in the form $\boldsymbol{M}^{\infty} = \lim_{\omega\to\infty}\left(\frac{p_n\omega^{n-1}}{q_n\omega^{n-1}}\right)$. For the curve's expressions, MATLAB's fitting curve tool is used.

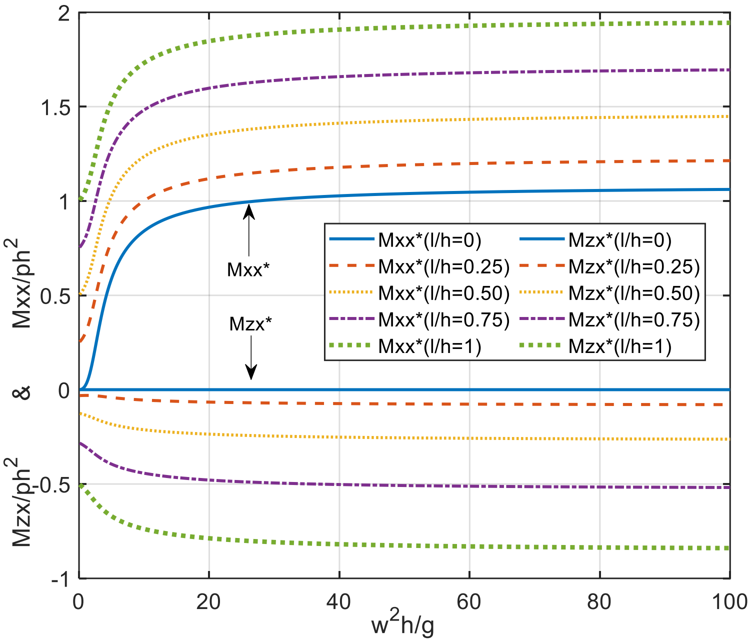

Figure 4.7. Total Dimensionless Added Mass (M_{xx} and M_{zx}).

Furthermore, Figure 4.8 displays that the horizontal $\boldsymbol{M_{xx}}^*$ and vertical $\boldsymbol{M_{zx}}^*$ added mass, as well as the ratio between them, behave relatively linearly with the variation of the plate length. However, the importance of the later $\boldsymbol{M_{zx}}^*$ over $\boldsymbol{M_{xx}}^*$ increases with plate length; thus, larger plates equalize the parameters in both directions.

Table 4-2. Dimensionless $\boldsymbol{M}_{xx}^{\infty}$ and $\boldsymbol{M}_{zx}^{\infty}$ for different ***l/h***.

l/h	$\mathbf{M_{xx}}^{\infty}$	$\mathbf{M_{zx}}^{\infty}$	$\mathbf{M_{zx}}^{\infty}$ / $\mathbf{M_{xx}}^{\infty}$
0	1.085	0	0
0.25	1.240	0.0839	0.067
0.5	1.475	0.2712	0.183
0.75	1.722	0.5311	0.308
1	1.972	0.8562	0.434

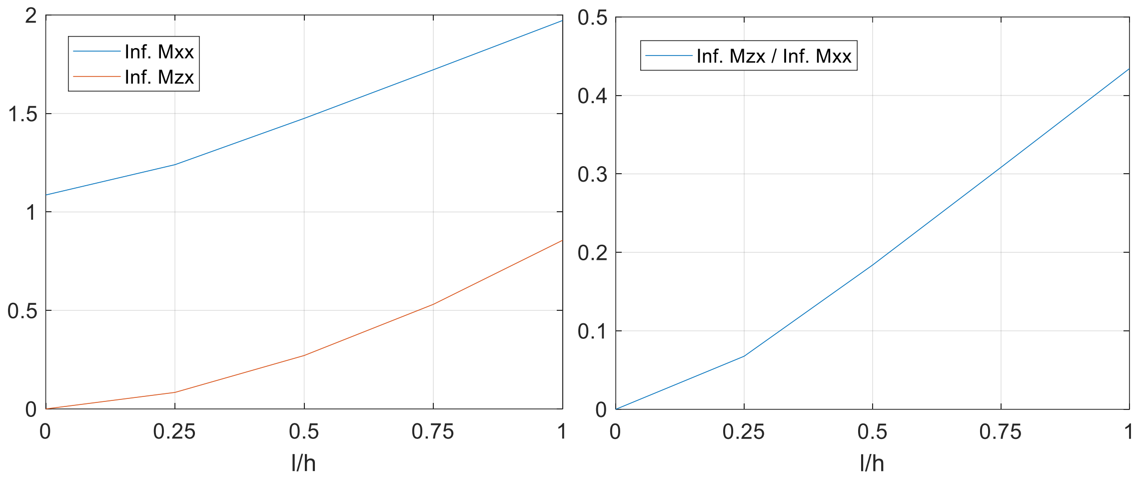

Figure 4.8. Dimensionless Constant Added Mass $\boldsymbol{M_{xx}^{\infty}}$ and $\boldsymbol{M_{zx}^{\infty}}$ (left) and ratio $\boldsymbol{M_{zx}^{\infty}/M_{xx}^{\infty}}$ (right) for different plate lengths.

For different submersion depth

The submersion depths for the analysis are $\boldsymbol{h_s}$ = [0:0.1:1]$\boldsymbol{h}$, including the cases $\boldsymbol{h_s}$ = 0.25$\boldsymbol{h}$ and 0.75$\boldsymbol{h}$, where the cases $\boldsymbol{h_s}$ = 0 and $\boldsymbol{h_s} = \boldsymbol{h}$ corresponds to the plate at the surface and no-plate case, respectively.

In Figure 4.9, the dimensionless values for the added mass acting on the wall in regions II (left figure) and III (right figure) are reflected. Figure 4.10 presents the added mass acting on the plate for the same regions. In region II, the added mass acting on the wall increases with plate submersion heading to the value of a regular caisson, although it has an initial slight reduction for plates in the range $0<\boldsymbol{h_s}\leq 0.2\boldsymbol{h}$, while the one acting on the plate increases steadily. As expected, region III's horizontal added mass decreases with the submersion of the plate and at a faster rate than the increments of region II. In contrast, the vertical added mass decreases for plates located in the range $\boldsymbol{h_s}<0.4\boldsymbol{h}$ and starts recovering for $\boldsymbol{h_s}>0.4\boldsymbol{h}$, although without reaching the initial value. This behavior responds to the larger fluid at the first locations and the narrowing depth for the latter.

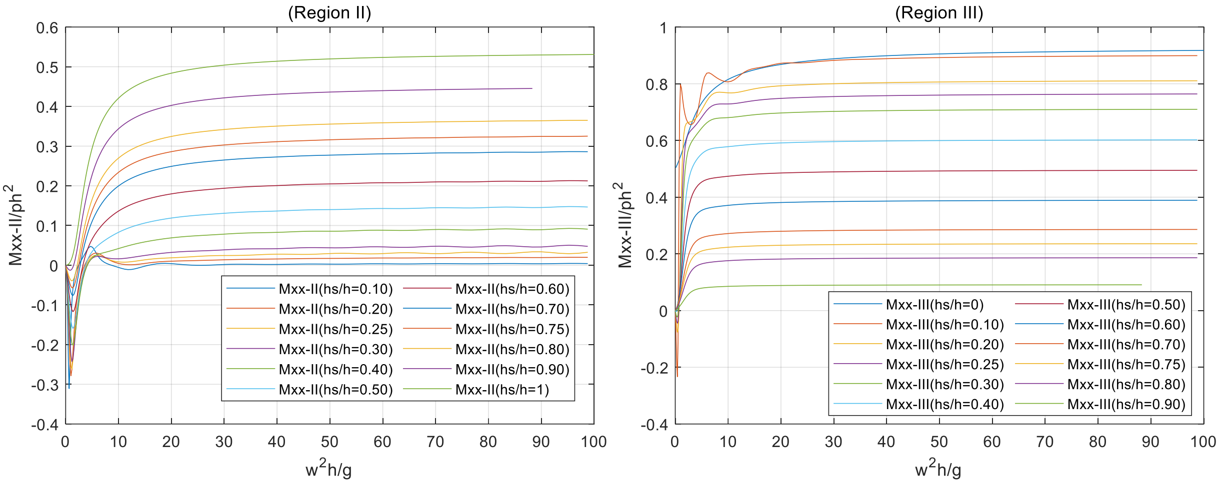

Figure 4.9. Dimensionless Added Mass on the Wall per region: over the wall -Region II (left) and under the plate -Region III (right) for different submersion depth. Single plate of *l*=*h*/2

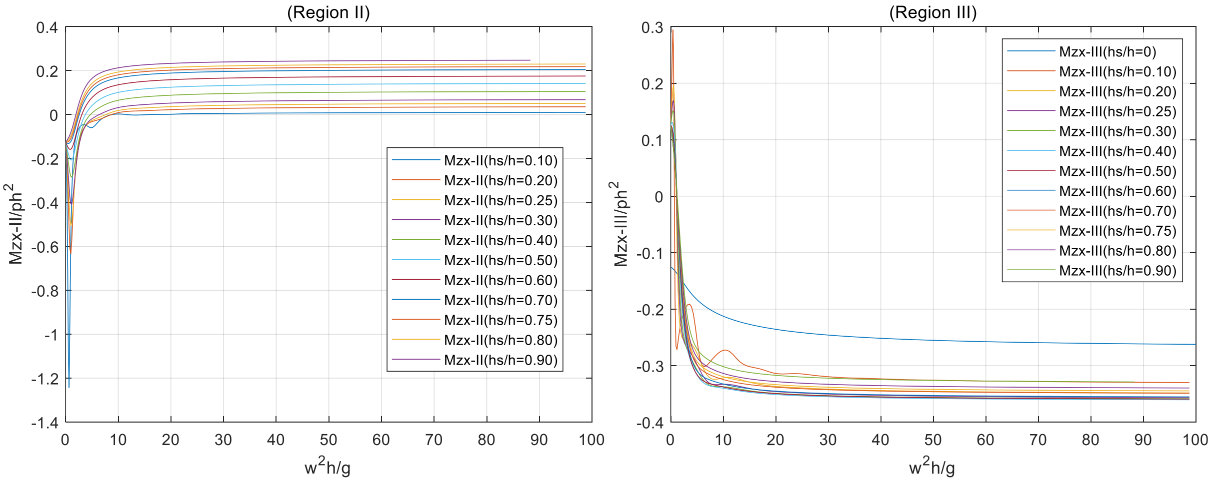

Figure 4.10. Dimensionless Added Mass on the Plate per region: over the wall -Region II (left) and under the plate -Region III (right) for different submersion depths. Single plate of *l*=*h*/2

The convolution of the related regions results in the total values for the horizontal (including region I) and vertical added mas acting on the walls and the plate are presented in Figure 4.11. From there, and the resume in

Figure 4.12, it is evident that the total horizontal added mass $\boldsymbol{M_{xx}}^*$ (left) reaches its higher value with the plate located at the surface and steadily decreases with the plate submersion since the volume of constricted fluid is reduced. The vertical added mass $\boldsymbol{M_{zx}}^*$ (right) also decreases with plate submersion; however, when comparing with the plate at the surface, the added mass of the latter has lower values than plates with $0<\boldsymbol{h_s}\leq 0.3\boldsymbol{h}$.

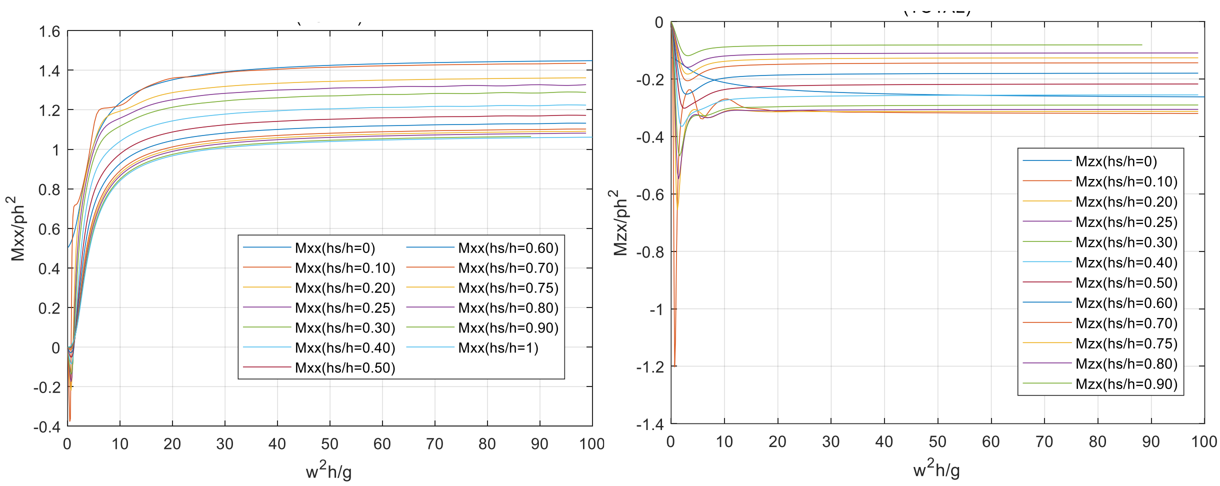

Figure 4.11. Total Dimensionless Added Mass on the Walls (left) and on the Plate (right) for different submersion depth. Single plate of ***l***=***h***/2

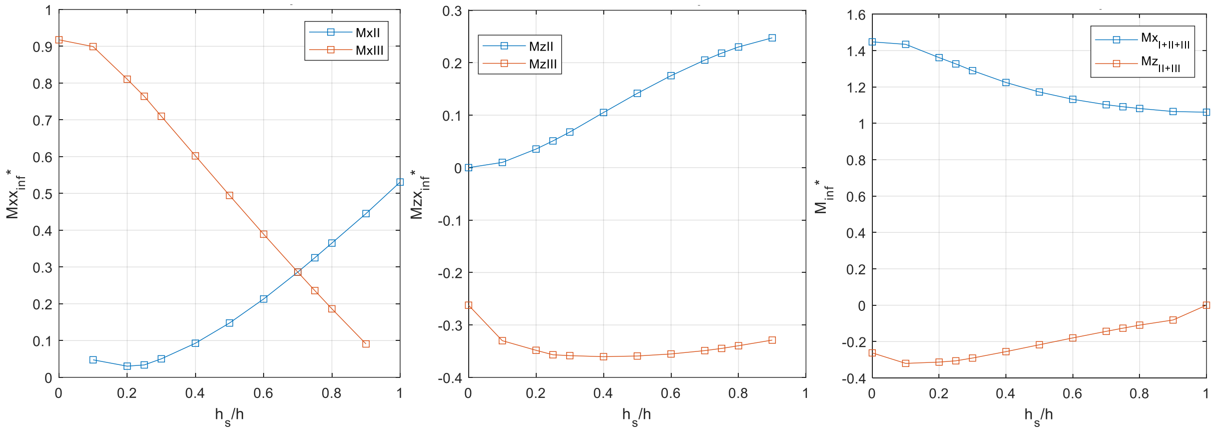

Figure 4.12. Dimensionless Constant Added Mass (ω*=100): Horizontal in regions I and II(left), Vertical in regions I and II (middle) and Total(right) for different submersion depths. Single plate of *l*=*h*/2

4.1.2.2 Damping Coefficient

For different plate lengths

The horizontal damping coefficient $\boldsymbol{N_{xx}}$ suffers minimal variations, although the cases with a plate slightly differ from the case without it. However, the vertical damping coefficient $\boldsymbol{N_{zx}}$ variation is more noticeable due to differences in the plate length. Larger plates induce higher damping. Furthermore, $\boldsymbol{N_{zx}}$ takes values closest to $\boldsymbol{N_{xx}}$ as the plate length increases. Yet, all graphs became asymptotic to 0, implying almost no influence of the damping coefficient when the frequency tends to be infinite.

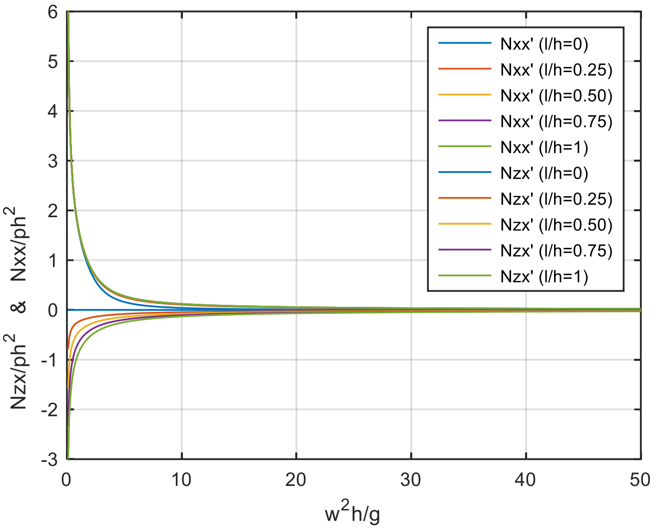

Figure 4.13. Dimensionless Damping Coefficient ($\boldsymbol{N}_{xx}{}^{*}$ and $M_{zx}{}^{*}$)

For different submersion depth

As well as with the added mass, an analysis for the influence of the submersion depth in the damping coefficient is made. In the below figures, general values for the damping coefficient are displayed on the left side, while a focus on a lower range of frequencies for each case is presented for better visualization on the right side. Horizontal damping over the plates reaches larger values and for a broader range than under the plate. Furthermore, their values are higher than those from the vertical damping. The latter in the region under the plate reaches 0 values for half of the frequency range compared to the parameter over the plate. Additionally, while submersion increases, tighter patterns show the similar behavior of plates closer to the bottom and a more noticeable variation for the plates higher than the water depth. The total values accounting for all implicated regions are seen in Figure 4.18.

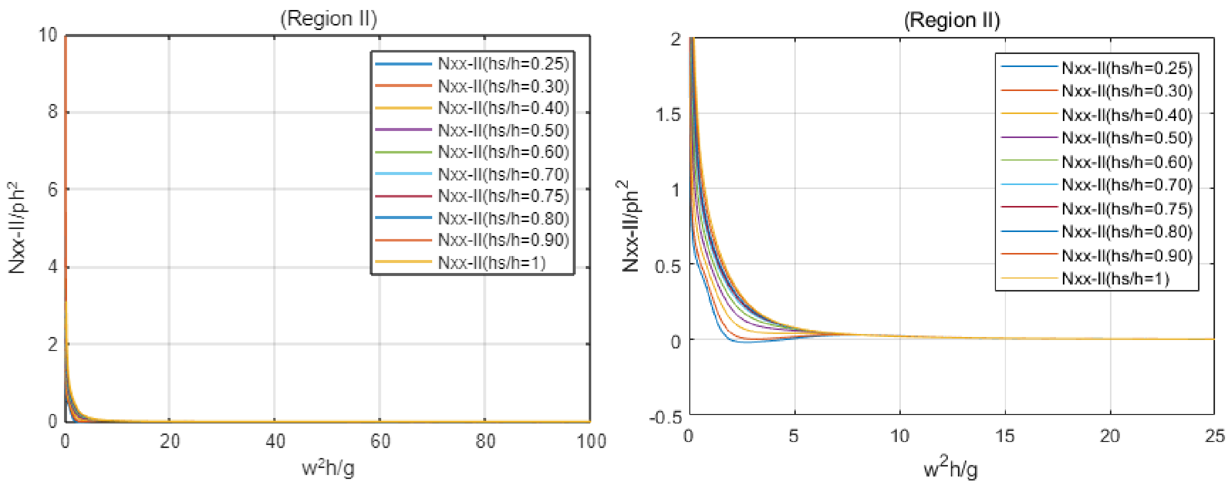

Figure 4.14. Dimensionless Damping Coefficients on the Wall over the Plate - Region II for different submersion depths. General (left) and zoomed (right). Single plate of l=h/2

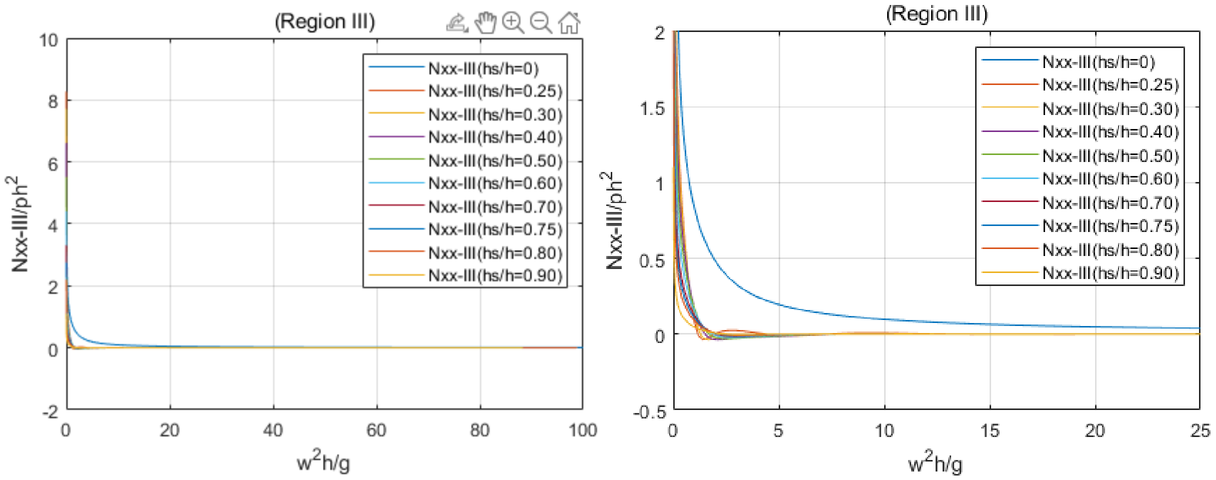

Figure 4.15. Dimensionless Damping Coefficients on the Wall under the Plate - Region III for different submersion depths. General (left) and zoomed (right). Single plate of l=h/2

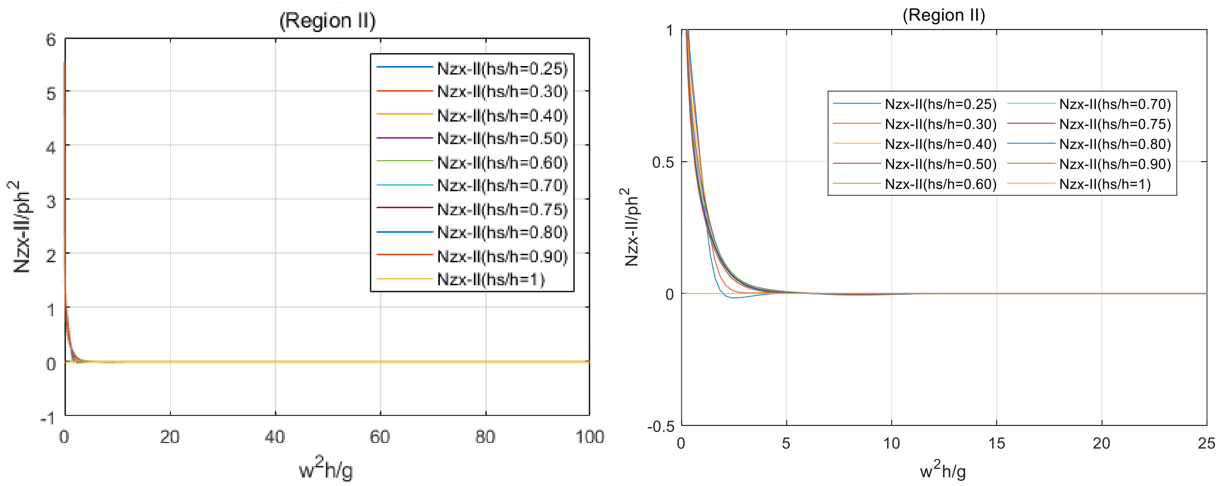

Figure 4.16. Dimensionless Damping Coefficients over the Plate - Region II for different submersion depths. General (left) and zoomed (right). Single plate of l=h/2

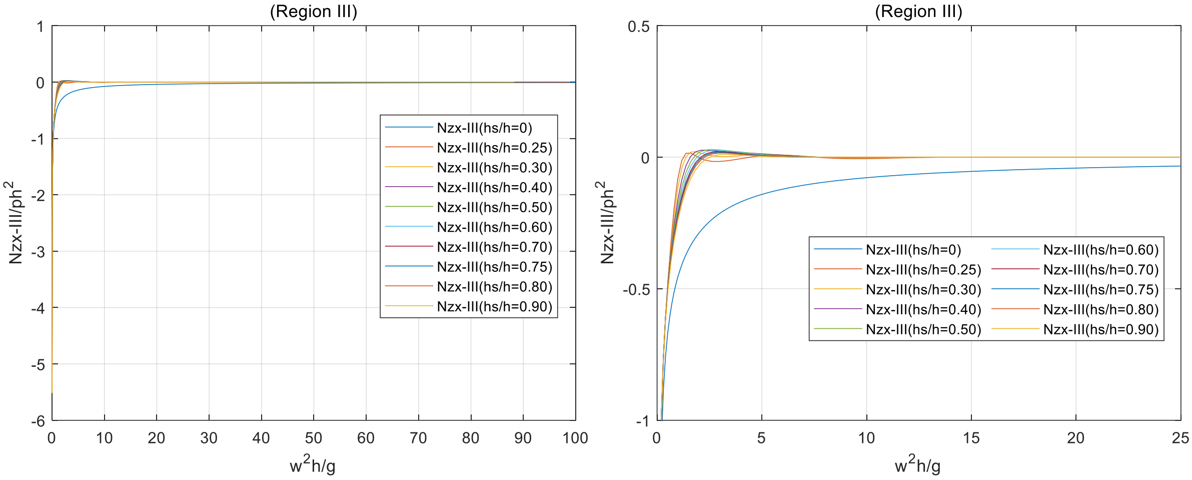

Figure 4.17. Dimensionless Damping Coefficients under the Plate - Region III for different submersion depths. General (left) and zoomed (right). Single plate of l=h/2

The total horizontal damping behaves similarly for all cases, with a more noticeable difference of the plate at the surface with higher values and more influence along the frequency range. More variations are seen for plates closer to the surface since the stability produced by the plate and volumes of fluid over it get reduced. A smaller water depth with a free surface brings variations to the parameter. Furthermore, the application of the methodology when the difference of region depths is wider also influences it. In general, as closer to the surface, the values start emulating more those from the plate at the surface.

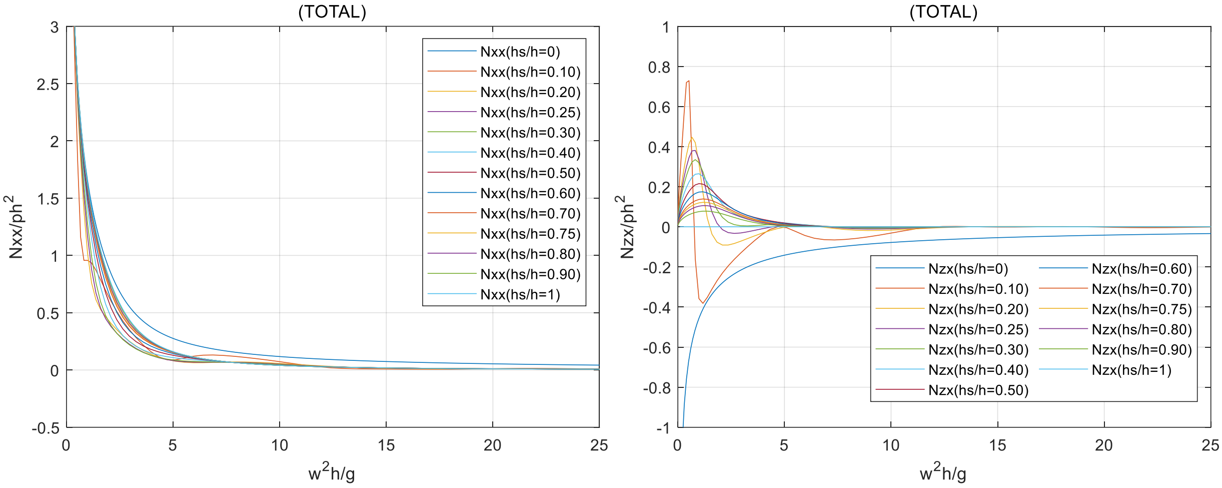

Figure 4.18. Total Dimensionless Damping Coefficients on the Wall (left) and the Plate(right) for different submersion depths. Single plate of l=h/2

4.1.2.3 *Memory- Effect Function*

The memory-effect function for different plate lengths is shown below. However, the parameter in each region is not displayed since its calculation is a function of the result of the total Damping coefficient. Hence, the submersion influence is discussed in subsection 4.1.2.4.

For different plate lengths

In Figure 4.19, a damped sinusoidal behavior for $\boldsymbol{R}^*(\boldsymbol{t}^*)$ is confirmed, with higher values in time frames near the impact of the external force. From there, it decays exponentially and then damped. Thus, the parameter is analyzed in a time frame where its influence is more significant: 0≤ **t***≤ 5.

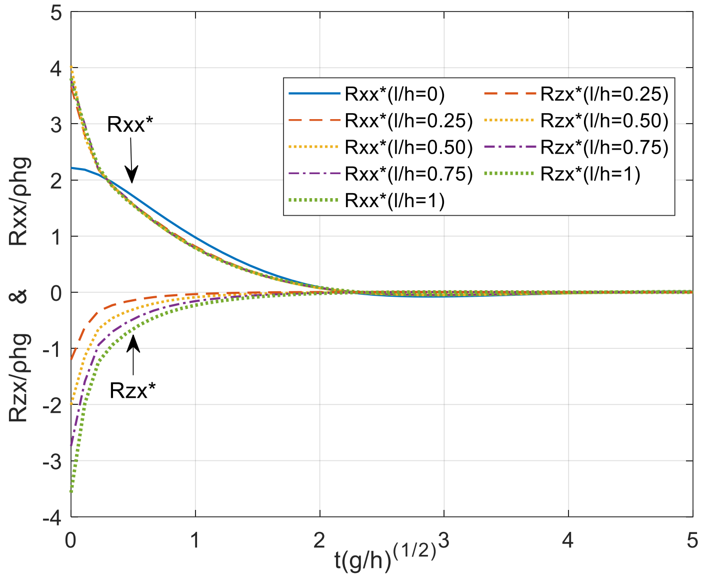

Figure 4.19. Dimensionless Memory-effect Function acting on the Wall (R_{xx}*) and the Plate(R_{zx}*) for different plate lengths. Single plate at z=0.

There is a similar overall behavior among the ***l/h*** ratios for $\boldsymbol{R}_{\boldsymbol{xx}}^*$. However, it differs from the curve of the breakwater without a horizontal plate for times near $\boldsymbol{t_o}$ with values of $\boldsymbol{R}_{\boldsymbol{0}}^*$ around 1.8 times higher than a regular caisson. The above reveals that $\boldsymbol{R_{xx}}$ function changes depending on the horizontal plate's presence. A more significant variation is observed in the Vertical Memory-effect Function $\boldsymbol{R}_{\boldsymbol{zx}}^*$. The damping tendency is still seen but with differences in the amplitude.

Unlike $\boldsymbol{R}^*_{xx}$, divergences between $\boldsymbol{R}^*_{zx}$ for different ***l/h*** ratios are seen, showing the influence of the plate variation on the $\boldsymbol{R}^*_{zx}$. Additionally, disregarding shape variations, $\boldsymbol{R}^*$ becomes 0 in the range between t^* = (2.2~2.3). As for their influence on the sliding, there is not much variation if using a linear approximation as in Aoki et al. (1995), although not the same, or a higher-degree polynomial function for $\boldsymbol{R}^*_{xx}$. Contrarily, linear approximations are impossible to use for $\boldsymbol{R}^*_{zx}$, therefore, high-degree polynomial functions are used.

4.1.2.4 *Total hydrodynamic parameters. $(M, N, R)_{xx} + f(M,N,R)_{zx}$*

For the sliding calculation, within the equation of motion, horizontal and vertical parameters are related in the form ($\boldsymbol{M}^{\infty *}_{xx} - \boldsymbol{f}\boldsymbol{M}^{\infty *}_{zx}$) and ($\boldsymbol{R}^*_{xx} - \boldsymbol{f}\boldsymbol{R}^*_{zx}$). Hence, such form will be arithmetically obtained, and the curve fitting will be done to the result of it and not to the individual parameters of $\boldsymbol{M}^{\infty *}_{xx}$, $\boldsymbol{M}^{\infty *}_{zx}$, $\boldsymbol{R}^*_{xx}$ or $\boldsymbol{R}^*_{zx}$. Note that independent memory-effect functions in each direction will not be determined since ($\boldsymbol{R}^*_{xx} - \boldsymbol{f}\boldsymbol{R}^*_{zx}$) curves are a direct function of ($\boldsymbol{N}^*_{xx} - \boldsymbol{f}\boldsymbol{N}^*_{zx}$).

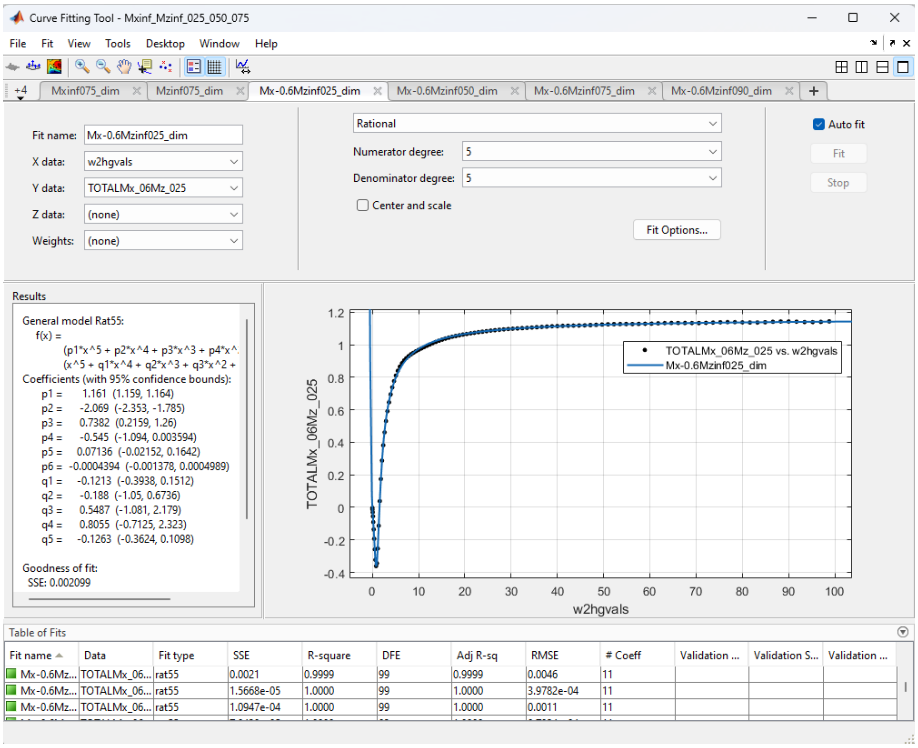

Fit name: Mx-0.6Mzinf025_dim
X data: w2hgvals
Y data: TOTALMx_06Mz_025
Z data: (none)
Weights: (none)

Rational
Numerator degree: 5
Denominator degree: 5
☐ Center and scale
☑ Auto fit

```
General model Rat55:
   f(x) = 
          (p1*x^5 + p2*x^4 + p3*x^3 + p4*x^
          (x^5 + q1*x^4 + q2*x^3 + q3*x^2 + 
Coefficients (with 95% confidence bounds):
     p1 =       1.161  (1.159, 1.164)
     p2 =      -2.069  (-2.353, -1.785)
     p3 =      0.7382  (0.2159, 1.26)
     p4 =      -0.545  (-1.094, 0.003594)
     p5 =     0.07136  (-0.02152, 0.1642)
     p6 =  -0.0004394  (-0.001378, 0.0004989)
     q1 =     -0.1213  (-0.3938, 0.1512)
     q2 =      -0.188  (-1.05, 0.6736)
     q3 =      0.5487  (-1.081, 2.179)
     q4 =      0.8055  (-0.7125, 2.323)
     q5 =     -0.1263  (-0.3624, 0.1098)

Goodness of fit:
  SSE: 0.002099
```

Fit name	Data	Fit type	SSE	R-square	DFE	Adj R-sq	RMSE	# Coeff	Validation ...	Validation S...	Validation ...
🟩 Mx-0.6Mz...	TOTALMx_06...	rat55	0.0021	0.9999	99	0.9999	0.0046	11			
🟩 Mx-0.6Mz...	TOTALMx_06...	rat55	1.5668e-05	1.0000	99	1.0000	3.9782e-04	11			
🟩 Mx-0.6Mz...	TOTALMx_06...	rat55	1.0947e-04	1.0000	99	1.0000	0.0011	11			

Figure 4.20. Screenshot of the curve fitting tool in MATLAB

Figure 4.20 shows a screenshot of the curve fitting tool in MATLAB used to determine the expressions for added mass used in the constant added mass calculations, and it is also implemented for the expressions of the damping coefficient used in the memory-effect calculation and its function expression directly used in the equation of motion to derive the sliding distance.

For the Added Mass analysis, the difference between utilizing independent parameters or the complete expressions $\boldsymbol{M}_{\boldsymbol{xx}}^{\infty} + \boldsymbol{f}\boldsymbol{M}_{\boldsymbol{zx}}^{\infty}$ is displayed in Table 4-3, where such a difference represents an error of 0.3%, which is small and admissible. What appears within the brackets represents the function to which the curve fitting is applied and the limit $\omega \rightarrow \infty$ is calculated for.

Table 4-3. Differences on calculations results using independent or complete expressions of added mass $\boldsymbol{M}_{\boldsymbol{xx}}^{\infty} + \boldsymbol{f}\boldsymbol{M}_{\boldsymbol{zx}}^{\infty}$

h_s/h	**$[M_{xx}^{\infty}]$**	**$[M_{zx}^{\infty}]$**	**$[M_{xx}^{\infty}] + f[M_{zx}^{\infty}]$**	**$[M_{xx}^{\infty} + fM_{zx}^{\infty}]$**	**Difference**	**%**
0.25	1.342	-0.3081	1.15714	1.161	0.00386	0.3325
0.5	1.188	-0.2139	1.05966	1.063	0.00334	0.3142
0.75	1.112	-0.1248	1.03712	1.04	0.00288	0.2769

For the Memory Effect function analysis, there is almost no change overall except for a difference observed for t<0.1s in the dimensional analysis. The largest difference is seen in Figure 4.21 for $\boldsymbol{h}_s/\boldsymbol{h}$=0.25, but still with a squared error of 0.998. This is an error already obtained in the $\boldsymbol{R}_{xx}$ fitting that it is dragged to the $\boldsymbol{R}_{xx}$ +$\boldsymbol{f}$ $\boldsymbol{R}_{zx}$.

The influence of using the direct output of the forms ($\boldsymbol{M}_{\boldsymbol{xx}}^{\infty *} + \boldsymbol{f}\boldsymbol{M}_{\boldsymbol{zx}}^{\infty *}$) and ($\boldsymbol{R}_{\boldsymbol{xx}}^{*}+ \boldsymbol{f}\boldsymbol{R}_{\boldsymbol{zx}}^{*}$) reduce errors introduced on the multiple approximations and calculations for each independent parameter, simplify the procedure within the methodology, and consequently decrease the analysis time. Furthermore, after checking the use of reduced and general equations for $\boldsymbol{R}(\boldsymbol{t})$, the changes were minimal. This is related to the fact that the displacement time is short, so the part of the graph that passes the 0 axis is not used, and that part is well-fitted on the general curve. However, to be more accurate, we will continue using the fitting curve to the $\boldsymbol{R}(\boldsymbol{t} = 0\text{-}5\text{s})$.

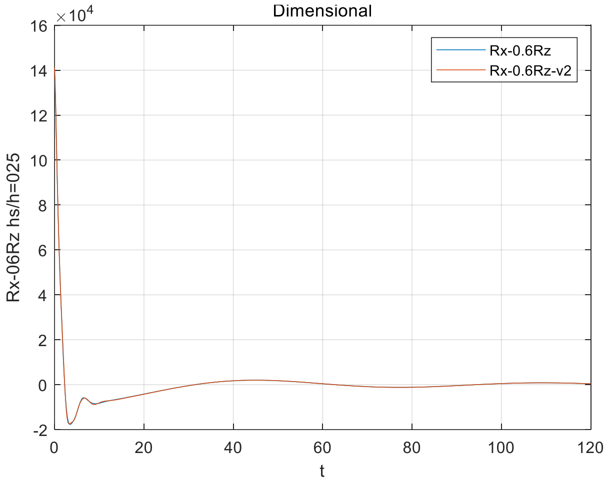

Figure 4.21. Results of the curve fitting using independent or complete expressions of memory-effect functions $\boldsymbol{R}_{\boldsymbol{xx}}^{\infty} + \boldsymbol{f}\boldsymbol{R}_{\boldsymbol{zx}}^{\infty}$

Added Mass M_{xx} - f M_{zx}

Plates located at $\boldsymbol{h_s}/\boldsymbol{h}$<0.4 have larger Added Mass relationships than a caisson without plate. According to this parameter, those cases are initially expected to behave better, while it might be unreasonable to locate plates at lower locations since performance will be poorer than the regular case (no plate). The case $\boldsymbol{h_s}/\boldsymbol{h}$ = 0 (plate at the surface) still has a larger Added Mass, and it is expected to behave better than all cases. The Constant Added Mass derived from the curves is also displayed in Figure 4.22(right).

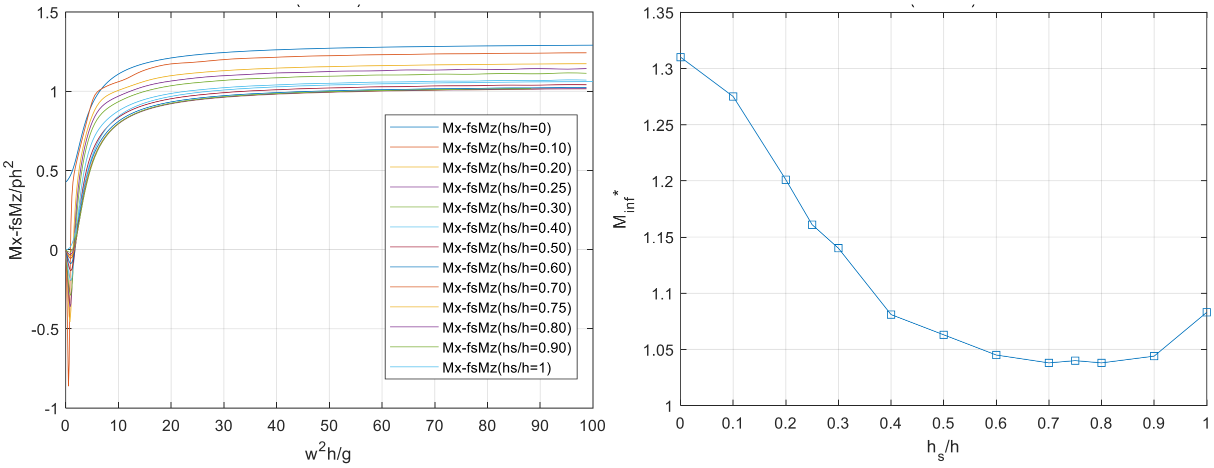

Figure 4.22. Relationship $M_{xx}^{\infty *} + f M_{zx}^{\infty *}$ (left) and Dimensionless Constant Added Mass (right) for different submersion depths. Single plate of *l*=*h*/2.

Memory-effect function R_{xx} - f R_{zx}:

As mentioned before, the Memory-effect function in the time domain is based on the damping coefficient in the frequency domain. Thus, the dimensionless relation N_{xx} - f N_{zx} is displayed in Figure 4.23(left), while the output for the memory-effect function is provided on the right side of the figure. The memory-effect functions for submerged plates follow a similar tendency: maximum at t*=0 with a fast damp reaching 0 in a range between t*=[1.91~2.95]. The effective time for the damping primarily decreases with plate submersion, with higher effective time for $\boldsymbol{h_s}$ =0.1$\boldsymbol{h}$ and shorter times for regular caissons and out of the pattern $\boldsymbol{h_s}$=0. The dimensionless memory effect function's maximum (R_0^*) and its integral are shown in Figure 4.24.

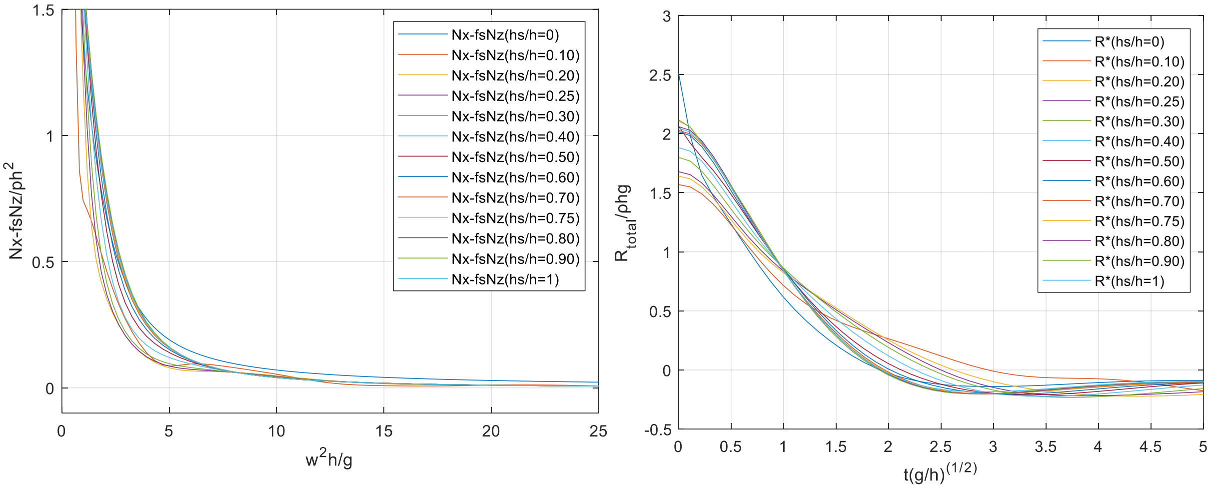

Figure 4.23. Horizontal and Vertical relationship for Dimensionless Damping Coefficients N_{xx} - f N_{zx} (left) and Dimensionless Memory-effect Function R_{xx} - fR_{zx} (right). Single plate of l=h/2

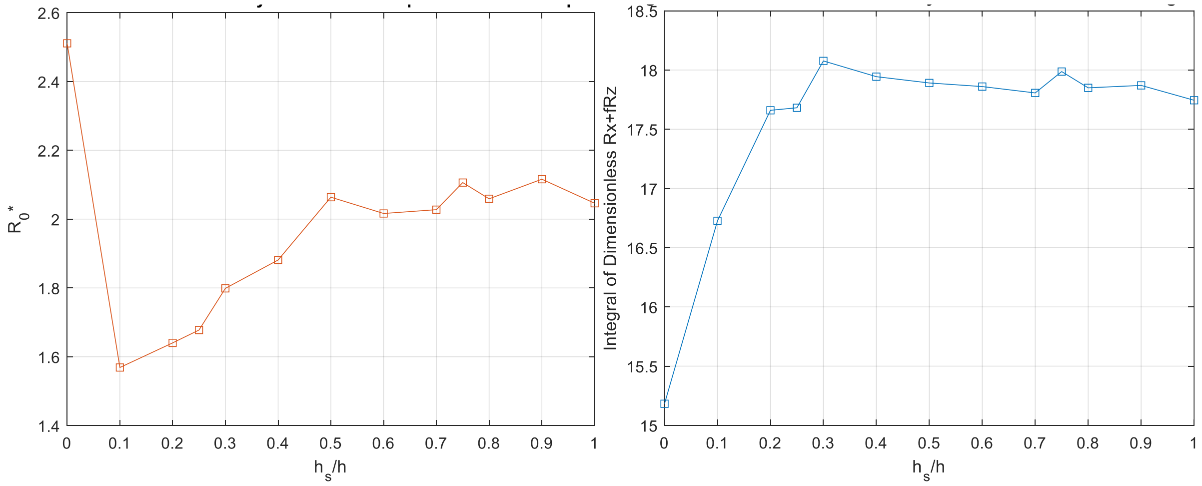

Figure 4.24. Dimensionless Memory-effect Function (left) and Integral of the Dimensionless Memory-effect Function (right). Single plate of l=h/2.

Furthermore, their ratio with respect to the values for the no-plate case, including the constant added mass from a previous analysis, is gathered in Figure 4.25 for better visualization. Based on the above figure, and when comparing with the regular caisson, larger added masses are obtained for submersion depth $\boldsymbol{h_s} < 0.4\boldsymbol{h}$. The behavior is to decrease with submersion and slightly recover after $\boldsymbol{h_s} > 0.75\boldsymbol{h}$. The memory-effect functions have lower integral values (component used within the motion equation) for $\boldsymbol{h_s} \leq 0.25\boldsymbol{h}$, while similar values to the no-plate case are seen for $\boldsymbol{h_s} > 0.2\boldsymbol{h}$, although slightly higher for $\boldsymbol{h_s} > 0.25\boldsymbol{h}$. The behavior is to have a minimum value for the plate at the surface, increasing up to around $\boldsymbol{h_s} = 0.2$, $0.25\boldsymbol{h}$ and remaining stable.

On the other hand, a quick look at the dimensionless memory-effect function's maximum (R_0^*) shows a reduction tendency when decreasing the submersion depth, with similar ratios than the regular caisson for the submersions under half of the water depth, but a sudden increment for the plate at the surface. A general reading is that regarding the added mass and the memory-effect function, while one increases, the other decreases, and vice versa; thus, their effect might get outweighed. The only case where this doesn't happen is at the surface. This is expected to be reflected in the output of sliding calculations. slightly higher values are at $\boldsymbol{h_s} \geq 0.75\boldsymbol{h}$; those locate at $0.1\boldsymbol{h} \geq \boldsymbol{h_s} > 0.5\boldsymbol{h}$ have lower values.

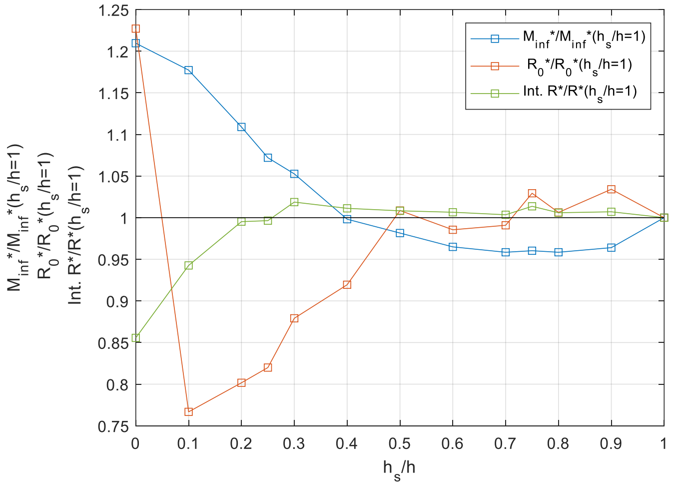

Figure 4.25. Ratio of Dimensionless Constant Added Mass and Memory-effect Function parameters related to the No-plate case for different submersion depths. Single plate of *l*=*h*/2.

4.1.3 *Sliding*

The process to determine the sliding of a breakwater with a horizontal plate is described in section 2.3.10 of Chapter 3. Sliding depends on the Wave Force *F(t),* the Frictional Force F_f, the Added Mass at infinite frequency (M^∞), and the Memory-effect Function *R.*

The mentioned procedure adapts and modifies the method introduced by Aoki et al. (1995) in "Simulation of the sliding of the breakwaters upright part" (in Japanese). The model includes vertical hydrodynamic forces (see Eq.2.102) and utilizes eight and nine-degree polynomial functions to describe the Memory-effect Function *R* instead of the linear approximation.

$$(m_a + M_{xx}^{\infty} + f_s M_{zx}^{\infty})\ddot{x} + \int_0^t [R_{xx}(t-\tau) + f_s R_{zx}(t-\tau)]\dot{x}(\tau)d\tau = \begin{Bmatrix} \alpha f_s m_w g \dfrac{t}{t_p}; & (0 \le t \le t_p) \\ \alpha f_s m_w g_s \left(2 - \dfrac{t}{t_p}\right); \ t_p \le t & \end{Bmatrix} \quad \text{Ref. to (3.126)}$$

For generalization, Eq.(3.126) is dimensionless expressed as in Eq.(4.1)

$$({m_a}^* + {M_{xx}^{\infty}}^* + f_s {M_{zx}^{\infty}}^*)\ddot{x}^* + \int_0^{t^*} [{R_{xx}}^*(t^* - \tau^*) + f_s {R_{zx}}^*(t^* - \tau^*)]\, \dot{x}^*(\tau^*)d\tau^*$$

$$= \begin{Bmatrix} \alpha f_s({m_w}^* g)\dfrac{t^*}{{t_p}^*} & (0 \le t^* \le {t_p}^*) \\ \alpha f_s({m_w}^* g)\left(2 - \dfrac{t^*}{{t_p}^*}\right) & ({t_p}^* < t^*) \end{Bmatrix} \tag{4.1}$$

4.1.3.1 Sliding reproducibility

Sliding due to the implementation of equations Eq.(4.1) to the model introduced in section 4.1 is compared with the sliding obtained by the method used in Aoki et al. (1995). The same parameters were used. Furthermore, an 8-degree polynomial is employed as Memory-Effect Function in the BPS case instead of the linear approximation in the conventional case. Fig.3-12 displays such a comparison.

Variation is minor, in the order of 3E-04 for general sliding and 0.000566m ≈ 0.6mm for the value of maximum sliding, implying a good agreement and confirming the reproducibility of both displacement and velocity. Furthermore, it is irrelevant for regular caisson (without horizontal plate) if the exact expression of the Memory-Effect Function is used as a high-order polynomial function or a linear approximation. However, this is not the case when determining the vertical component, as it was introduced in section 3.5; thus, the high-order polynomial functions will be used in all cases.

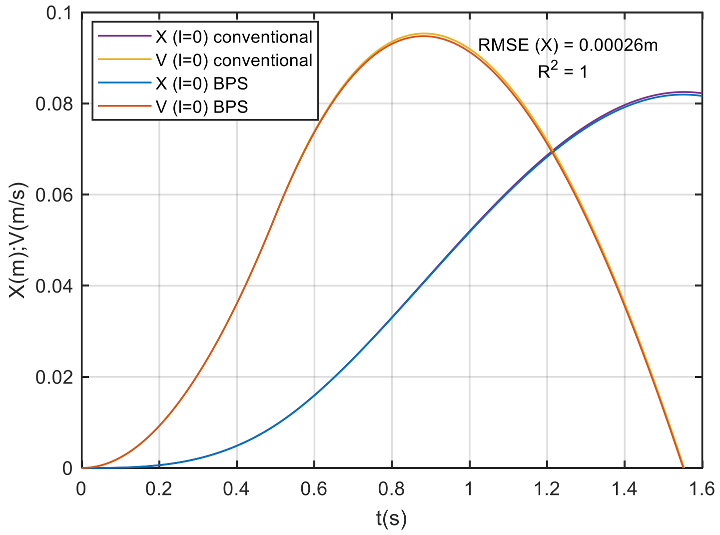

Figure 4.26. Displacement and Velocity for Breakwater Without Horizontal Plate (l/h = 0) Conventional Method v/s Boundary-Point Selection Method (BPS) (f_s=0.6, α=0.1, t_p=0.5).

4.1.3.2 *For different plate lengths*

[This part of the subsection is an enhanced version of a previous work of the author (Fundora, 2021) and Fundora and Aoki (2023)]

In this subsection, the horizontal plate influence is analyzed by changing the ratio of plate length to water depth (***l/h***). Such analysis is made for the relations ***l/h*** = 0, 0.25, 0.5, 0.75, and 1.0. The case ***l/h***=0 corresponds to the regular caisson (without horizontal plate). Although in Figure 4.27, a dimensional displacement is shown for the model (***B***=10m, ***h***=8m, ***d***=2m) with the parameters expressed in the figure's caption, when comparing with other models in further subsections, the analysis will be made for dimensionless parameters.

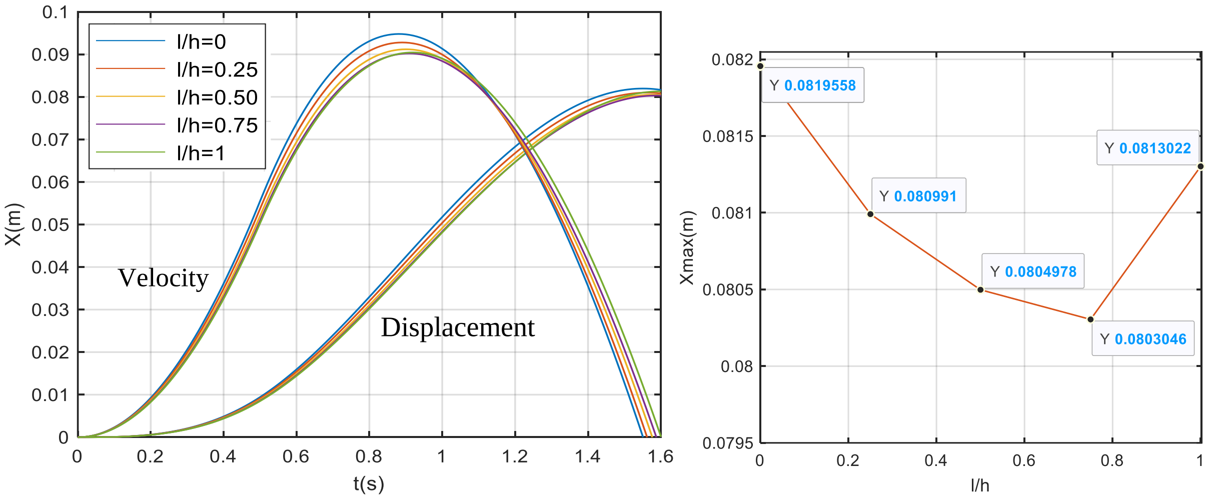

Figure 4.27. Displacement and Velocity (left) and Maximum Displacement for (right) for *l*/*h* = 0:0.25:1 (f_s=0.6, α=0.1, t_p=0.5).

For all ***l/h*** *>0*, the maximum displacement is inferior to the case without a plate ***l/h*** *=0*. Hence, it is correct to say that adding a horizontal plate reduces the caisson sliding. Furthermore, the behavior of the maximum sliding is to steadily decrease with increments of the plate length up to ***l***=0.75***h***, to increase after, although not reaching the sliding of the no-plate case. Thus, when the plate becomes too long, reaching ***l***=***h***, it starts working as an equalizer of the forces acting on the wall and the plate, as we saw in the independent analysis of the force components; thus, the sliding goes back to be similar that from the regular caisson.

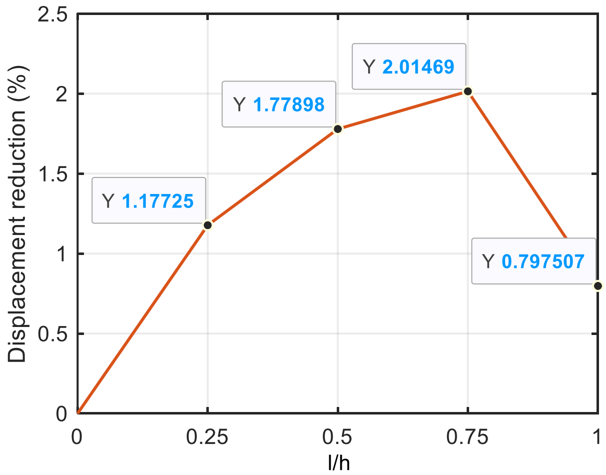

Figure 4.28. Displacement reduction for *l*/*h* = 0:0.25:1

Finally, the influence of the horizontal plate at the surface on the reduction of the caisson sliding against impulsive waves is minimal, with a maximum of 2% for ***l/h*** =0.75, as displayed in Figure 4.28, where the displacement reduction with respect to the regular caisson is presented.

4.1.3.3 For different submersion depth

In this subsection, the influence of the horizontal plate submersion on the sliding is analyzed by changing the ratio of the plate submersion depth to the water depth (***h_s/h***). Such analysis is made for the relations ***h_s/h*** = 0:0.1:1, including ***h_s/h***=0.25 and 0.75. The case ***h_s/h*** = 0 corresponds to the plate at the surface and ***h_s/h*** = 1 to the regular caisson (without horizontal plate). From the plate length analysis, a plate with length *l*=*h*/2 is selected and utilized for the submersion analysis.

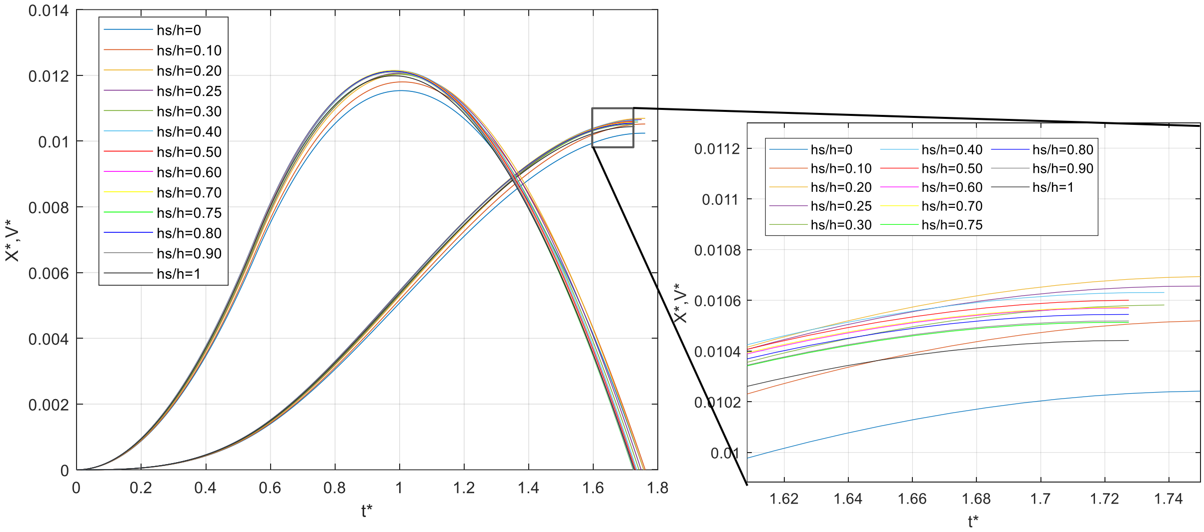

Figure 4.29. Dimensionless Sliding/Displacement for different submersion depth. Single plate of *l*=*h*/2

The minimum sliding is reached by a plate at the surface, starting to increase, reaching a maximum sliding at ***h_s***= 0.2***h***. From there, the sliding distance starts decreasing until reaching the displacement for a case without plate. The reason for this is that for the first part of the behavior, the fluid area gets reduced and so does their positive influence on reducing the sliding;

while for the second half, the combination effect of the fluid mass over the plate and the total added mass, counteract the uplift forces, thus the sliding reduces. Among the submerged locations, the displacement is slightly smaller while the plate is closest to the surface $\boldsymbol{h_s} \leq 0.1\boldsymbol{h}$ or to the bottom $\boldsymbol{h_s} \leq 0.75\boldsymbol{h}$ around. Nevertheless, only the plate at the surface or very close to it (less than 0.1h) reduces the sliding when compared with the regular caisson.

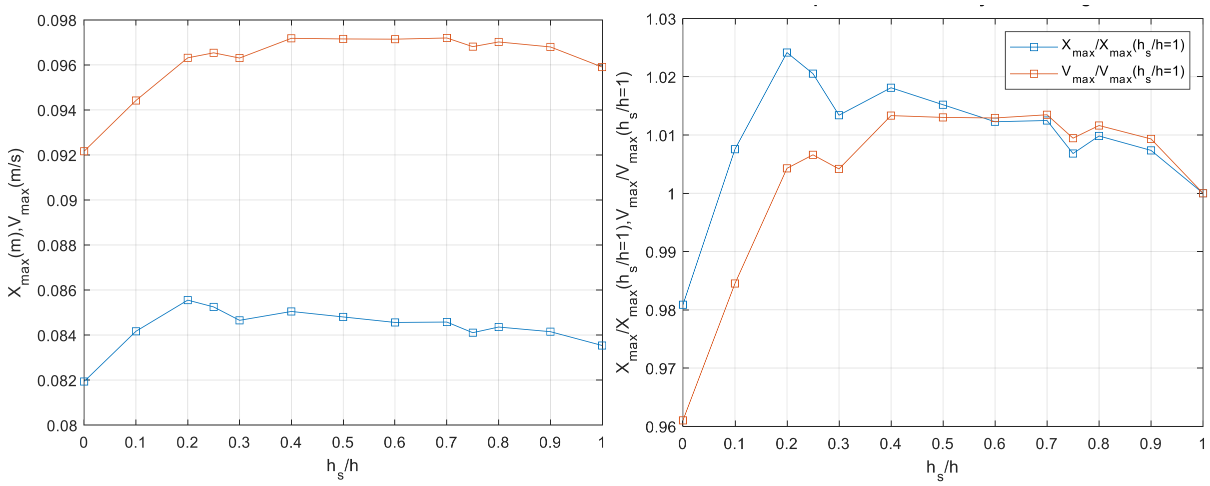

Figure 4.30. Dimensional maximum sliding and velocity (left) and ratio related to the no-plate case for different submersion depths. Single plate of $l=h/2$

Regarding motion velocity, the caisson velocity is minimum for the plate at the surface, doubling the sliding reduction rate with respect to the no-plate case. It sharply increases and remains constant from $0.4 \leq \boldsymbol{h_s}/\boldsymbol{h} \leq 0.7$ when it starts decreasing again until reaching the no-plate case. Furthermore, for both sliding and velocity, plate locations at distances $\boldsymbol{h}/3$ from the surface and the bottom drop with respect to their relative tendencies. This might respond that the positive effect on the sliding of the forces acting over and under the plate is more balanced at such locations.

4.1.3.4 *Influence of the use of vertical components on the sliding*

Although in Figure 4.27, a dimensional displacement is shown for the model (**B**=10m, **h**=8m, **d**=2m) with the parameters expressed in the figure's caption, the comparison analysis is made for dimensionless parameters. From Figure 4.31, the sliding due to both cases (with and without vertical force) can be contrasted.

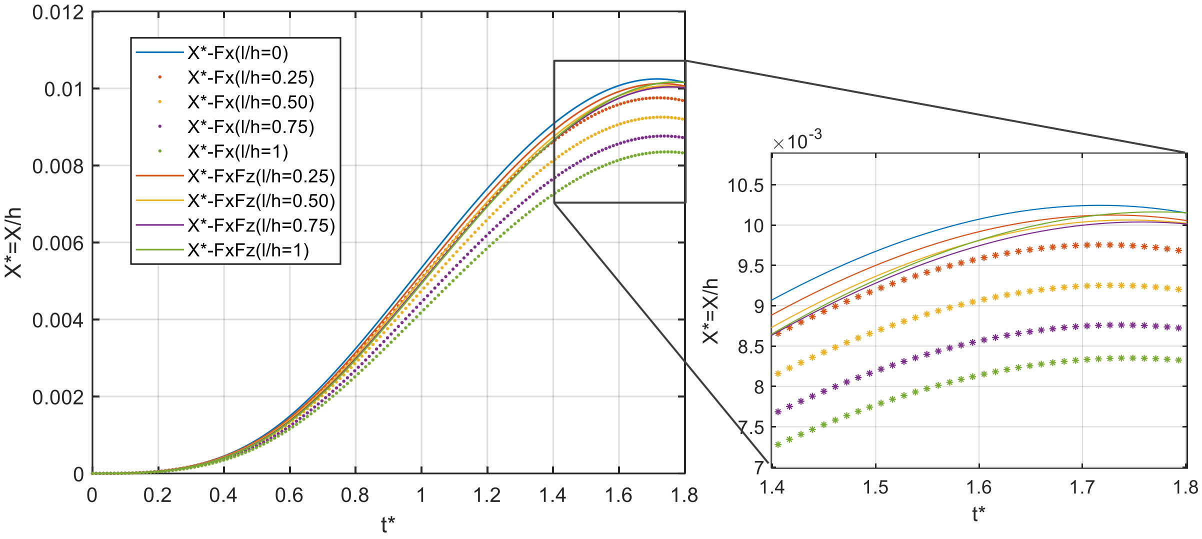

Figure 4.31. Dimensionless displacement for the "only Fx" and "FxFz" cases.

Compared with the only use of the horizontal forces "only F_x" {using Eq.(4.1) with only $\boldsymbol{M_{xx}}$ and $\boldsymbol{R_{xx}}$ i.e., dismissing $\boldsymbol{M_{zx}}$ and $\boldsymbol{R_{zx}}$} and as in the conventional approach and in (Yoshihara, 2019), where such reduction in the sliding is crescendo for larger relation ***l/h*** until reaching almost 20%, the inclusion of the vertical force in the analysis gives more accurate results due to a broader representation of the phenomena. Excluding $\boldsymbol{M_{zx}}$ and $\boldsymbol{R_{zx}}$ leads to underestimating the sliding of the caisson and overestimating the horizontal plate's positive influence in reducing the sliding, especially for larger ***l/h*** ratios.

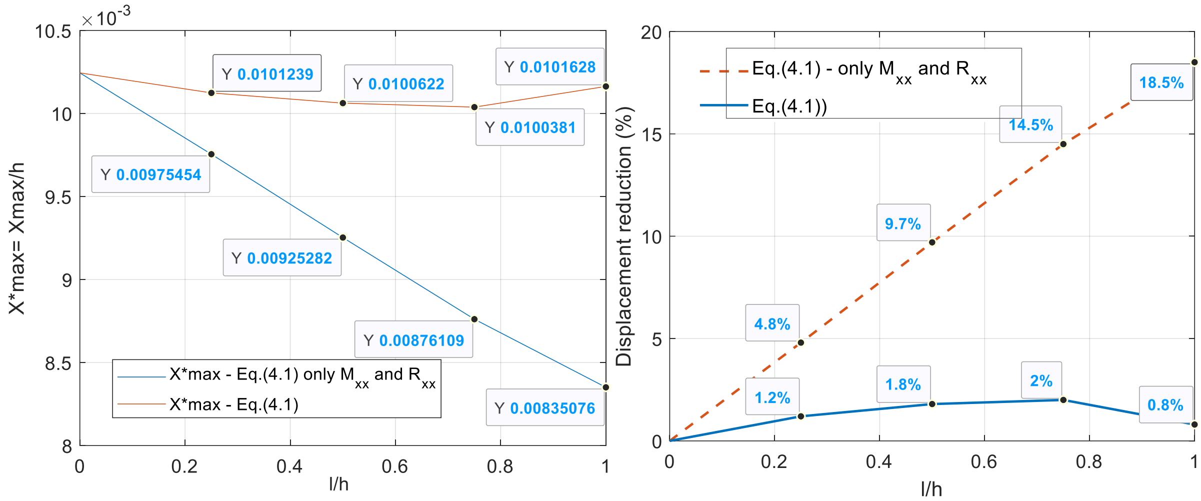

Figure 4.32. Dimensionless maximum displacement (left) and displacement reduction (right) for the "only Fx" and "FxFz" cases.

Compared with the "only F_x" case, sliding becomes around 4%, 8%, 12% and 18% smaller for ***l/h***=0.25, 0.50, 0.75 and 1, respectively. Finally, the real influence of the horizontal plate on the sliding of the breakwater caisson is minimal, with a maximum of 2%, as in Figure 4.32 (right). Hence, the conventional model dismissing vertical components of the forces in the sliding simulation is not applicable to caissons with horizontal plates.

4.1.3.5 Influence of the use of the memory-effect function on the sliding

The introduction of the memory-effect function in the sliding simulation is another difference from the conventional model for regular caissons. Thus, it is also analyzed in addition to the vertical components of the forces. In the figure below, the comparison of the results of the caisson's motion equation as in the conventional model, utilizing only the added mass (real component of the forces), and as in the proposed model, utilizing both the added mass and the memory-effect function (imaginary component of the force expressed in time domain).

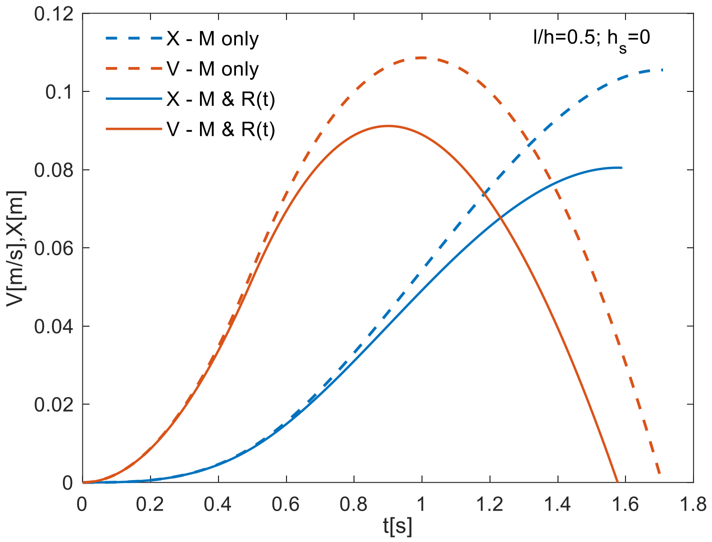

Figure 4.33. Influence of the inclusion of memory effect function on the sliding and velocity.

As displayed in the figure, there is a significant variation of the sliding maximum distance, velocity, and effective time of the sliding. For the first part of the movement, there is not much variation. Such time is slightly higher than the rising time of the wave force (t_p=0.5s in this case). The memory-effect function should be included in the sliding simulation of caisson with plates. Neglecting it overestimates the sliding by about 30%. Hence, the generalized model does not apply to it.

4.1.3.6 Influence of the Wave Parameters: Rising Time and Force Magnitude

The parameters of the wave force used in the simulation also have an important influence in the sliding simulation. For the case of impulsive waves, the representative parameters are the rising time and the force magnitude. The rising time is the time lapse from when the sliding starts i.e., when the wave force is higher than the static frictional force F_s (force needed to produce sliding), until the maximum wave force is reached. The force magnitude is the normalized relation of maximum wave force F_{max} and the static frictional force F_s as below.

$$\alpha = (F_{max} - F_s)/ F_s \tag{4.2}$$

Larger rising times of the impulsive wave t_p lead to smaller initial sliding but larger total sliding.

It translates into faster initial motions before reaching maximum velocity; after that, deceleration occurs at the same pace for all t_p. Increasing rising times also increases the maximum velocity reached during the sliding; however, the sliding velocity itself (ratio of maximum sliding to maximum velocity) gets reduced. The sliding duration increases with increments of the rising time.

On the other hand, higher force magnitude α directly translates to larger initial and total sliding. The relative increments of the sliding remain similar for all cases. Furthermore, increasing α also increases the maximum velocity reached during the sliding; however, α changes do not influence the sliding velocity or duration.

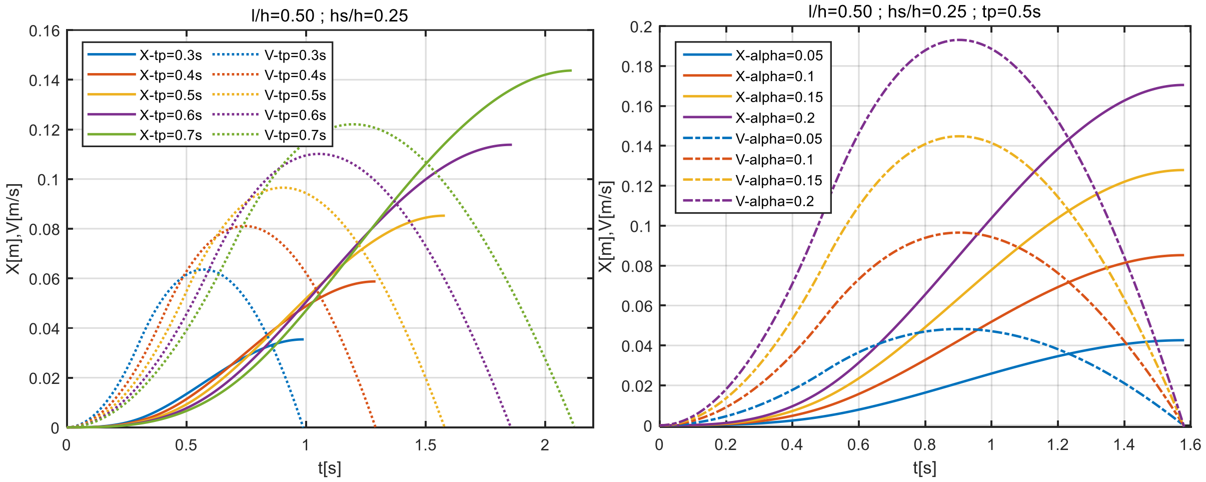

Figure 4.34. Displacement and Velocity for wave rising time (left) and alpha (right) variation.

4.1.4 *Conclusions for the single plate case*

The analysis results confirmed that the presence of a single plate increases the added mass of the structure. When focusing on plate length, general added mass can grow up to 35% for plates at the surface with lengths up to water depth value h. In contrast, the general added mass starts decreasing with plate submersion, adversely influencing the sliding for submersion depths higher than 0.4h. On the other hand, the damping effect has a more significant influence on the sliding of plates located at submersion depths over 0.4h, with positive influences for the superficial plates but also over depths higher than $0.75\boldsymbol{h}$ and negative influences on the range $0.1\boldsymbol{h} \leq \boldsymbol{h_s} < 0.5\boldsymbol{h}$. An increase in the horizontal added mass as the plate becomes larger is corroborated, but it is also seen in the vertical added mass. Other parameters, such as damping coefficients, do not see much change in the horizontal direction, but they do in the vertical one. Such relations indicate that the longer the plate, the more equal the parameters at the vertical wall and the horizontal plate. Thus, the plate works as an equalizer for horizontal and vertical directions, which is reflected in the sliding calculations.

The combined effect of the hydrodynamic parameters results in a reduction of the sliding for plates located at the surface, with a better impact for plate lengths between 50% and 75% of the water depth value. The positive effect of the hydrodynamic coefficients’ horizontal components on the sliding was drastically reduced by the vertical ones when such plates have lengths larger than 2/3 of the water depth.

Regarding the sliding simulation, the critical influence of uplift forces and the importance of including the memory-effect function when elements such as plates are added to the caisson are corroborated. An underestimation of the sliding is obtained when dismissing the forces' vertical parameters; such underestimation increases with plate length reaching up to 20% for plate lengths equal to water depth. On the other hand, dismissing the memory-effect function leads to overestimating the maximum sliding of around 30%.

4.2 CAISSON WITH TWIN HORIZONTAL PLATES. COMPARISON

The initial hypothesis of the influence of the water constriction in the increment of hydrodynamic coefficients, such as the added mass, was displayed in the previous section. However, it was also observed that another parameter, the damping coefficient, reduces the general positive effect on the sliding of the caisson. To investigate further, a twin plate arrangement is analyzed in the present section of the document, and a comparison with the single plate at the surface is made.

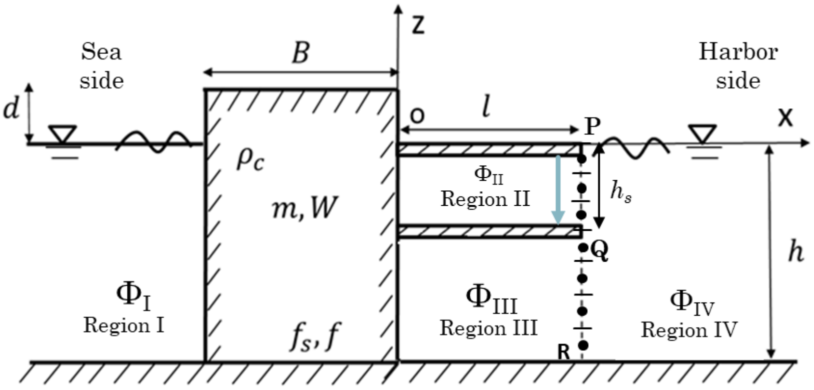

Figure 4.35. Model representation of a caisson with twin plates.

As Figure 4.35 shows, the model is similar to the one presented in section 4.1 but with a combination of a caisson with a submerged plate and another one at the surface. The latter was the best location from the single plate analysis; thus, the arrangement for the twin plates keeps one plate at the water surface and the second one is submerged at ½ of the water depth. Although different submersion depths can be analyzed using the present methodology, a single location is enough to validate the hypothesis for this section. Geometric characteristics of the caisson, water depth and properties of the medium remain as in section 4.1.

4.2.1 *Pressure analysis.*

After finding the solution for the velocity potential, the first parameter to be obtained is the pressure, which is an excellent indicator for visualizing the effect of the plates on the reactions at the wall and plates. The values of pressures are complex numbers: the real part is related to the propagating mode (connected to the added mass obtention), and the imaginary part to the evanescent or decaying mode (connected to the damping coefficient). Selected values within the frequency range: $\boldsymbol{\omega}^*$ = 0.01, 1, 10, 100, for better visualization and analysis. The primary and extended approach when analyzing pressures, and consequently the forces, is made based on the real part of the complex argument. Figure 4.36 displays such components of the pressures at the wall (left) and the plates (right) for regions II and III, or 2 and 3, respectively.

The pressure acting on the vertical wall has less variation in Region II (Px2) than in Region III (Px3), reaching the maximum values near the plate for both regions. In contrast, the pressure acting on the plates decreases as the distance from the wall to the analyzed point $\boldsymbol{x}$ increases, being larger near the wall and nearly half at the end of the plate.

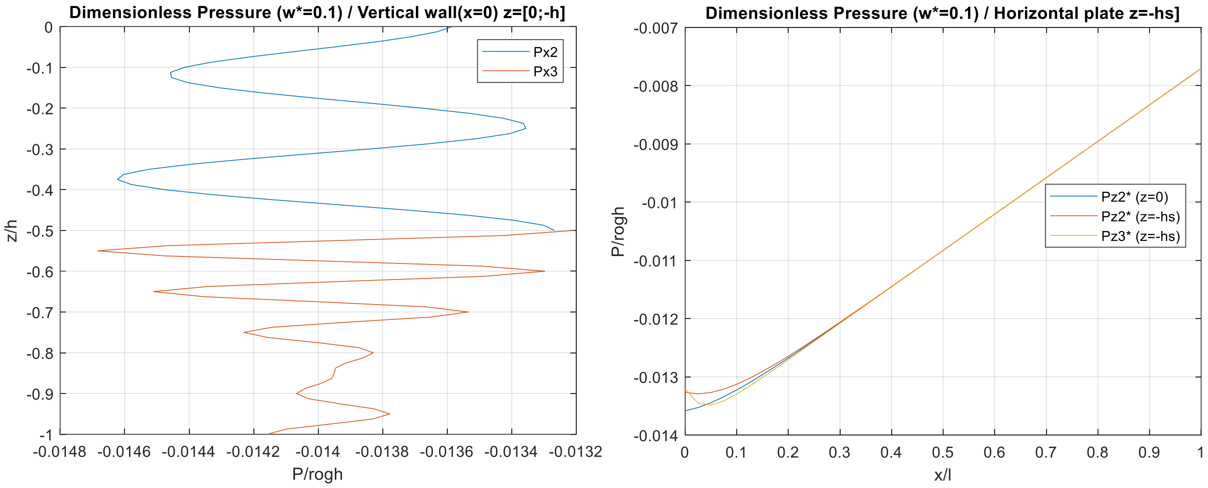

Figure 4.36. Pressure distribution acting on the wall (left) and the plates (right) per regions. (Imaginary parts of complex arguments ignored)

However, besides the conventional approach, this study approach is deeply based on incorporating the imaginary part due to its relation to the Damping Coefficient ($\boldsymbol{N}$) and Memory-effect Function. Thus, the following figures showcase complex arguments for the pressures in each region.

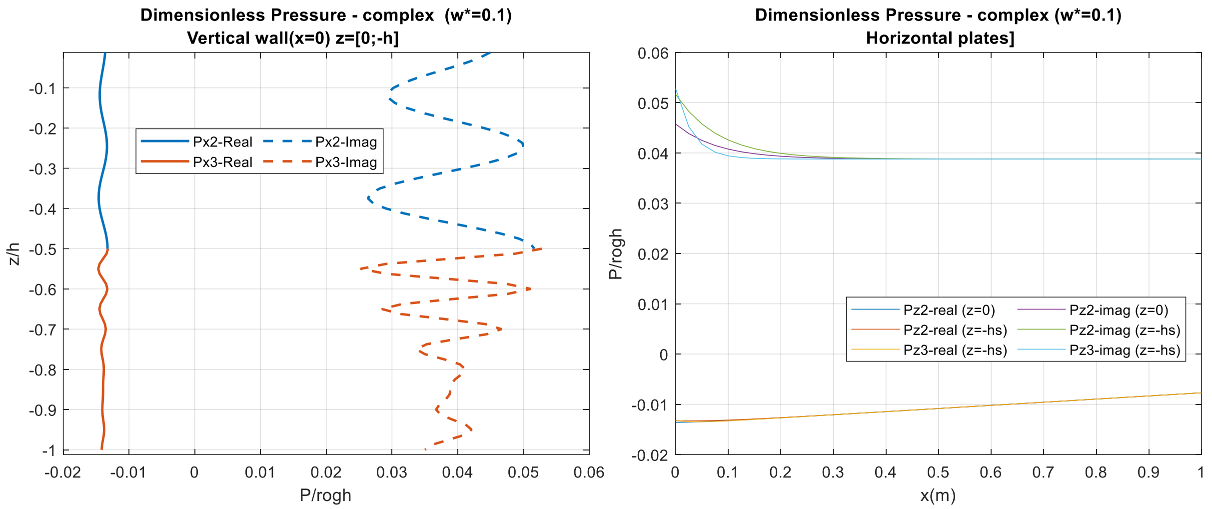

Figure 4.37. Pressure distribution acting on the wall (left) and the plates (right). (Full complex arguments)

From Figure 4.37, larger values of the imaginary part (related to ***N***) in the order of over 3 times the real part (related to ***M***) of the arguments are seen. This gets translated to the forces (Figure 4.38), although not the focus of this subsection, showcasing the significant impact of the Damping when compared with the Added Mass for the case of the double plate, reinforcing the conclusion from the preceding section.

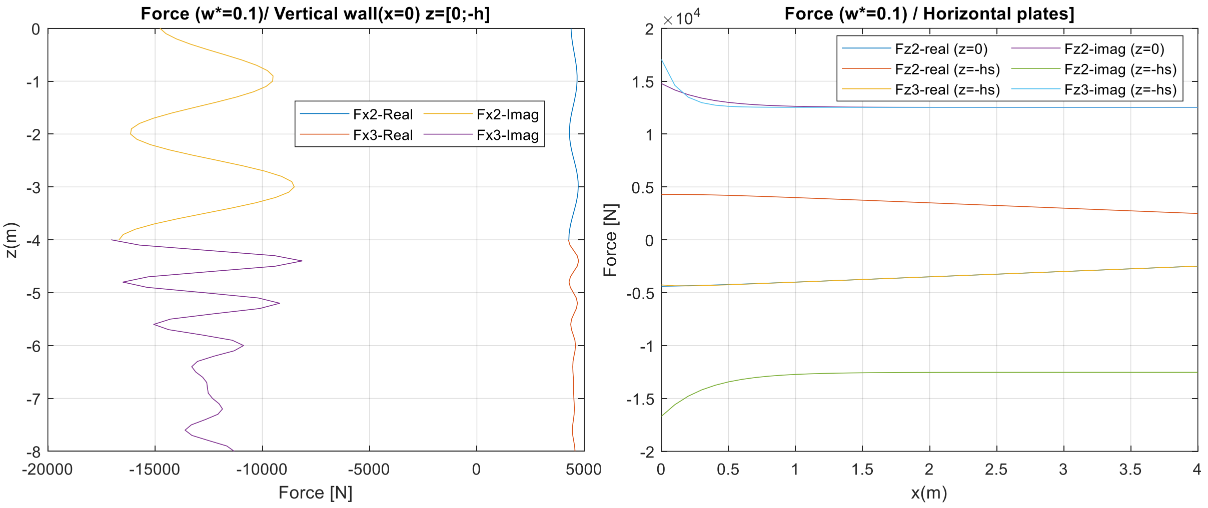

Figure 4.38. Forces distribution on the wall and the plates. (Full complex arguments)

The behavior observed in previous pictures is for ω^* =0.1 (lower frequency). However, in Figure 4.39, analysis for the range ω^* = 0.1, 1.0, 10 and 100 is made. In there, the prevalence of the imaginary part of the pressure is higher for lower frequencies ($\omega^*<10$). While for higher frequencies ($\omega^* \geq 10$), such influence becomes minimal. The average of the imaginary part is around 0 for all frequencies, while the average value of the real part is almost 0 for low frequencies but takes values different from 0 as the frequencies increase.

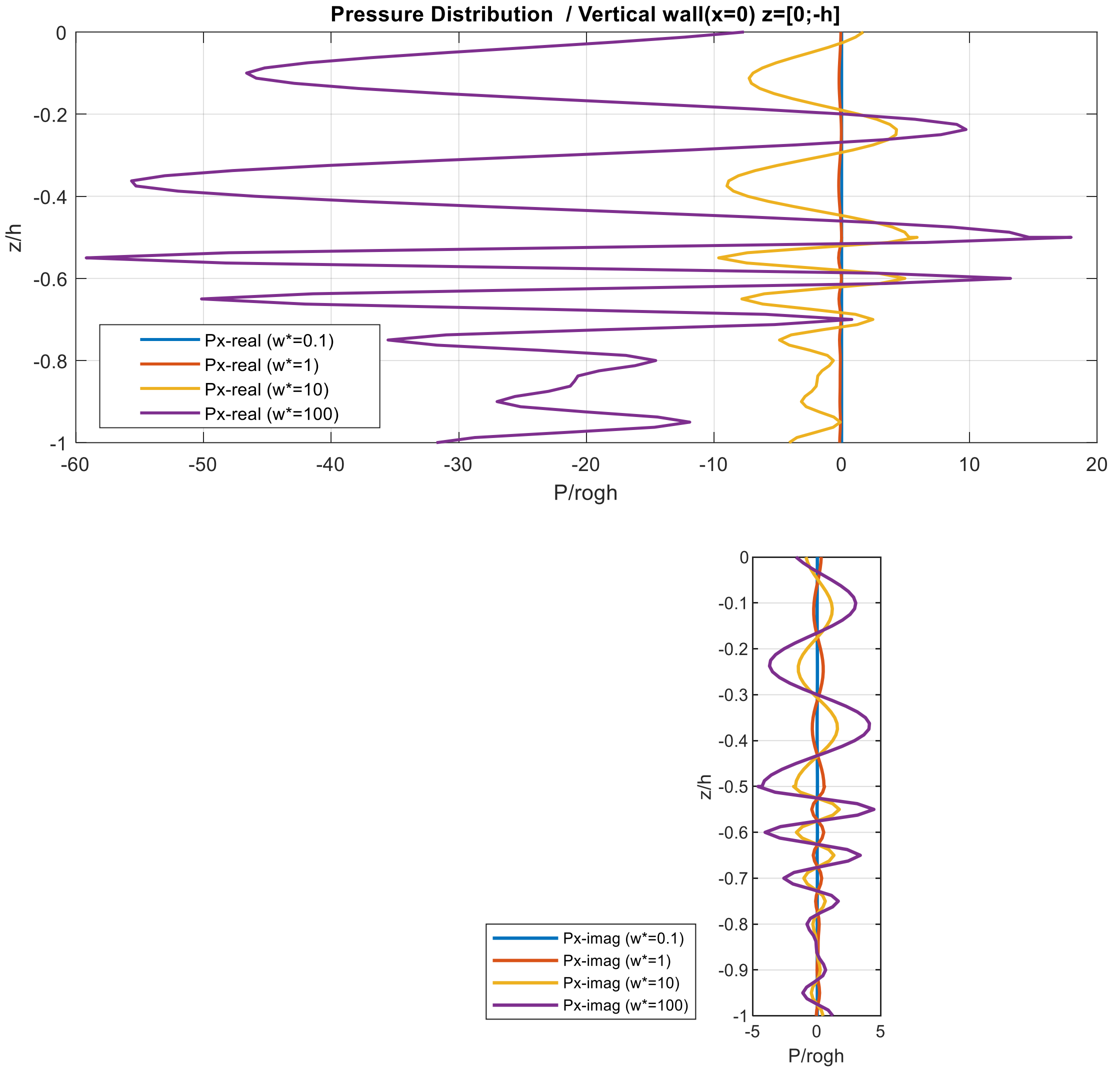

Figure 4.39. Pressure distribution acting on the wall. Influence of the frequency.

In Figure 4.40, the pressure on the horizontal plates is represented. Larger pressure values are reached for larger frequencies. Furthermore, major variations in the pressure are seen in the half of the plate near the wall since the water is more constricted in that zone. It is evident that pressures acting on the second half of the submerged plate (***z*** = -***h**$_s$*) from regions II and II cancel each other; thus, that part of the plate reaches an equilibrium state. Being the pressures acting on the surface plate the main uplifting forces acting on the system. In the horizontal plate, the predominance of the imaginary part is also seen for low frequencies. While the real part grows in importance for larger frequencies ($\omega^*\geq 10$).

Details for each frequency in Figure 4.39 and Figure 4.40 can be observed in the compendium in Figure 4.41 and Figure 4.42.

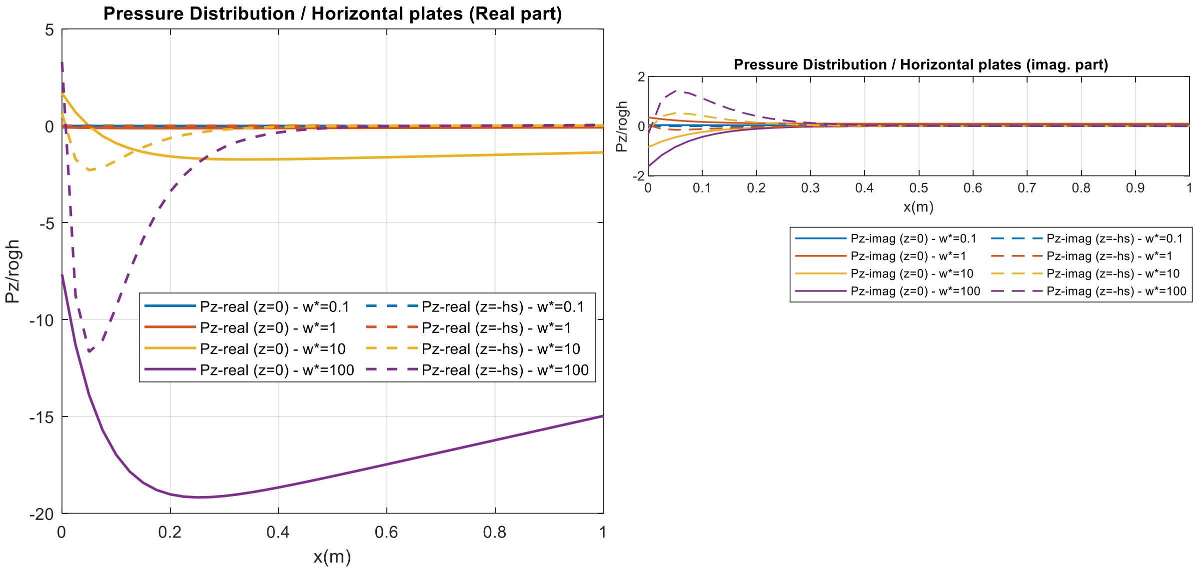

Figure 4.40. Pressure distribution acting on the plates. Influence of the frequency.

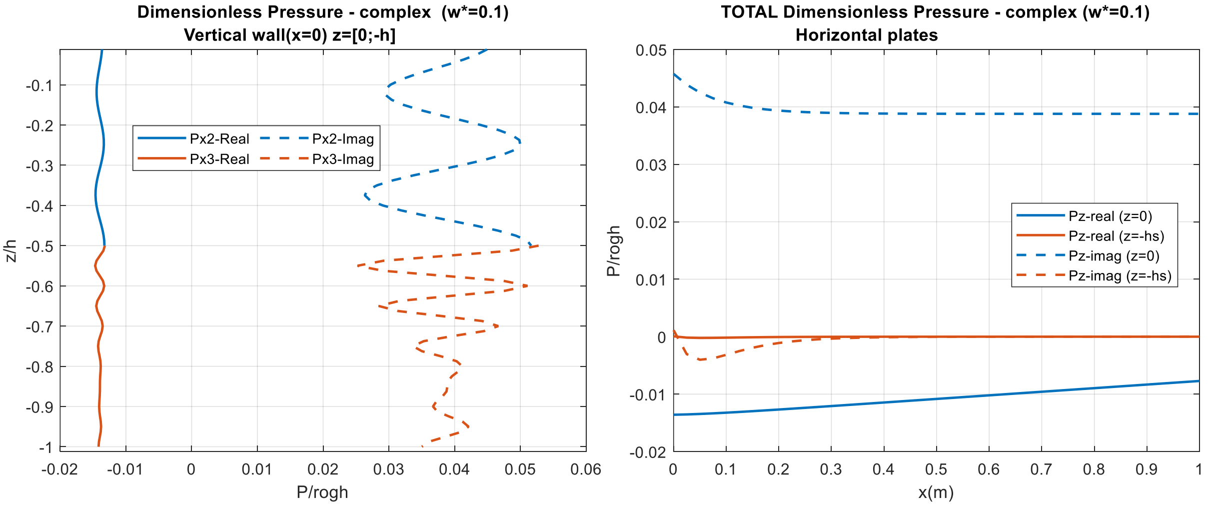

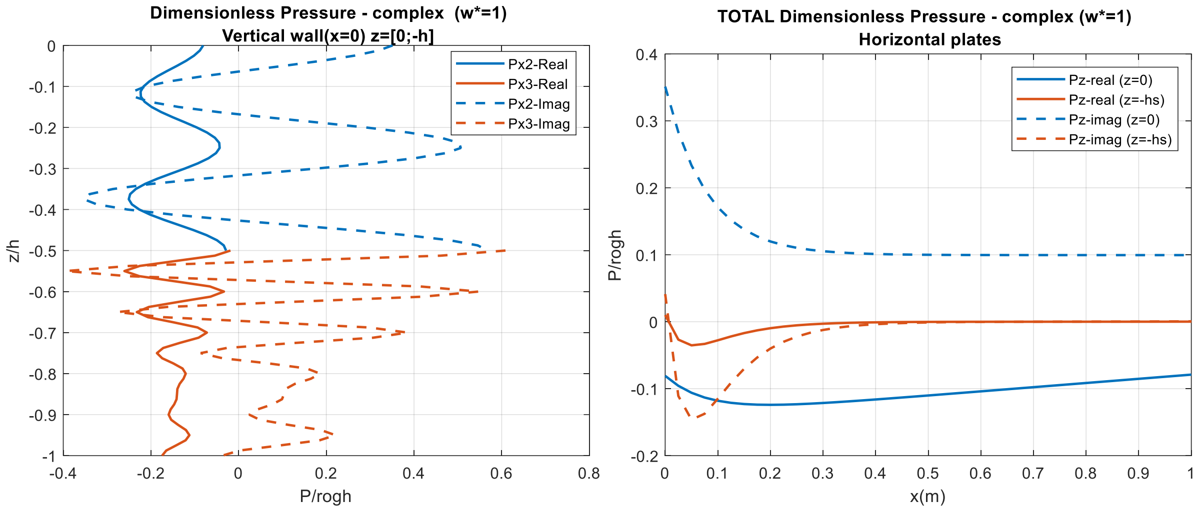

Figure 4.41. Pressure distribution acting on the wall (left) and the plates (right) for frequencies *ω**=0.01 and 0.1. (Full complex arguments). Part 1

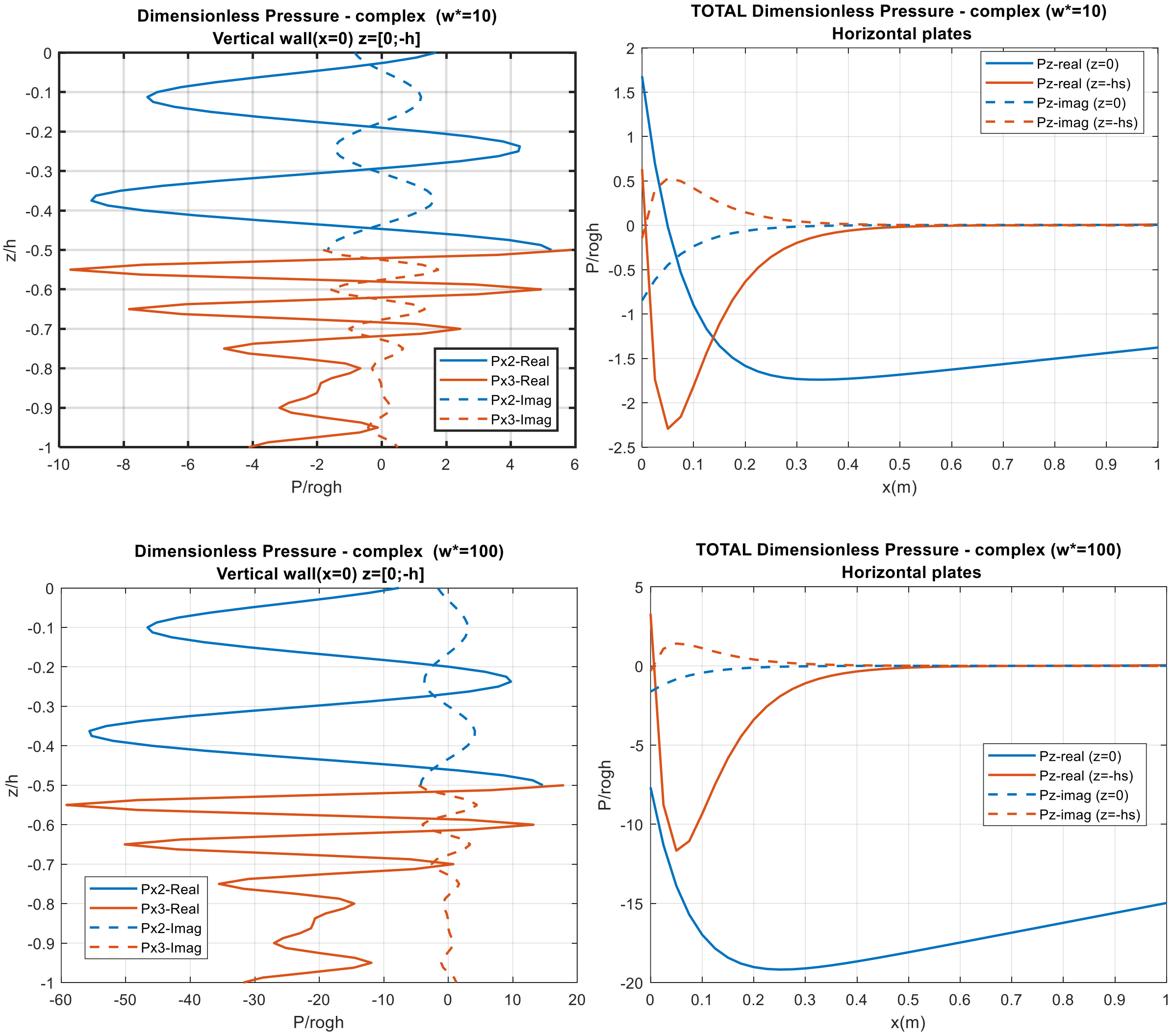

Figure 4.42. Pressure distribution acting on the wall (left) and the plates (right) for frequencies *ω**=0.01 and 0.1. (Full complex arguments). Part 2

Total pressure

The following frequencies $\boldsymbol{\omega^*}$ = 0.1, 5, 10, 15, 20 are used to better compare the total horizontal and vertical pressures, providing a more stable step and easier visualization. The double plate generates a fluctuated pressure distribution on the wall, taking positive and negative values following that pattern. Real and Imaginary parts for the same water depth have opposite signs for larger frequencies $\boldsymbol{\omega^*} > 5$, and the same sign for $\boldsymbol{\omega^*} \leq 5$, although smaller values. Less pressure variation is seen in Region II ($0 \leq \boldsymbol{z} \leq -\boldsymbol{h_s}$) since it is closer to the surface, while more variation is seen in Region III ($-\boldsymbol{h_s} \leq \boldsymbol{z} \leq -\boldsymbol{h}$), especially closer to the plate. Furthermore, less undulating behavior has been observed for the last 20% of the water depth, where the static water pressure due to depth is starting to become more influential. Minimum values are seen near the surface, and maximum values are seen under the submerged plate.

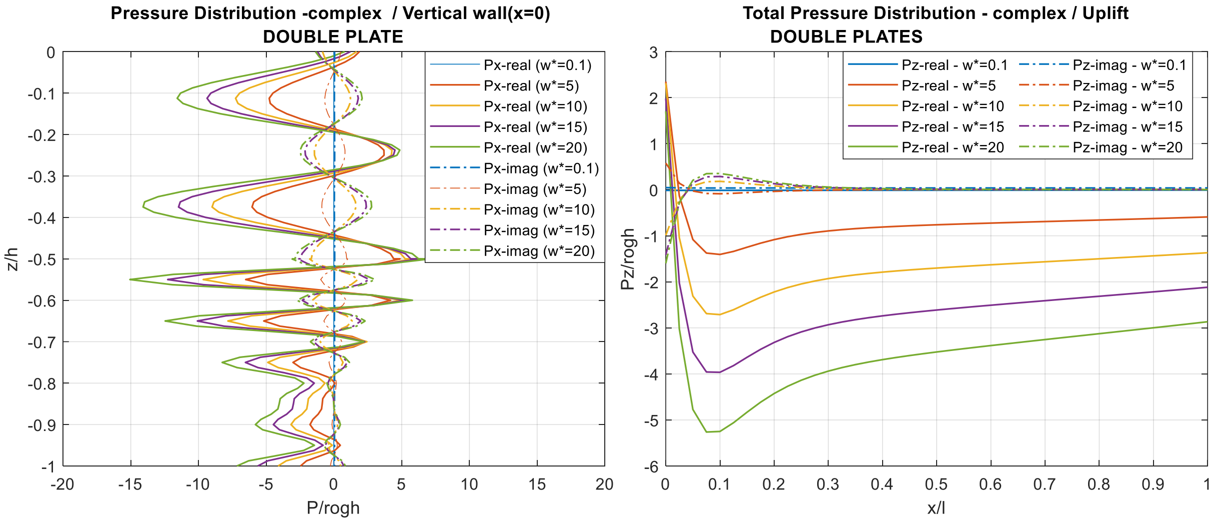

Figure 4.43. Total horizontal (left) and vertical (right) pressure distribution for ω^*=0.1, 5, 10, 15, 20. Full complex arguments. Case: twin plates (z = 0, h/2)

Conversely, the uplift pressures acting on the plates are smoother than the horizontal pressures. They illustrate a damped behavior that switches from one side of the spectrum (positive for the real part and negative for the imaginary part) in the areas near the wall to the other side for the rest of the plates' length. After the switching, maximum values are reached around $\boldsymbol{x/l}$=0.1 to then decrease stably as the distance from the wall to the analyzed point $\boldsymbol{x}$ increases, being larger near the wall and nearly half at the end of the plate.

Figure 4.44 shows details on each plate pressure distribution. The pressure on the submerged plate (*z*=-***h**$_s$*) became zero after ***x***/***l*** = 0.5, i.e., the second half of the plate. The imaginary part in both plates also becomes zero after ***x***/***l*** = 0.5. Being the pressures (real part) on the surface plate (*z*=0) the ones influencing the motion system in that area. While in the first half of the plates, pressures on both plates are to be considered.

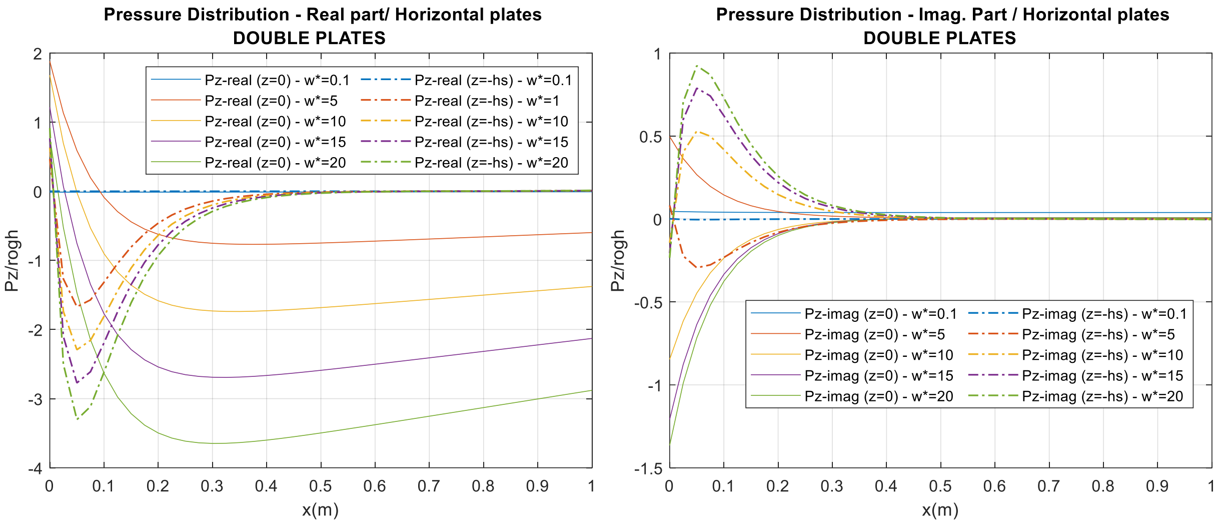

Figure 4.44. Pressure distribution acting on each plate for ω*=0.1, 5, 10, 15, 20.
Full complex arguments. Case: twin plates (z = 0, h/2)

Comparison with single plate case.

When comparing the double-plate cases (Figure 4.44. Pressure distribution acting on each plate for ω*=0.1, 5, 10, 15, 20.) with the single plate (Figure 4.2), the pressure is still superior in the wall than in the plates. For the case of the double plates, the maximum horizontal pressure is about six times higher than the same for the single plate case, while the maximum vertical pressure is about 2.5 higher. Furthermore, the pressure distribution is remarkably wavy compared with the smooth distribution of the single plate case, where the presence of larger plates generated more even distributions. This is the opposite of what Ijima (1971) stated: that double plate pressure distributions to both directions were smoother than for a single plate.

However, the pressure distribution for the double-plate case was not displayed in the mentioned paper, and the plate was on the seaside, from where the incident wave was generated and impacted the wall. While in this research, the plate is on the harbor side, and the incident wave is on the seaside, while the analyzed “incident wave” in this study is a product of the movement of the caisson due to the impulsive incident wave.

Additionally, the vertical pressure distribution has less variation along the plates, with stable minimum values dropping after the third part of the plate length. In contrast, for the single plate, pressures almost linearly drop from the starting to the end point of the plate length. This shows more uniform distributions in the plates due to double plate arrangements.

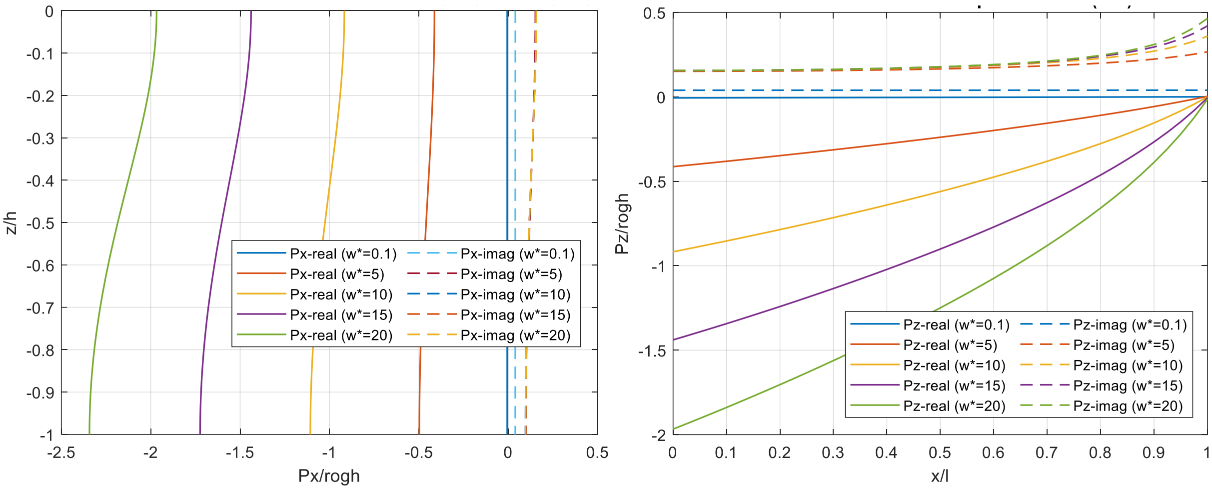

Retrieved Figure 4.2. Pressure distribution acting on the wall(left) and the plate(right) for different frequencies. Single plate at z=0. (Complex arguments)

Analyzing the average pressures in Figure 4.45, the pressures are still superior (almost doubled) in the wall than in the plates. However, the pressures due to the double plate are higher than those due to a single plate at the surface, increasing proportionally to the frequency. On the other hand, pressures for the double-plate case increase at a higher ratio than the single-plate case. The vertical or uplift averaged pressure shows similar behavior to the horizontal pressure but with smaller values. Furthermore, the ratio Pz/Px for the twin-plate case is lower than for a single plate.

Most researchers use average pressure (Ijima,1971) for the calculations; this means that the imaginary part is usually dismissed since their average values generally were almost zero. And that is true for regular caissons, where only a fluid analysis in the horizontal plane is done, and the ratio real/imaginary values is substantial. However, when analyzing plates, such a ratio gets drastically reduced.

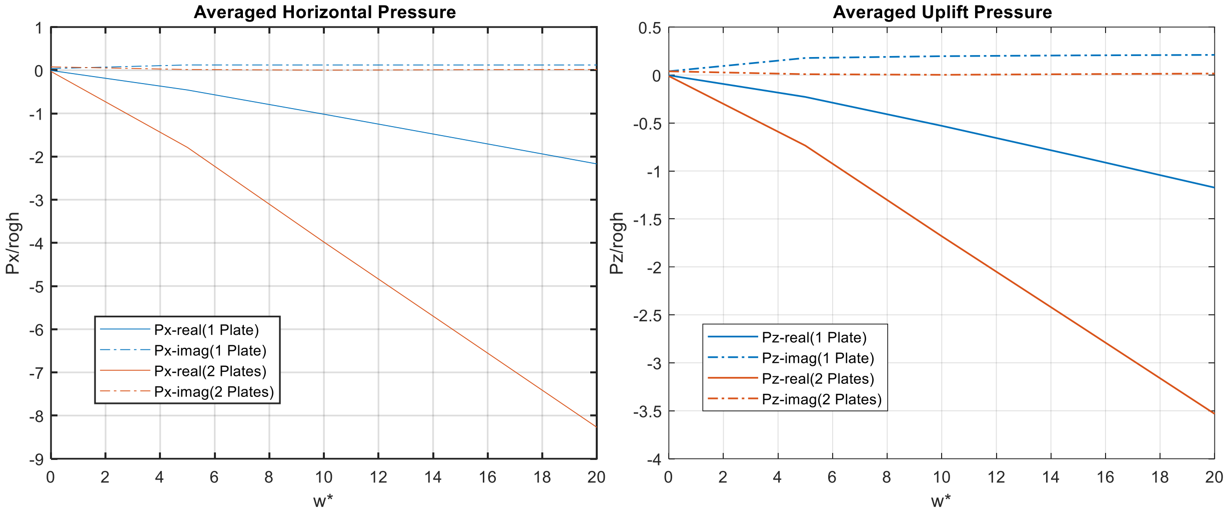

Figure 4.45. Averaged Pressure Distribution (Single-plate v/s Double-plate)

4.2.2 *Hydrodynamic parameter analysis*

The parameters added mass, damping coefficient, and memory-effect function in each region are analyzed in this subsection, as well as their total values and their horizontal and vertical components. Total values are the summation of the regions implied in each analysis.

$$M_{xx} = M_{xx}^{II} + M_{xx}^{III} \tag{4.3}$$

$$M_{zx} = M_{zx}^{II}(z=0) + M_{zx}^{II}(z=-h_s) + M_{zx}^{III}(z=-h_s) \tag{4.4}$$

$$N_{xx} = N_{xx}^{II} + N_{xx}^{III} \tag{4.5}$$

$$N_{zx} = N_{zx}^{II}(z=0) + N_{zx}^{II}(z=-h_s) + N_{zx}^{III}(z=-h_s) \tag{4.6}$$

Some of the components of the above equations have opposite signs, mainly the following vertical components such as $M_{zx}^{II}(z=0)$, $M_{zx}^{III}(z=-h_s)$, $M_{zx}^{II}(z=0)$ and $M_{zx}^{III}(z=-h_s)$. However, for the most straightforward comparison of the values, it was considered the same sign, disregarding region or direction.

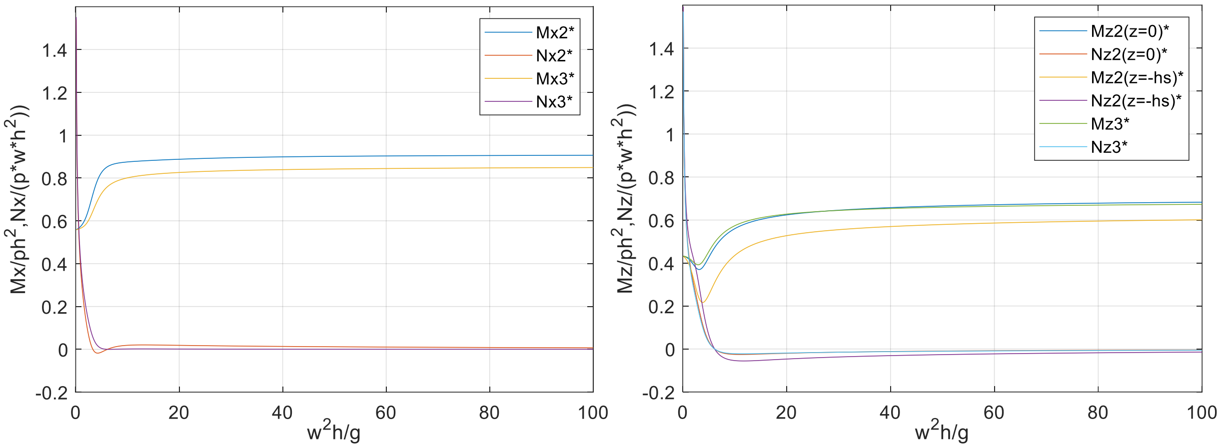

Figure 4.46. Dimensionless Added Mass and Damping Coef. at the vertical Wall (x=0) [left] and at the plates (z=0, -h_s) [right] in Regions II and III.

From the dimensionless added mass at the wall (although both regions have the same boundary conditions and water column length), the added mass acting on the wall for Region II is larger than that of Region III. It is a fact that the hydrostatic pressure is lower in Region II due to a lower location, but due to the wave-induced effect, the hydrodynamic pressure tends to be higher at the surface, which translates to the added mass.

When analyzing the plates, [$\boldsymbol{M_z^{II}}$ (z=0) and $\boldsymbol{M_z^{III}}$] and [$\boldsymbol{N_z^{II}}$ (z=0) and $\boldsymbol{N_z^{III}}$] are similar, indicating that similar values of uplift forces act on both plates. The added mass in Region III of the submerged plate ($\boldsymbol{z=-h_s}$) is higher than in Region II. This aligns with the higher pressures generated under the submerged plate, although the two regions have the same water column length and boundary conditions. On the other hand, the damping under the submerged plate

(N_z^{III}) reaches 0 values and stabilizes from lower frequencies than over the plate Region II [N_z^{II} ($z = -h_s$)].

For low frequencies, M_z slightly declines in most cases, then recovers, increases, and follows the typical asymptotic behavior. The lower peak is more noticeable in the M_z acting over the submerged plate (Region II-Mz2). This behavior is not seen in the total $M_{total} = M_{xx} + f * M_{zx}$. Note that M_x and M_{xx} are used indistinctly, representing the added mass produced in the horizontal direction due to the horizontal movement of the caisson. The same applies for M_z and M_{zx}, but in this case, they are the added mass produced in the vertical direction due to the horizontal movement of the caisson. This use of the subscript is also used with the damping coefficient and the memory-effect function. The total value of the parameter in the wall and the plate are the summation of their components from each region.

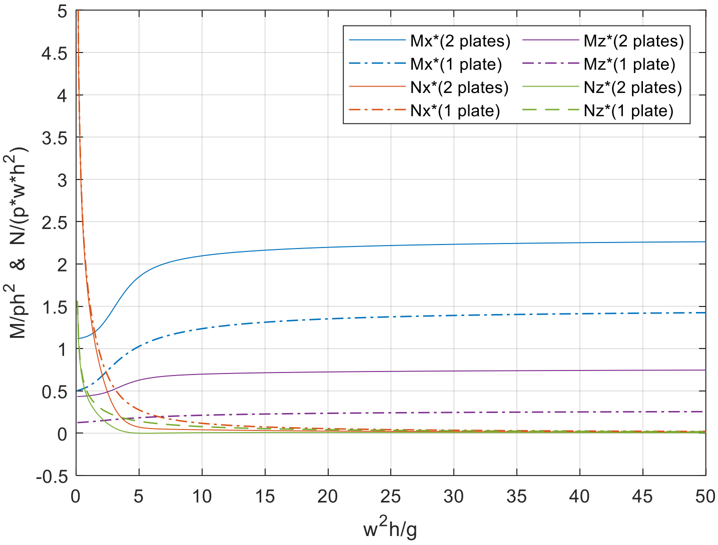

Figure 4.47. Dimensionless Added Mass and Damping Coef. (single and twin plate cases)

The relation $M_x > M_z$ remains for the double plate analysis, M_x doubling the initial value of M_z for low frequencies and a tendency to triple the asymptotic value at infinite frequency. Both curves' behavior follows a similar tendency as in the single plate case. For a comparison with the case of the single plate, Figure 4.47 includes the hydrodynamic parameters for such case as discontinuous lines. As expected, the values of added mass are higher for the double plate since the water constriction increases, while the damping coefficient has a steeper decline since more solid boundaries act as flow stabilizers. Additionally, a fundamental analysis based on the added mass relationship is performed to visualize the best arrangement. In Figure 4.48, for easier comparison, it was considered a positive sign for M_{zx}; thus, the relation $M_{xx}+f_s*M_{zx}$ derives to $M_{xx}-f*M_{zx}$. The same is applied to the Damping Coefficient and Memory-effect function.

Table 4-4. Directional Added Mass Relationships for none, single and double plates.

Case	Mxx	Mzx	Mzx/Mxx	Mxx-fs*Mzx	% Increment
0 plate	1.085	-	-	1.085	-
1 plate (z=0)	1.475	0.271	0.184	1.312	20.9
2 plates (z=0, h/2)	2.316	0.7659	0.331	1.856	71.0

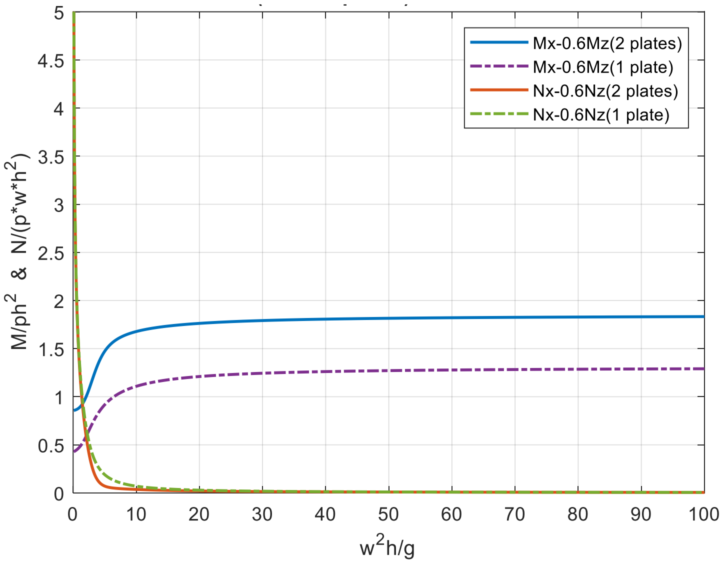

Figure 4.48. Total Dimensionless Added Mass and Damping Coef. (single and twin plate cases)

Total added mass ***M*** is higher for the two plate arrangement, with a total increment over the single plate case of around 40%, and 70% with respect to a regular caisson. On the other hand, the total damping coefficient ***N*** is smaller in the range $1<\omega^*<30$ approximately, although the values near 0 remain the same. The area under the curve is reduced too, i.e., ***R(t)*** is expected to have smaller values.

The memory-effect function in each direction (Figure 4.49 - left) is presented below. The horizontal memory-effect function $\boldsymbol{R_{xx^*}}$ has higher values at each time step than the vertical $\boldsymbol{R_{zx^*}}$, while also having a slower damped effect. Note that although the components have the same sign for better visualization, $\boldsymbol{R_{zx^*}}$ has negative values according to the sign convention based on the direction of the implicated forces. Hence, the total dimensionless memory effect function $\boldsymbol{R_{xx^*}}$ - $\boldsymbol{fR_{zx^*}}$ is in Figure 4.49 (right), showing a low value and a damped behavior in the range 0<t*<3 while reaching 0 around t*=15.

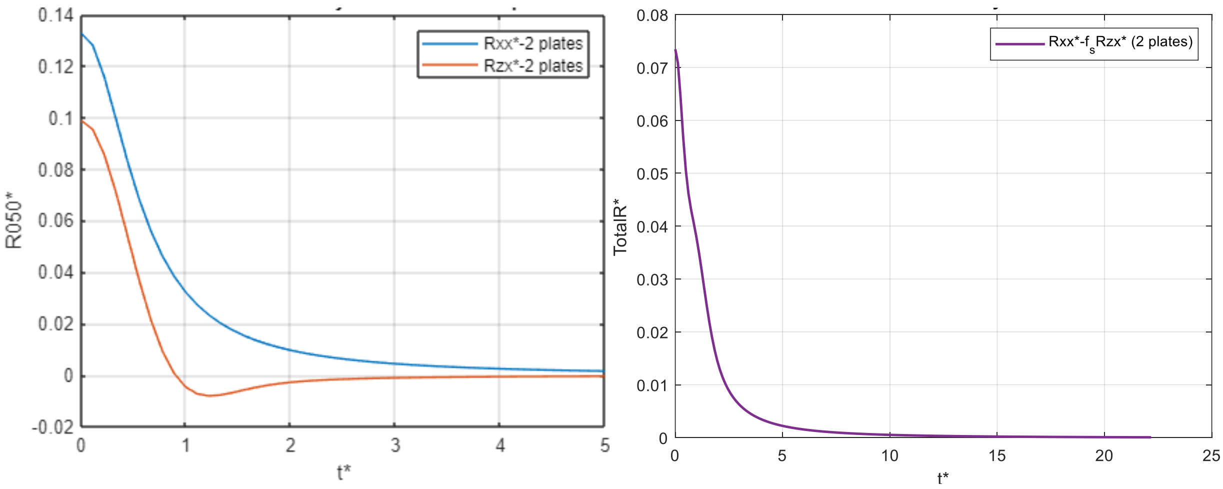

Figure 4.49. Horizontal and vertical (left) and total (right) dimensionless memory-effect function for twin plates.

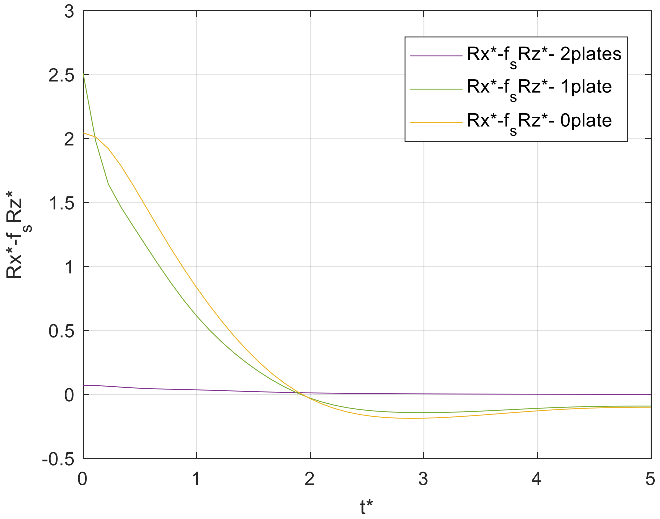

Figure 4.50. Total Dimensionless Memory-effect function (single, twin and no plate cases).

For a single plate with length $\boldsymbol{l}=\boldsymbol{h}/2$ located at the surface, the maximum value of the relation $\boldsymbol{R_{xx}}\text{-}\boldsymbol{f_s}{*}\boldsymbol{R_{zx}}$ [$R^*(0) = 2.5$] was not inferior to the case without a plate with $R^*(0) = 2.17$ (see Figure 4.50). However, the total Dimensionless Memory-effect Function for two plates is almost zero $R^*(0) = 0.07$. The small values for damping coefficients and memory-effect function in twin plates should not be a surprise since they are the result of a more considerable influence in the system reducing or preventing the wave oscillation and promptly dissipating the generated wave due to the caisson motion.

One conclusion derived from the analysis of the hydrodynamic coefficients would be that, since the memory-effect function is almost zero for all-time spam, the two-plate sliding simulation mostly depends on the Added Mass. And, although that is the case, larger added mass doesn't necessarily lead to a sliding reduction, as we already observed in the single plate case, if the damping coefficient doesn't positively affect that reduction. This could be preliminary predicted when larger $R^*(0)$ values are seen.

4.2.3 *Sliding*

The solutions to the motion equation for the double plate are displayed in Figure 4.51, as well as for the single plate at the surface and regular caisson for comparison. The double plate arrangement has a larger motion duration than the single and no-plate cases. The maximum velocity is slightly higher than the single plate and lower than the no-plate caisson and is reached later than both. More importantly, the sliding is higher than the single plate and the regular caisson for 11% and 7%, respectively. This can be explained by recalling the statement in the preceding section: two-plate sliding calculation is primarily dependent on the added mass since the memory-effect function was mainly null. It is similar to removing the latter from the motion equation, leading to an increment of the total sliding, which aligns with the conclusions from subsection 4.1.3.5 about the influence of the inclusion or simplification of the memory-effect function in the motion equation. Basically, the displacements are higher when dismissing ***R*(*t*)**, which is almost zero in the two-plate case naturally.

Nevertheless, as previously stated, larger added mass increases the hydrodynamic resistance, so why does the double plate have a larger displacement and there is no sliding reduction? This is due to the importance or weight of each hydrodynamic parameter: added mass and memory-effect function. To understand it better, a simple ratio of M_∞* and ***R****(0) for the three cases in Figure 4.51: no plate, simple plate and double plate is presented in Table 4-5.

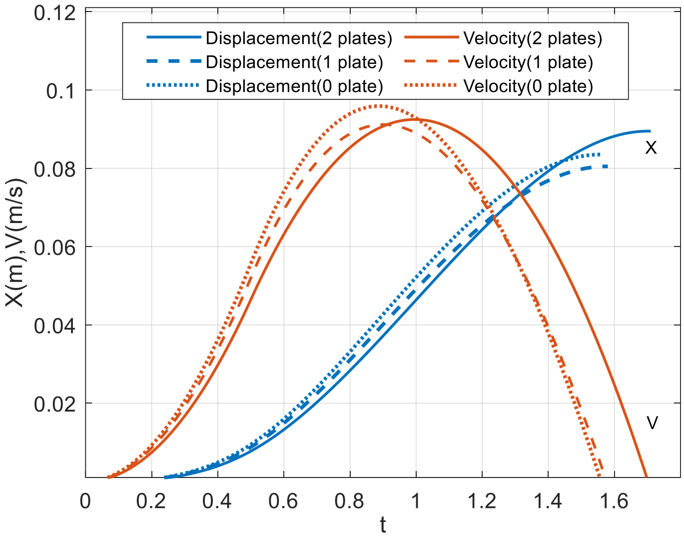

Figure 4.51. Total dimensionless memory effect function (single, twin and no plate cases).

Table 4-5. Ratio of values of M* and R(0)

M*	**0-plate**	**1-plate**	**2-plate**
0-plate	-1-	1.24	1.65
1-plate	0.85	-1-	1.33
2-plate	0.6	0.75	-1-

R*(0)	**0-plate**	**1-plate**	**2-plate**
0-plate	-1-	1.29	*0.03*
1-plate	0.78	-1-	*0.03*
2-plate	*31*	*40*	-1-

The ratio is column/row of the tables: e.g. 0.6 is the result of ***M****(0-plate) / ***M****(2-plate). Values between 0.5 and 2 show variances of 100% within the same parameter comparison; this is seen in ***M****. However, comparative values far from that range display an unbalanced relation within the parameter, as seen in the ***R****(0) ratios related to the double plate. Similar values show a relative balance when comparing the two parameters: ***M**** and ***R****(0), but disproportional differences display unbalance. That is the case again for the twin plate: although the ratios are similar for others, e.g., for 1-plate / 0-plate, the ***M**** ratio is 1.24, and ***R****(0) ratio is 1.29; for the double plate, it is far different, e.g. for 1-plate / 2-plate is 0.75 for ***M**** ratio and 40 for the ***R****(0) ratio.

4.2.4 *Conclusions for the double plate*

The double plate arrangement conveys higher pressures acting on the wall and the plates, while more uniform distributions are seen on the plate but less on the wall. Furthermore, it increases the added mass of the structure; however, it drastically reduces the memory effect, which led to an increase in the sliding of 11% and 7% compared to those for the single plate and the regular caisson, respectively. This confirmed that an increase in the added mass does not lead to smaller displacement.

4.3 CHAPTER CONCLUSIONS

In this chapter, an analysis of the pressures and the hydrodynamic coefficients is performed for caissons with horizontal plates. Their changes according to the location, length, submersion, and number of plates are estimated and analyzed in order to define their influence on the sliding for such geometries. Such parameters are calculated by applying the simulation models and methods described in Chapter 2.

The Boundary-Point Selection Method (BPSM) was applied with excellent results in finding solutions for boundary problems related to breakwaters with horizontal plates. Its application simplifies formulations and reduces computing and programming time. However, it is limited to geometries where the fluid regions have constant water depth. Additionally, aspects related to the application of the Boundary Point Selection method were highlighted, such as the increment of selection points for submersion depths smaller than 25% of water depth to avoid unstable or error results.

Following the main findings in this chapter regarding pressures: a) Reasonable distributions according to the boundary conditions were obtained b) The horizontal plates affect the pressure distribution on the caisson, mostly bringing more uniform distributions at the wall for the case of the single plate and at the plates for the twin-plate case as well as higher pressure values, especially for the double plate, although with more variations on the wall distribution c) Regarding the plate length, the role of the plate as a pressure equalizer is confirmed: when plates' length tends to be equal to the water depth, the plate starts functioning as a pressure equalizer. c) The ratio of the imaginary to the real part of the pressure complex values varies according to the different plate arrangements; thus, its influence should not be dismissed when analyzing annexation elements such as horizontal plates since their geometry resists the forces acting in that direction.

The analysis results confirmed the critical influence of uplift forces on the sliding calculations, as well as the importance of including the memory-effect function on it. Excluding the first one leads to overestimating the horizontal plate's positive influence in reducing the sliding, especially for large *l/h* ratios. Dismissing the latter overestimates the maximum sliding distance.

The double plate analysis confirmed the increments of the added mass; however, it also showed a drastic reduction of the memory effect, which led to an increase in sliding. This confirmed that an increase in the added mass does not lead to smaller displacement and that the memory-effect function plays an important role in the sliding simulation under impulsive wave loads, which has been underestimated. Additionally, a relation in which shapes with larger damping coefficients, on the other hand, with added mass increments, induce better structure performance. Furthermore, for a preliminary prediction of better performance, i.e., a reduction of the sliding distances, analysis based only on the Added Mass is not enough; instead, also searching for sections with larger values of memory effect focusing on larger values of $R^*(t=0)$ should be included.

Chapter 5. EXPERIMENTAL STUDY

OUTLINE

As part of the study of the influence of the horizontal plates in the sliding of breakwaters caissons, wave flume experiments are carried out at Osaka University's Hydraulic Laboratory indoor facilities, measuring the horizontal sliding distance of a vertical breakwater in 1:20 scale with rear horizontal plates due to impulsive waves higher than design. The cases subject to study are caissons with a single submerged horizontal plate, including the special case with the plate at the surface, and caissons with multiple plates considering the variation of plate(s) lengths and submersion depths.

The methodology covers the wave generation of an impulsive wave at a target location, measurements of the wave force acting on the caisson, and the sliding due to the wave impact. The analysis is based on the data recorded from wave height gauges and load sensors for the time series of the wave elevation and forces acting on the caisson, respectively, while displacement is obtained by image analysis.

Throughout, we seek to experimentally reproduce the impulsive wave generation using the Aoki-Koga method and estimate the characteristics of the wave forces acting on the structure. More importantly, it is also pursued to clarify the effect of the horizontal plate's length and submersion on the sliding of breakwater caissons, as well as confirming the fit of the sliding analytical models presented in chapters 3 and 4 to the experimental results.

5.1 EXPERIMENTAL SET-UP AND TEST CONDITIONS

The physical model experiments are conducted in the two-dimensional wave flume of the Hydraulic Laboratory of Osaka University. The wave flume is 20m long, 0.7m wide and 1m deep. It is equipped with a piston-type generator at one of its ends, able to generate both regular and irregular waves, and it will be used for the generation of the single impulsive waves necessary for this study. At the terminal end, a wave-absorbing surface is located as an artificial beach that minimizes the waves' reflection reaching the flume's end.

As shown in the side view of the experimental set-up's sketch, up to six wave gauges are located to measure the wave height at each location and time duration of the impulsive wave: one at the front face of the structure, another three in front, and two after it. Furthermore, two video cameras are located over and at the side of the target locations to capture the movement of the caisson, which is later measured using video analysis tools.

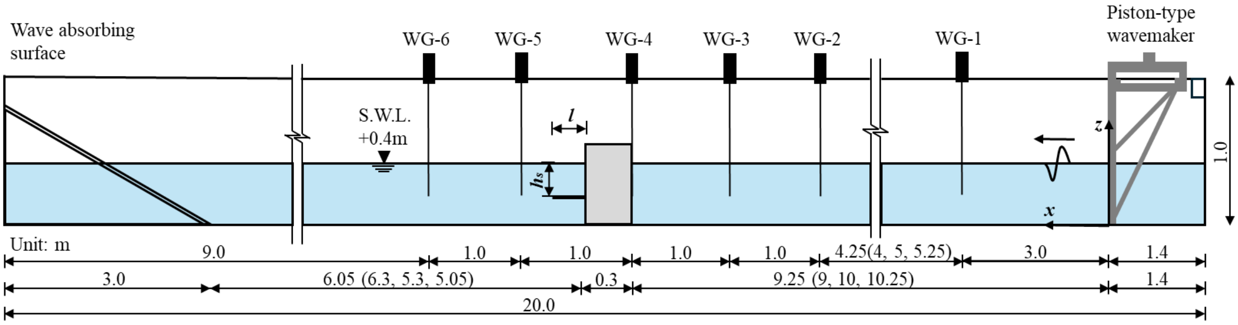

Figure 5.1. Sketch of the experimental set-up

5.1.1 *Caisson Model*

The geometrical characteristics and properties of the prototype used in the analytical study and the 1:20 scale model to be used in the experimental study are displayed in Table 5-1. The length of the model was taken to cover the width of the wave flume, sparing 2cm at each side to allow the collocation of the beams for plate adjustment and avoid the silicone-like bottom-wall joints of the flume that could affect the sliding due to different friction factors.

Table 5-1. Geometrical characteristics and properties of the prototype and the model

Geometric Characteristics / Properties	Symbol	Prototype	Model Scale 1:20
Caisson length (orthogonal to wave direction)	$\boldsymbol{L}$	-1- m	0.66 m
Caisson width (in wave direction)	$\boldsymbol{B}$	6 m	0.3 m
Caisson height	$\boldsymbol{H}$	10 m	0.5 m
Freeboard	$\boldsymbol{d}$	2 m	0.1 m
Water depth at the wall	$\boldsymbol{h}$	8 m	0.4 m
Water density	$\boldsymbol{\rho}$	1030 kg/m^3	1000 kg/m^3
Material density	$\boldsymbol{\rho_c}$	2100 kg/m^3	1585 kg/m^3
Gravity acceleration	$\boldsymbol{g}$	9.8 m/s^2	9.8 m/s^2
Volume	$\boldsymbol{V}$	60 m^3	0.099 m^3
Mass	$\boldsymbol{M}$	126000 Kg/m	75.4-138 kg

A box of 300x660x500mm made of clear plexiglass of 10mm thickness represents the caisson model, filled with coarse white sand until reaching the desired mass. Two metallic beams are added to the sides of the box at 0, 10, 20 and 30 cm from the water surface according to the case, while wood panels of 65 x 10, 20, 30 and 40 cm are attached to the beams simulating the horizontal plates.

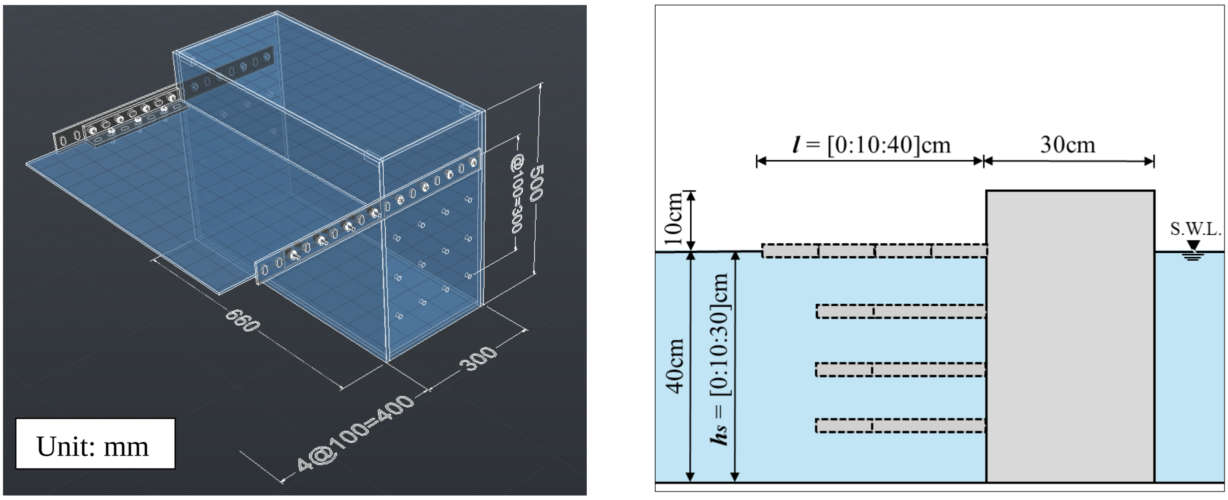

Figure 5.2. Caisson Model: Isometric of the model (left) and side view of the plate configurations (row).

Eleven configurations are tested in terms of plate length and submersion, including a no-plate case, represented in Figure 5.2 and summarized below.

Table 5-2. Summary of Test Cases

No.	Case Name	Plate Submersion Depth (h_s)	Plate Length (l)
1	HS0_PL0	0 cm	0 cm
2	HS0_PL10		10 cm
3	HS0_PL20		20 cm
4	HS0_PL30		30 cm
5	HS0_PL40		40 cm
6	HS10_PL20	10 cm	20 cm
7	HS10_PL30		30 cm
8	HS20_PL20	20 cm	20 cm
9	HS20_PL30		30 cm
10	HS30_PL20	30 cm	20 cm
11	HS30_PL30		30 cm

5.1.2 *Friction Test*

The caisson exerts resistance force induced in part by the friction force between the caisson's bottom surface and the flume's surface. Such resistance force should be estimated for the practical design. The frictional force can be simply predicted through the friction factor. Hence, a coefficient of friction test is conducted, which determines “the resisting force tangential to the interface between two bodies when, under the action of external force, one body moves or tends to move relative to the other,” according to the ASTM standard G-40.

A wire is attached to the empty caisson model and initially pulled to prevent loosening. For the test, the caisson model is pulled until displacement is reached. The tensile force is measured with a Newton scale, and the maximum value reached that generated the start of the movement is selected.

Figure 5.3. Newton scale used for measuring friction force.

The pulling model tests were repeated ten times in the same condition, taking into consideration that manual pulling may introduce more errors. The average value of the measured tensile forces was employed as the value of static frictional force in the calculation of the friction factor as in Eq.(2.1), where $\boldsymbol{F_s}$, $\boldsymbol{m}$ and $\boldsymbol{g}$ represent the tensile force of the wire, the empty caisson mass, and the gravitational acceleration, respectively.

$$f_s = F_s/(mg) \tag{5.1}$$

Tensile forces ranged between 27.1N and 30N. Since the empty caisson has a mass of 7.9kg, the design friction factor between the caisson made of plexiglass and the surface of the flume bottom made of aluminum under wet conditions is 0.37. This value is close to the expected range of [0.4~0.5] from the closest conditions in the bibliography for steel and plexiglass under lubricated conditions.

5.2 WAVE GENERATION.

The wave generation system consists of a hydraulic system, which gives a vertical wave board a horizontal translational movement through a piston. The position of the board is controlled by an electric signal from the wave function or multifunction generator (WFG). The digital record of the signal is converted to an analog electric signal which is fed to the WFG under the arbitrary waveform (ARB). The voltage amplitude of the electric signal is adjusted to 10V, which is the maximum for the multifunction generator, and another 4.5V are added to the input gain of the operation panel of the wave generator.

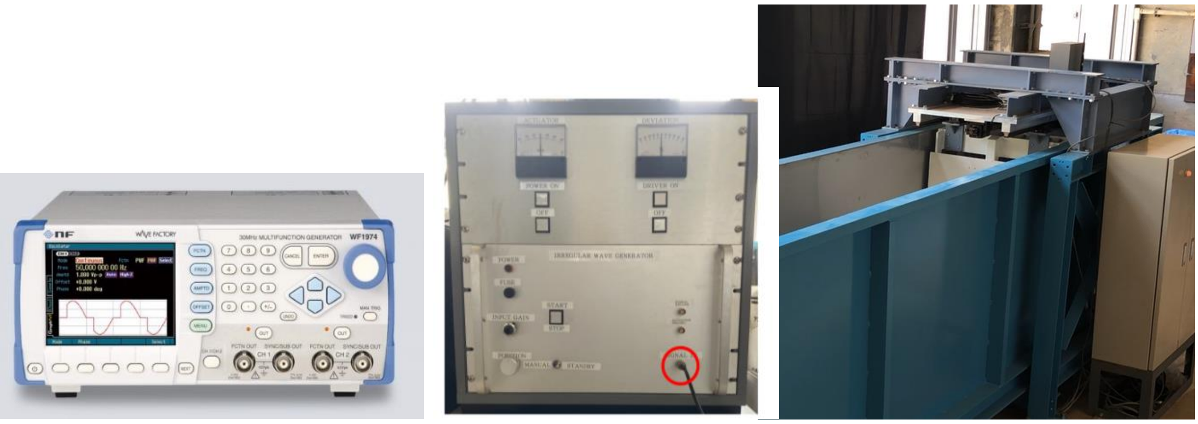

Figure 5.4. Multifunction Generator WF1973/WF1974 (left), operation panel of wave generator (center) and piston-board station at one end of the wave flume (right).

The impulsive waves are most related to caisson sliding. However, the generation of a single concentrated wave at a predetermined location in a flume is not an easy task. Related research has been done in the naval engineering field by Omatsu (1978, 2009) and in the civil engineering field by Usui et al. (2016, 2017), but with some limitations for its easy application in wave flumes. Aoki and Koga (2021) presented a method for generating concentrated waves of arbitrary waveform at arbitrary locations in a channel. The method is intended for wave flumes with a piston-type wave maker and is based on linear systems using frequency and impulsive response functions from linear wavemaker theory. The research was analytically presented and verified numerically but not experimentally. Thus, initial tests are done to confirm it and implement the method in this study.

5.2.1 *Wave-making Signal*

Estimating the motion of the wavemaker board starts by defining the desired waveform $\boldsymbol{\eta}$ (X, $\boldsymbol{t}$) or water level fluctuation at a target position $\boldsymbol{x}$ = X in the wave channel. This function is Fourier transformed and the result is substituted in the frequency response function [Eq.(5.2)], yielding to the obtention of the Fourier transform of the wavemaker (WM)'s board motion. Finally, by inverse Fourier transforming the latter, the time series of the board motion is obtained.

$$\eta^*(\omega) = h^*(\omega)\,\xi^*(\omega) \tag{5.2}$$

Furthermore, the waveform resulting from the wavemaker board motion can be verified by applying the impulsive response function [Eq.(5.3)] to it.

$$\eta(X,t) = \int_{-\infty}^{\infty} h(t)\xi(t-\tau)d\tau \tag{5.3}$$

This calculation flow is presented in Figure 5.5, where $\boldsymbol{\eta}$ stands for water elevation, $\boldsymbol{x}$ for the position, $\boldsymbol{\omega}$ for frequency, $\boldsymbol{t}$ for time, $\boldsymbol{\xi}$ for board motion, and $\boldsymbol{h}$ for the response functions.

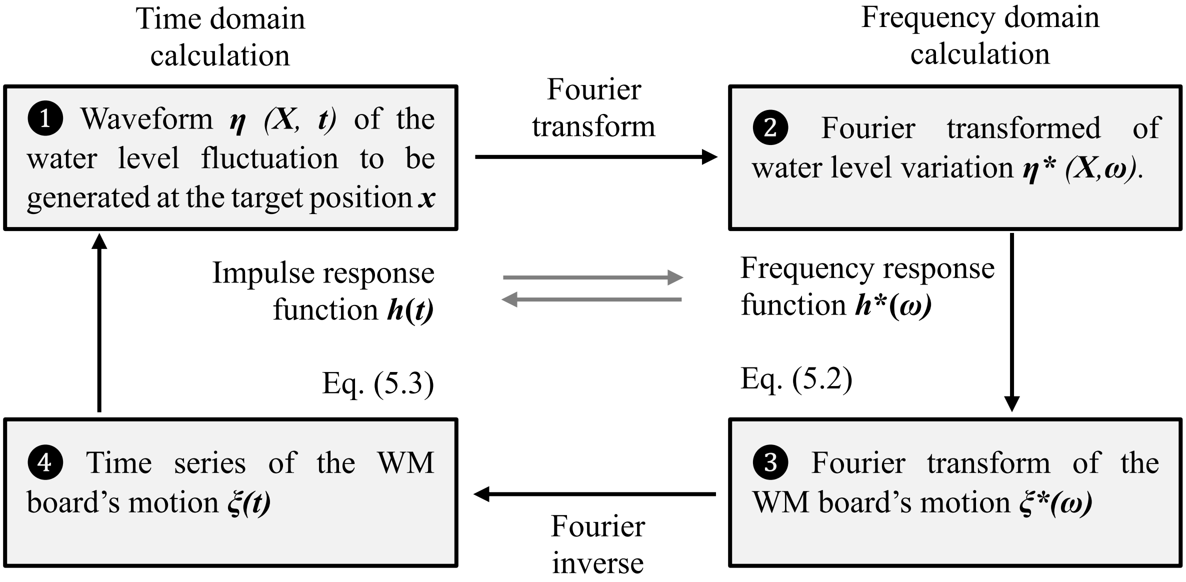

Figure 5.5. Calculation flow for wave-making signals.
(English reproduction of the calculation flow in Aoki and Koga (2021)

The method can be applied to both constant and variable water depths. For our case study, the caisson is located directly on the bottom of the wave flume; thus, it is a case of constant water depth. More details of the derivations within the method for generating concentrated waves of arbitrary waveform at arbitrary locations in a channel can be found in Aoki and Koga (2021).

The Aoki-Koga method is applied to obtain an impulsive wave with the initial below characteristics. These characteristics are higher than those for the design wave since we aim to produce sliding, i.e., structure failure.

Table 5-3. Initial characteristics for the wave-making signal

CHARACTERISTICS	
Waveform	Triangular
Distance from the board	10 m
Water depth	0.4 m
Wave elevation	0.1 m
Period	1 s
Rising time	0.5 s

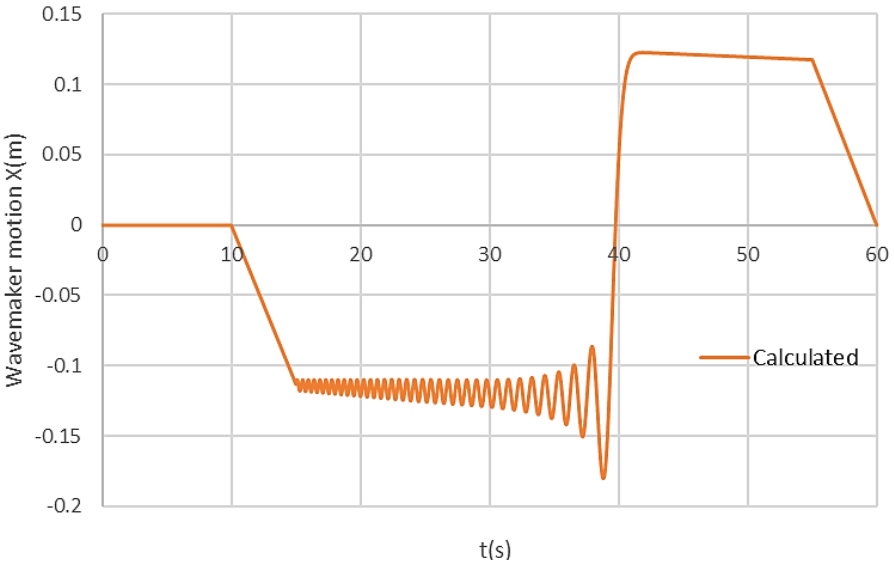

Figure 5.6. Wave-making signal. Case: h=0.4m, X=10m, $\eta(10)$=0.1m, t=0.5s.

The wavemaker board motion should follow then the function presented in Figure 5.6Figure 5.6. Wave-making signal. Case: h=0.4m, X=10m, $\eta(10)$=0.1m, t=0.5s. where a clear sinusoidal movement with increments of period and amplitude is seen up to the last and larger stroke. The direct output of the method application goes from 10s to 50s; however, in order to achieve a smooth return to the initial position and reduce strain on the wavemaker, 10 seconds are added at the end of the signal with a lineal return to zero, and another 10 seconds at the starting point of rest. The digital record of the signal is converted to an analog electric signal which is fed to the WFG under the arbitrary waveform (ARB). The wave height is determined by the amplification WFG. The voltage amplitude of the electric signal is adjusted to 10V, which is the maximum for the multifunction generator, and an input gain of 4.5 is used in the operation panel of the wave generator. The sampling rate of the water elevation was of 0.001 second (1kHz).

5.2.2 *Results*

Figure 5.7 shows the time series wave elevation for the target location (x=10m). However, a doble wave is seen with a $\boldsymbol{\eta_{max}}$ = 8.9cm; thus, neither a unique wave nor the expected elevation is reached at 10m from the wavemaker board. Nevertheless, it also indicates that the targeted characteristics can be obtained a few centimeters later. Hence, a series of locations in the range of 10m to 10.6m were tested, being the later the final location also matching with the video recording requirements.

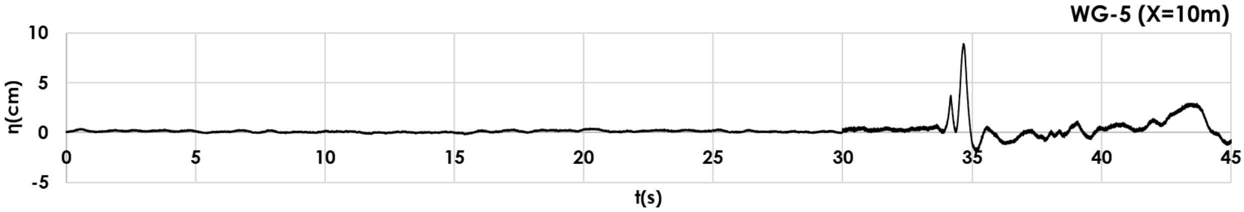

Figure 5.7. Wave-making signal. WG-5 at x=10m. Case: h=0.4m, X=10m, $\eta(10)$=0.1m, t=0.5s.

From Figure 5.8, it is evident that the concentrated wave is the overlapping of multiple frequency waves along the wave flume just before the target location until a unique wave is obtained there (in this study, it is around 25cm after the expected location). This behavior was also seen for a case with X=9m, where the target wave characteristics were obtained at x=9.25m.

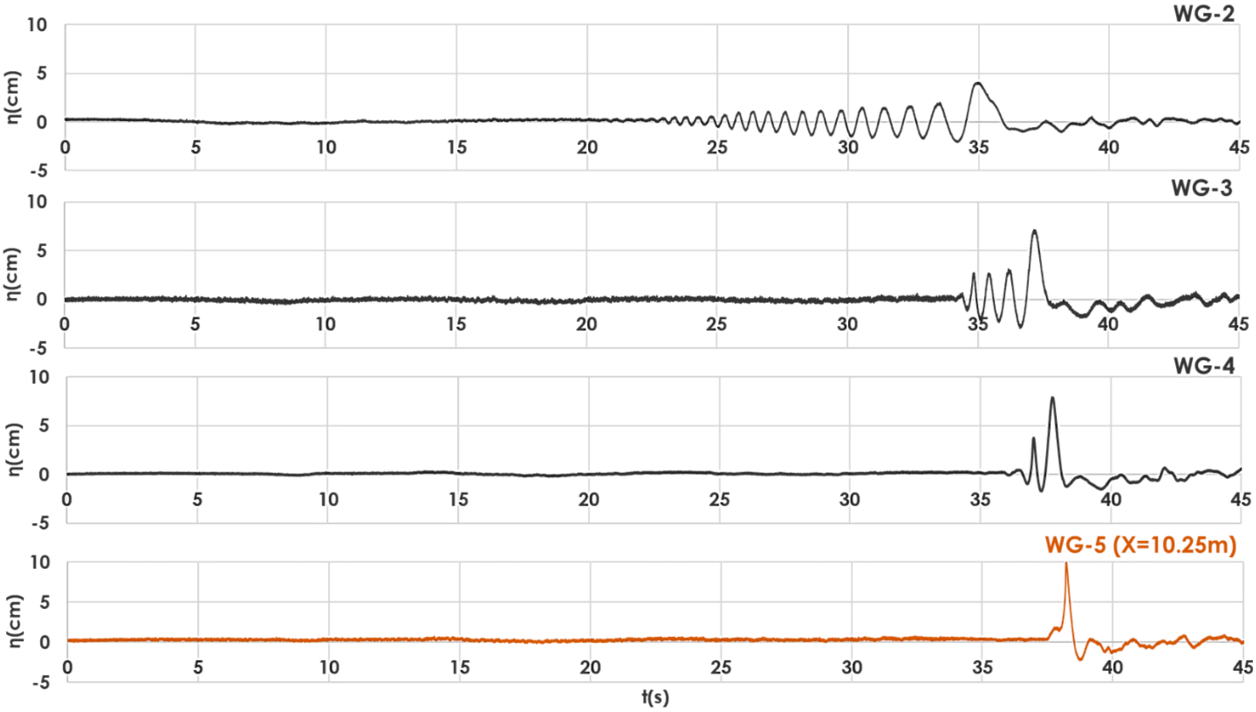

Figure 5.8. Wave-making signal for all wave gauges. Especial case of WG-5 at x=10.25m. Case: h=0.4m, X=10m, $\eta(10)$=0.1m, t=0.5s.

A wave height of 9.991m and a 0.97s period measured from the test agreed very well with the target design values (10m and 1s, respectively). Thus, it can be concluded that the generated waves are both geometrically and dynamically similar to the target produced by the Aoki-Koga method.

5.2.3 *Variation of the wavemaker board movement*

Due to the variation in the target location, the actual board motion is measured using a video analysis tool to experimentally verify whether its motion corresponds to the one obtained based on the linear wave theory and the generation of the desired water level fluctuation. Figure 5.8

shows the ‘Calculated’ and ‘Measured’ representing the calculated board motion sent as an electric signal and the actual observed motion of the board.

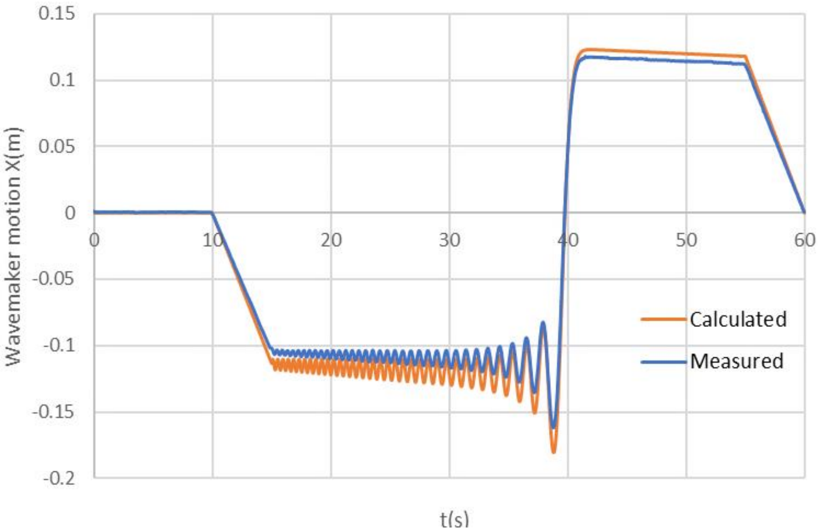

Figure 5.9. Wavemaker board motion

Case: h=0.4m, X=10m, $\eta(10)$=0.1m, t=0.5s.

There is a minimum phase variation at the lower frequencies, but generally, there is not much change in the phase. The actual motion of the wavemaker plate has a lower amplitude than the signal input from the theoretical calculations, with a maximum variation of 8.2%. The phase is slightly displaced for higher motion frequencies but the same for most of the rest, i.e., higher amplitude with a margin of error of R^2=0.9938, MSE= 5.35e-05 and the RMSE=7.3e-03. The wavemaker piston cannot replicate high-frequency movements due to the mechanical nature of the device. Hence, according to the experimental results, the concentrated wave will be reached around 25 cm after the theoretical target location, mainly due to variations in the wavemaker board motion.

Table 5-4. Statistics of the motion of the wavemaker. (Measured vs. Calculated)

	Measured (M)	Calculated (C)	M-C
Maximum displacement (cm)	11.8	12.3	-0.5
Minimum displacement (cm)	-16.2	-18.0	1.8
Maximum amplitude (cm)	27.9	30.3	-2.4

5.2.4 *Numerical simulation*

The wave signal generation method can be applied to numerical wave tanks. Hence, since a variation in the target location has been seen in the physical experiments, a numerical simulation would be a faster way to determine the actual target location before reaching the experimental stages. The numerical study is done in CADMAS-SURF (SUper Roller Flume for Computer Aided Design of MAritime Structure), a free-surface flow simulator based on the volume of fluid (VOF) method studied and developed by the Study Group on Application of Numerical Wave Motion to Wave Resistant Design of Waterways to replace conventional hydraulic model experiments with CFD-based numerical calculations.

5.2.4.1 Basic Equations and Free Surface

The numerical wave flume is based on the continuity equations of continuity for a two-dimensional incompressible fluid and the modified Navier-Stokes formulations. Details of the theoretical description and discretization process of the governing equations are given in the CADMAS-Surf manual book (2001).

$$\frac{\partial \gamma_x u}{\partial x} + \frac{\partial \gamma_z w}{\partial z} = 0 \tag{5.4}$$

$$\lambda_v \frac{\partial u}{\partial t} + \frac{\partial \lambda_x uu}{\partial x} + \frac{\partial \lambda_z wu}{\partial z} = -\frac{\gamma_v}{\rho}\frac{\partial p}{\partial x} + \frac{\partial}{\partial x}\left[\gamma_x \nu_e \left(2\frac{\partial u}{\partial x}\right)\right] + \frac{\partial}{\partial z}\left[\gamma_z \nu_e \left(\frac{\partial u}{\partial z} + \frac{\partial w}{\partial x}\right)\right] - R_x \tag{5.5}$$

$$\lambda_v \frac{\partial w}{\partial t} + \frac{\partial \lambda_x uw}{\partial x} + \frac{\partial \lambda_z ww}{\partial z} = -\frac{\gamma_v}{\rho}\frac{\partial p}{\partial z} + \frac{\partial}{\partial x}\left[\gamma_x \nu_e \left(\frac{\partial w}{\partial x} + \frac{\partial u}{\partial z}\right)\right] + \frac{\partial}{\partial z}\left[\gamma_z \nu_e \left(2\frac{\partial w}{\partial x}\right)\right] - R_z - \gamma_v g \tag{5.6}$$

where $\boldsymbol{t}$ is the time, $\boldsymbol{x}$, $\boldsymbol{z}$ are the horizontal and vertical coordinates, respectively, $\boldsymbol{u}$, $\boldsymbol{w}$ are the horizontal and vertical velocities, respectively, $\boldsymbol{\nu_e}$ is the molecular kinematic viscosity, $\boldsymbol{\gamma_v}$ is the porosity, $\boldsymbol{\gamma_x}$, $\boldsymbol{\gamma_z}$ are the horizontal and vertical sectional transform ratios, respectively, $\boldsymbol{p}$ is the pressure, $\boldsymbol{\rho}$ is the mass density of the fluid, and $\boldsymbol{g}$ is the acceleration due to gravity.

The coefficients of $\boldsymbol{\lambda_v}$, $\boldsymbol{\lambda_x}$, $\boldsymbol{\lambda_z}$ in Eqs.(5.4), (5.5) and (5.6) are:

$$\lambda_v = \gamma_v + (1 - \gamma_v)C_M \tag{5.7}$$

$$\lambda_x = \gamma_x + (1 - \gamma_x)C_M \tag{5.8}$$

$$\lambda_z = \gamma_z + (1 - \gamma_z)C_M \tag{5.9}$$

While $\boldsymbol{R_x}$ and $\boldsymbol{R_z}$ are the horizontal and vertical drag forces defined below, and where C_D is the drag coefficient and Δx, Δz are the horizontal and vertical mesh sizes for the numerical simulation, respectively.

$$R_x = \frac{1}{2}\frac{C_D}{\Delta x}(1 - \gamma_x)u\sqrt{u^2 + w^2} \tag{5.10}$$

$$R_z = \frac{1}{2}\frac{C_D}{\Delta \mathrm{z}}(1 - \gamma_z)w\sqrt{u^2 + w^2} \tag{5.11}$$

For the fluid-free surface, the Volume of Fluid method (Hirt, 1981) is applied, and the transfer diffusion equation F is shown below.

$$\gamma_v \frac{\partial F}{\partial t} + \frac{\partial \gamma_x u F}{\partial x} + \frac{\partial \gamma_z w F}{\partial z} = 0 \tag{5.12}$$

5.2.4.2 Simulation Outline and Results

The numerical wave tank is 20m long, 1m wide and 1m deep. The region is divided into 0.02m cells in the x and y axes and 0.1m in the y axis. A setup for piston-type wave generation is made using the IB method to incorporate the board's motion and considering the moving boundary by including geometry and time series displacement. The board is located 1m from the start of the flume and setups for wave absorption are set at both ends of the flume. Gauges are located along the wave tank every 0.1m for wave elevation, including the location of the structure, and the latter includes pressure and velocity measurements. The calculation time is set for 40 seconds, and the time step is set for 0.001s (higher time steps led to fluid instabilities).

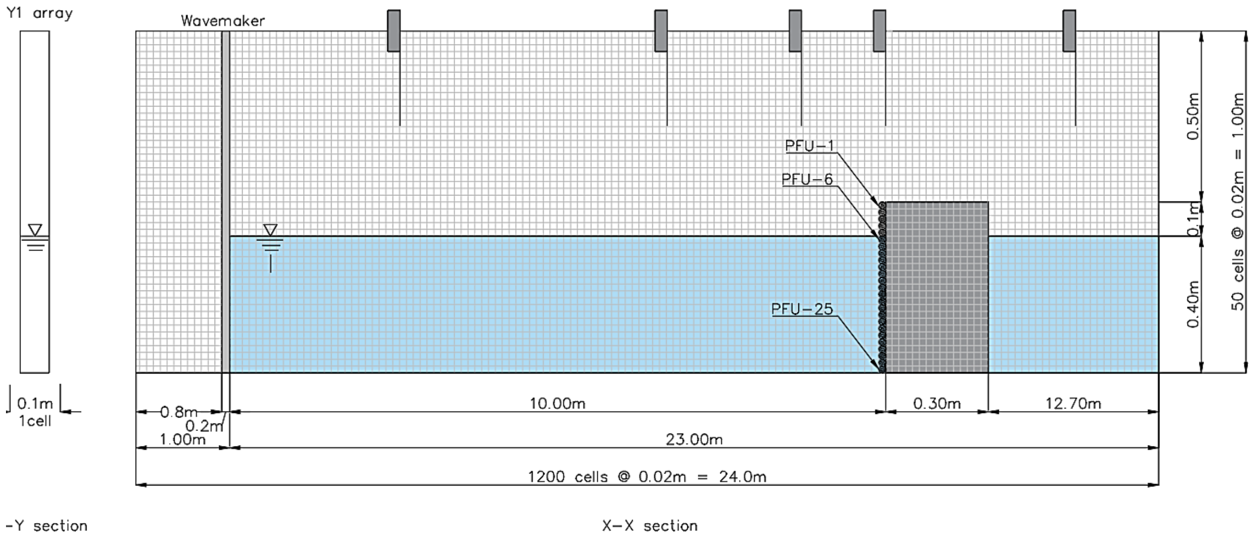

Figure 5.10. Diagram of the analysis model

Both the ‘computed’ time series of the board movement and the actual motion of the board ‘measured’ during the experiments are incorporated in the simulations. The wave elevations due to each are displayed in Figure 5.11.

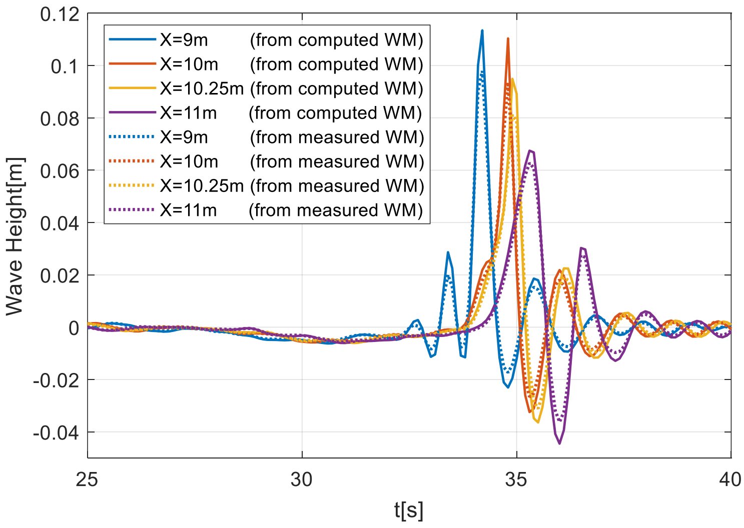

Figure 5.11. Wave elevation due to computed and measured wavemaker board motion. CADMAS simulation

Contrary to what was observed in the experiments, the concentrated wave is obtained at the target location for both board time series displacements. The difference in the wave generator motion does not affect the wave phase, but it does affect the maximum wave heights. As expected, the wave height at the target location is lower for the ‘measured’ board motion since the latter has a smaller amplitude.

Table 5-5. Maximum wave elevation attending to wavemaker motions. (Computed vs. Measured board motion)

WG location	Using board motion (Computed) [cm]	Using board motion (Measured) [cm]	M-C [cm]
9 m	11.34	9.79	-1.55
10 m	11.04	9.36	-1.68
10.24 m	9.49	8.11	-1.38
11 m	6.75	6.27	-0.47

Concerning the design wave height, the ‘computed’ board motion leads to an overestimation of the wave height by 1cm, while the ‘measured’ underestimates it by 0.4cm. It is expected that the wave due to the ‘measured’ board motion is lower than due to the ‘computed’ one since the amplitude of the former is lower than the latter.

On the other hand, the overestimation of the wave elevation in the numerical simulation using the ‘calculated’ board motion is consistent with the results in the method description by Aoki and Koga (2021). In the study, the waveforms of the calculated values with the linear theory generally correspond to the results of CADMAS. They are decided to be of sufficient use for the concentrated waves of arbitrary waveforms. However, variations on the wave elevation with respect to the design value were obtained in the range from 0.5cm to 5cm. For short duration times t_o, the maximum value of the water level was difficult to reproduce. This is seen in Figure 5.12, where for t_o = 0.5s, the set value p_o = 0.2m is not reached even for linear theory, partly due to the lack of time for the wave to grow. On the other hand, when t_o = 2.0s, the maximum value of the water level is slightly large, and the onset of the water level is somewhat faster, probably due to the nonlinearity of the waves.

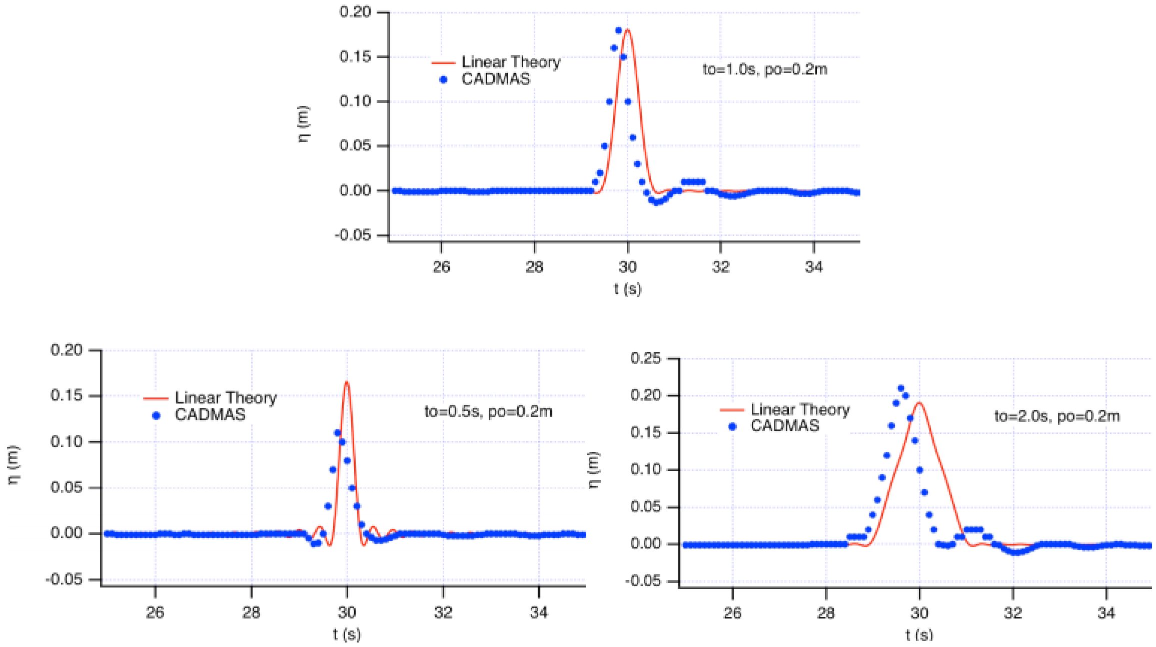

Figure 5.12. Wave elevation for different wave times. Aoki and Koga (2021)

As explained before, not obtaining the exact maximum wave elevation with the predetermined electric signal during physical tests can be resolved by adjusting the input gain, which increases the amplitude without phase variations. Thus, the obtention of waveform and close values for the maximum wave elevation is enough for the study. The time series of the wave elevations due to CADMAS simulation and the physical test are displayed in Figure 5.13 and Figure 5.14, respectively. It shows that the diverse waveforms during the physical tests are obtained at locations centimeters after the theoretical and numerical target. Table 5-6 shows the maximum wave elevation for each case.

Table 5-6. Maximum wave elevation at different locations. (CADMAS vs. Experiments)

WG location	CADMAS (Measured) [cm]	Experiments [cm]	CADMAS – Exp. [cm]
8.6 m	9.43	7.71	1.72
9.6 m	*9.98*	7.94	2.04
10 m	*9.36*	*8.51*	*0.85*
10.25 m	8.26	*9.99*	1.73
11.6 m	5.92	4.56	1.36

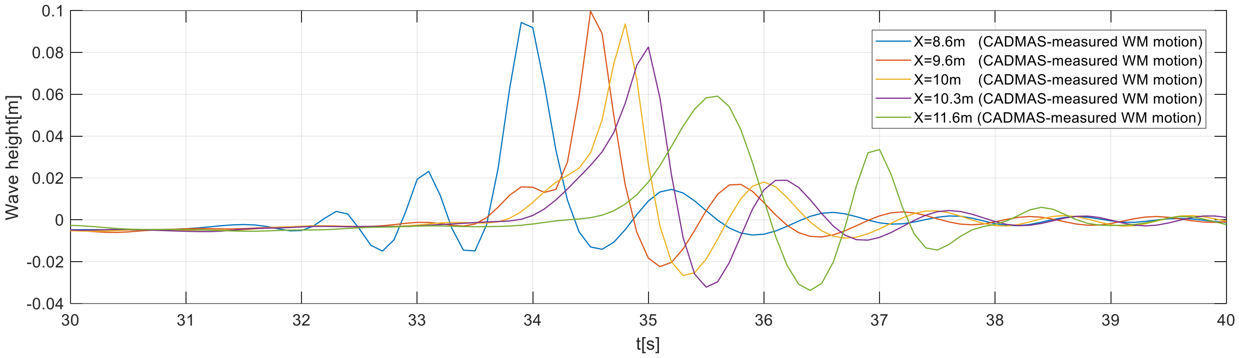

Figure 5.13. Time series of wave elevation. CADMAS simulation with real WM board motion

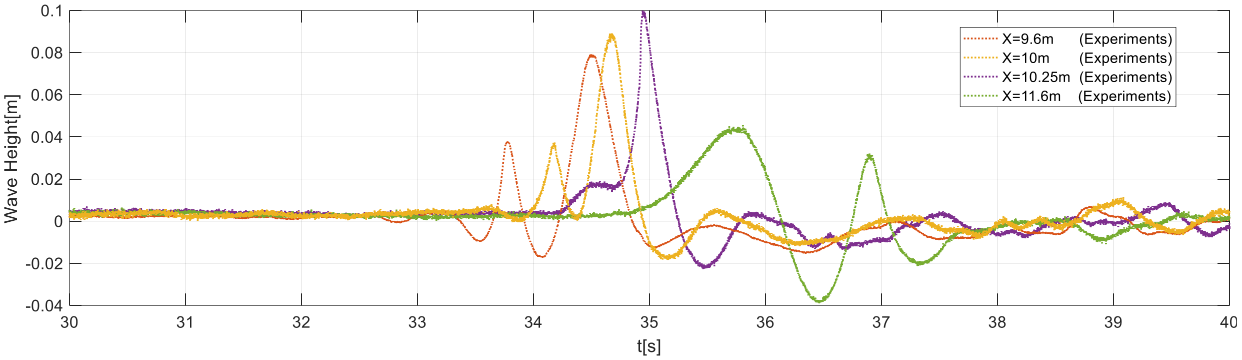

Figure 5.14. Time series of wave elevation. Experimental results.

Furthermore, when analyzing changes in the rising time of the wave, the first observation is that board movement needs to replicate a more extensive range of low-frequency movements, which, as we concluded in the previous subsection, is difficult for the generation mechanism. Thus, the experimental output is expected to not completely match the predicted wave elevation.

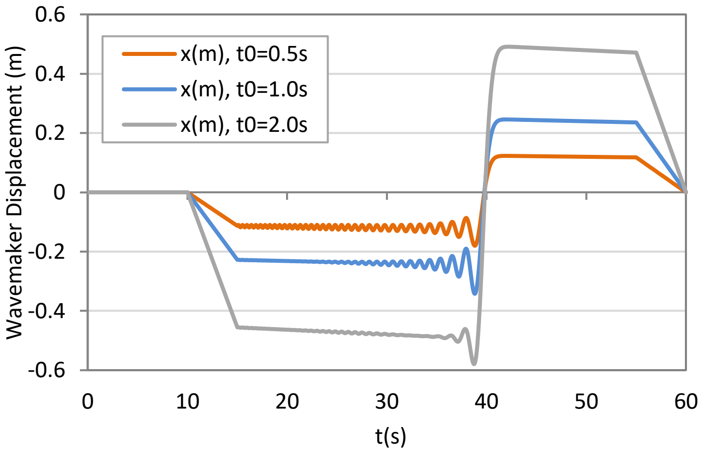

Figure 5.15. Board displacement for various rising times (h=0.4m, X=10m, η_{max}=0.1m)

Additionally, higher rising times require larger amplitude strokes according. A special note about the parameter rising time $\boldsymbol{t_o}$ and the employed symbology: $\boldsymbol{t_o}$ was the total wave period in the Aoki and Koga (2021) study and not the rising time. For the triangular waveform, the rising time is half of the total wave period. As a result of the variation of the rising time, although a distinctive unique wave is observed at the target location for all cases, rising times outside of t_0=0.5s lead to more unstable water level elevation and different phases. (Figure 5.16-below). The instability is also observed in wave gauges closer to the wave board (Figure 5.16-above) for larger rising times.

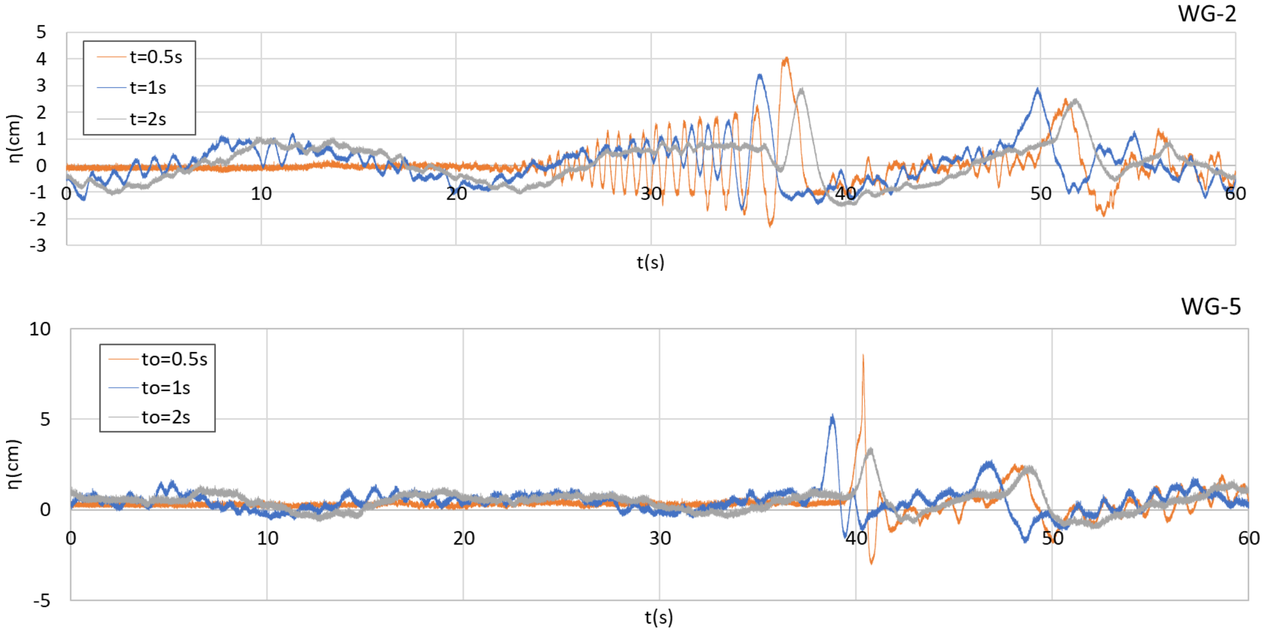

Figure 5.16. Time series of wave elevation for different wave rising times. Experimental test.

Another difference from the linear theory is that although rising times should theoretically generate higher wave height (Figure 5.12), the physical test shows that the maximum wave elevation gets drastically reduced. Then, rising times of 0.5s or wave period 1s are the best adjusted to the target waveform. The best relationship between wave height, target location and rising time must be tested and selected for configurations other than the one used in this study. Numerical tests are first recommended until a stable waveform and close wave height values are obtained, and later, the latter is adjusted during the physical test.

5.3 WAVE FORCE TEST

In Chapter 2, existing models for time-history wave loads on caisson breakwaters were discussed. Such models are used for the analytical determination of the sliding. In this study, the wave force in time-domain $F(t)$ is determined by a triangle-shaped profile that needs two critical parameters: the static frictional force F_s, which is possible to determine with the weight of the structure and the friction coefficient and the maximum wave force acting on the wall F_{max}. The procedure and results of experimentally determining the latter are described in this subsection.

The actual time series of the wave force acting on the wall of the caisson is determined experimentally by utilizing a mock structure of 300x220x500mm (Figure 5.17), which corresponds to 1/3 of the length of the caisson model to be used in the sliding test and measuring the forces. Such reduction is done to better comply with the measurement instruments' load-rated capacity. The sampling rate of the forces was of 0.001 second (1kHz).

The model is made of wood, and a load sensor is attached to its upper face. A gap of 1cm between the model and the flume bottom is left since the direct location on the bottom leads to error measurements by the sensor. The six components of the translational force (F_{xyz}) and the moment of force (M_{xyz}) are detected by the strain gauge, although only the F_x component in the direction of the impulsive wave is representative in this study. According to the supplier, the built-in transducer and digital processing make it less susceptible to noise and enable compact measurement. However, another factor is that direct contact with the impulsive wave interrupts the measurement.

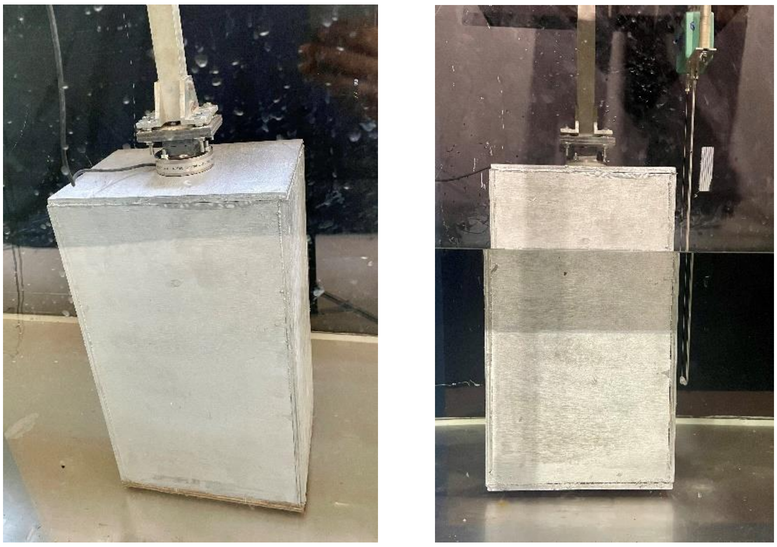

Figure 5.17. Caisson model used in the wave force test.

The natural frequency of the structure is initially determined in dry conditions (without water in the flume) by a simple bump test. The caisson is gently struck with a hammer in the direction of the wave, and the sensor measures the impact forces, which are later used to create time histories. A Fast Fourier Transform (FFT) analysis is applied to the time series, and the corresponding spectral representation is extracted. An illustrative example of the results related to the rocking motion of the caisson subject to the impact is given in Figure 5.18, showing the time series (left) and the corresponding spectral representation.

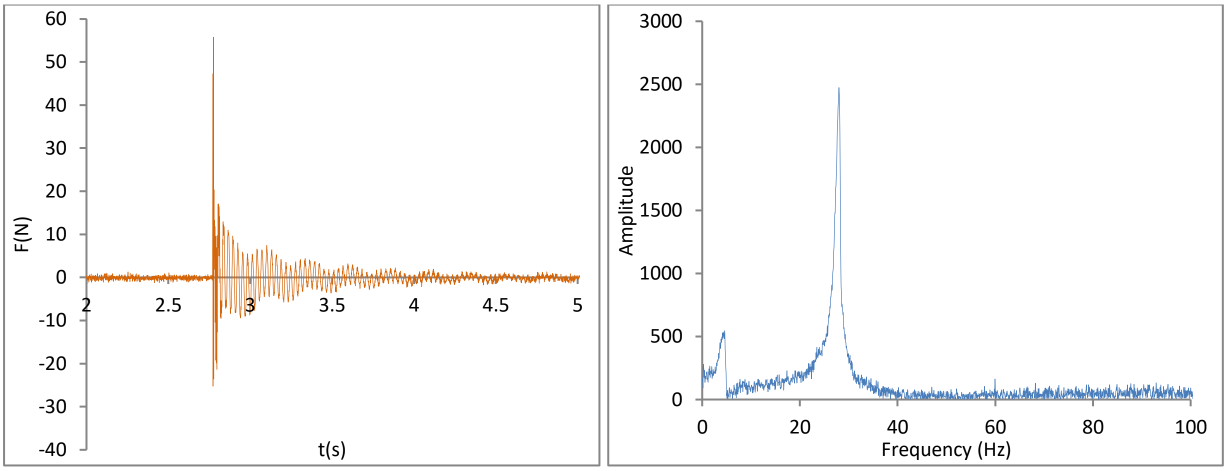

Figure 5.18. Time series (left) and power spectral density for hammer exciting source.

Two resonance peaks correspond to two modes of natural frequency; a well-defined peak is seen at 28 Hz, taking this value as the natural frequency of the structure to analyze the wave-induced vibration response.

The figure below shows an example of the time series of the wave force acting on the wall under wet conditions (wave flume with 0.4m of water depth). Two defined peaks are seen at 22Hz and 60Hz, related to the structural mode of the wave-induced vibration responses and the component of the oscillatory frequency alternating current in supplied from outlet, respectively. For all the measurements, the time series is shortly interrupted for 0.2 seconds when the overtopping water reaches the sensor. This happens after the impulsive peak; thus, it doesn't affect the measurement of the maximum force. Considering the structure's natural frequencies, the time series of the wave forces are denoised from where a maximum value is obtained, 48N, the maximum wave force F_{max}. This value is for the mock caisson with a 22cm length; thus, the maximum value in the figure is then extrapolated to the full length of the caisson (66cm) as shown in Table 5-7.

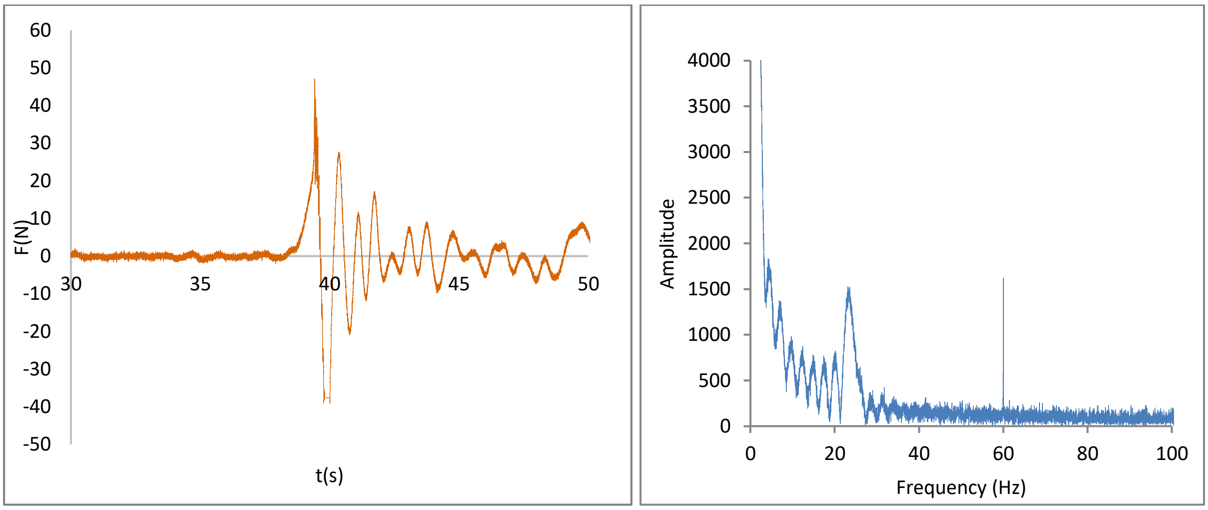

Figure 5.19. Time series (left) and power spectral density for impulsive wave exciting source.

Table 5-7. Model and force characteristics from the experiments.

Characteristics	Symbol and Units	Quantity
Frictional coefficient	f_s	0.37
Caisson mass	M [kg]	113
Caisson mass in water	M_w [kg]	79.2
Structure weight in water	$W = (M-M_w)*g$ [N]	331
Static Frictional Force	$F_s = f_s W$ [N]	123
Maximum wave force	F_{max} [N]	144
Magnitude wave force	$\alpha = (F_{max} - F_s)/ F_s$	0.17
Force rising and declining time	t_1, t_2 [s]	0.7s, 0.3s

The impact horizontal forces over the vertical face measured during the physical model test are lower when compared with values from some methods for predicting wave impact forces on vertical breakwaters (Allsop and Vicinanza, 1996) (British Standard, 2000) presented in Chapter 2 of this study. For example, using the recommendation from British Standard to a water depth of 0.4m, the impact force should be around 67 N for 0.1m of wave height, representing over 40 % of our measured value, and 48N for 0.09m matching the measured force but not reaching the wave height. It is important to notice that most of these values are for preliminary designs, have empirical values, most of them obtained from large-scale or prototype experiments, and are focused on actual structure dimensions. Thus, the scale factor plays an important role when comparing with these prediction methods.

Based on the model characteristics and its static frictional force, the rising time related to the sliding (the time from when the caisson starts moving because the wave force is higher than the frictional static force to the moment when the maximum wave force is achieved) is about 0.005s. Taking into account the scale of the experiments, a 0.0025s would be an estimated value; however, all impulsive wave characteristics are not necessarily scalable. The magnitude of the wave force is 0.17. Furthermore, these two parameters are strictly bound to each other for physical reasons and thus should not be assumed to be independent.

5.4 SLIDING TEST

The main objective of the physical experiments is to determine the displacement of the caisson with the different plate arrangements. Thus, a sliding test is done after selecting the impulsive wave set-up.

5.4.1 *Procedure*

The structure model: a box of 300x660x500mm made of plexiglass filled with coarse white sand is located in the flume at 10.25m of the wavemaker board with its larger dimension parallelly facing the board. A 2cm gap is left at each side to add the beams sustaining the horizontal plates and to avoid the silicone-like bottom-wall joints of the flume that can affect the sliding due to different friction factors.

Initial test runs of the impulsive waves are done to ensure the structure's displacement and adjust the structure's mass through the incorporation or removal of the fill material for a stable sliding, proceeding to the sliding tests for each case. A three- and five-time average is taken from each test's results, dismissing the cases where rotation or no movement is seen.

One of the problems encountered when performing tests in the wave tank was the reflection process going on between the metallic generation board and the caisson. Thus, a continuous wave cycle was not followed, and a one-by-one concentrated wave was generated with a gap of 5 minutes to allow the surface stabilization. On occasions, that time was increased due to the repositioning of the caisson during the sliding test.

Video images are recorded during each test to obtain the displacement of the structure. The video image processing was done using Dipp-Motion V from Digital Image Technology (DITECT). It is a 2D motion analysis software based on normalized cross-correlation, binarization of grayscale, HLS color (hue, saturation, and lightness), and checker-marker tracking. More information can be found in the technical documentation on the official website of DITECT Corporation.

The sliding experiment was repeated with the same parameters: 0.4m water depth, 0.1m maximum wave height, 1s wave period, and 0.5s rising time in two locations at x=10.25m and x=9.25m, ‘Experimental 1’ and ‘Experimental 2’, respectively. In the former location, only the plate length influence was tested; while in the latter, the submersion plate was added to the testing.

5.4.2 *Results*

Plate length

Table 5-8. Location of caisson with a plate at the surface at the beginning (*ti*) and end (*tf*) of the motion. shows screenshots of representative videos for the first sliding test of the caisson with rear plates at the surface. For this case, the ratios plate length to water depth ***l***/***h*** = 0, 0.5, 0.75, 1 are tested corresponding to plate lengths ***l*** = 0, 20cm, 30cm and 40 cm, respectively. The ratio ***l***/***h***=0.25 was initially dismissed in this test since it had a small influence on the analytical analysis. The initial and final positions can be seen in the second and third rows. From the visual analysis, it is already evident the sliding reduction is higher for the cases HS0_PL20 (***l***/***h*** = 0.5) and HS0_PL30 (***l***/***h*** = 0.75) when compared with HS0_PL20 (***l***/***h*** = 0). The time series of the caisson sliding for each ratio ***l***/***h*** plate are gathered in Figure 5.23. A correlation adjustment has been made to the time series since they are collected from videos manually taken and the initial time for each recording was not necessarily the same. Correlation was made taken the beginning of the displacement.

Table 5-8. Location of caisson with a plate at the surface at the beginning (t_i) and end (t_f) of the motion. Plate length:0,0.2,0.3,0.4m

	Case: HS0_PL0 Plate length = 0m	Case: HS0_PL20 Plate length = 0.2m	Case: HS0_PL30 Plate length = 0.3m	Case: HS0_PL40 Plate length = 0.4m
t_i			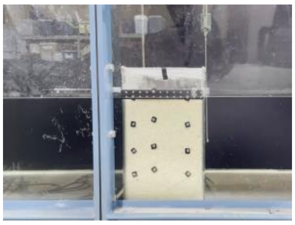	
t_f			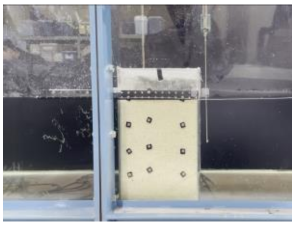	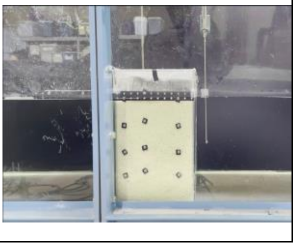

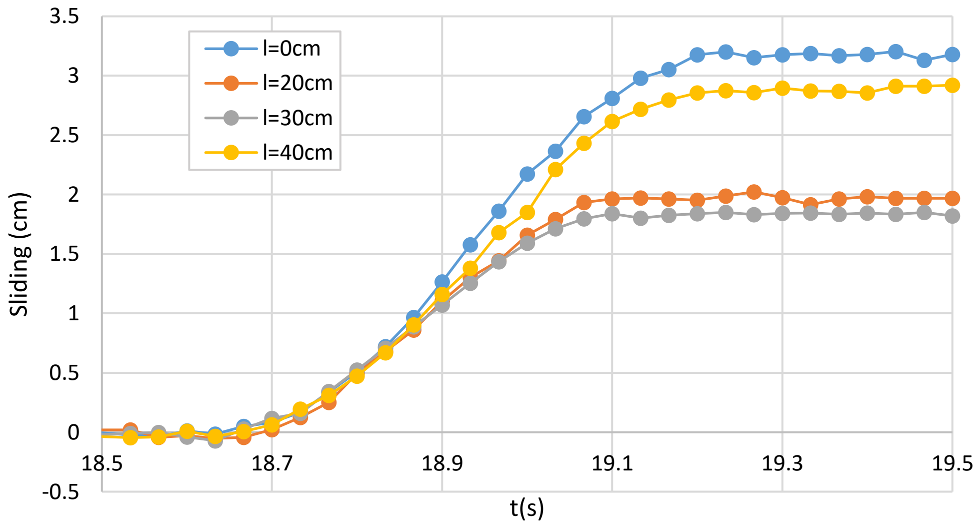

Figure 5.20. Time series of the caisson sliding with different plate lengths ((Experimental 1)

All the plate lengths led to a reduction of the maximum displacement. It is also evident that the lower values are related to the plate length $\boldsymbol{l}$ = 0.75$\boldsymbol{h}$; the case with $\boldsymbol{l}$ = 0.5$\boldsymbol{h}$ also has a low displacement compared to the non-plate case. While the one with the longest tested plate ($\boldsymbol{l} = \boldsymbol{h}$)

has larger sliding than the ***l*** = 0.5***h*** and ***l*** = 0.75***h***, the maximum sliding is actually closer to the regular caisson. The measurements of displacement and the estimated velocity related to it are shown in Figure 5.21. The 20 cm and 30 cm-plate caissons have slower movement under the impact of the impulsive wave: the sliding time-lapse is lower, and the maximum velocities are smaller than those from the no-plate and 40 cm-plate caissons. This behavior would translate to more stable caisson motions.

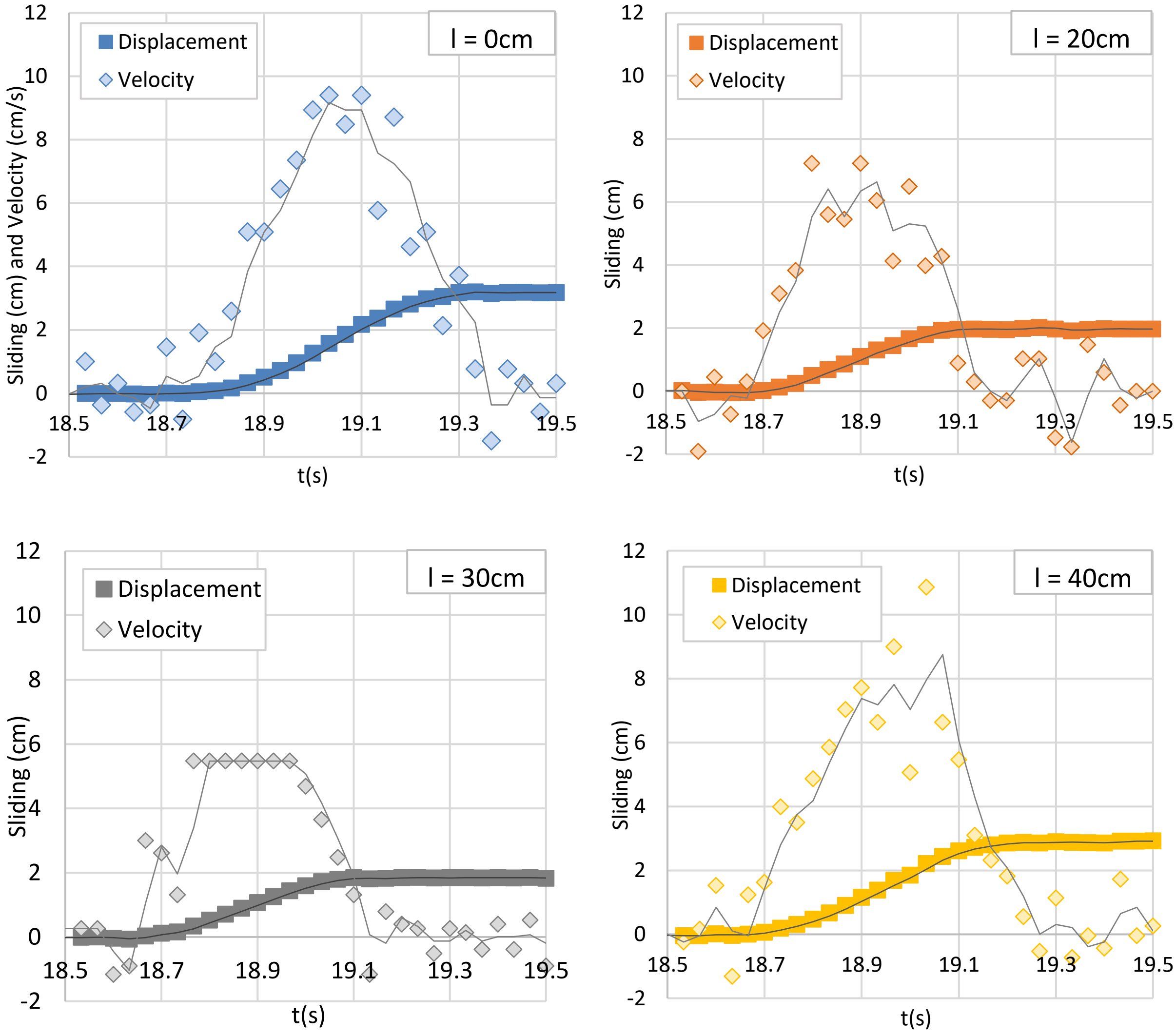

Figure 5.21. Time series of the caisson sliding and velocity for different *l/h* (Experimental 1)

Figure 5.21 displays the final displacement, i.e., from the start to the end of the motion. However, the maximum sliding does not always necessarily match with the final sliding in vertical caissons, as shown in Figure 5.22, where the time series for a slightly lower-mass caisson during the second test was recorded. The caisson moves in the direction of the wave reaching a maximum point, and after that, it moves slightly in the opposite direction until it stops, which is the latest sliding. This is due to the dynamic response of the structure and the wave overtopping, which leads to hydrodynamic forces acting on the back wall and pushing the structure in the seaside direction.

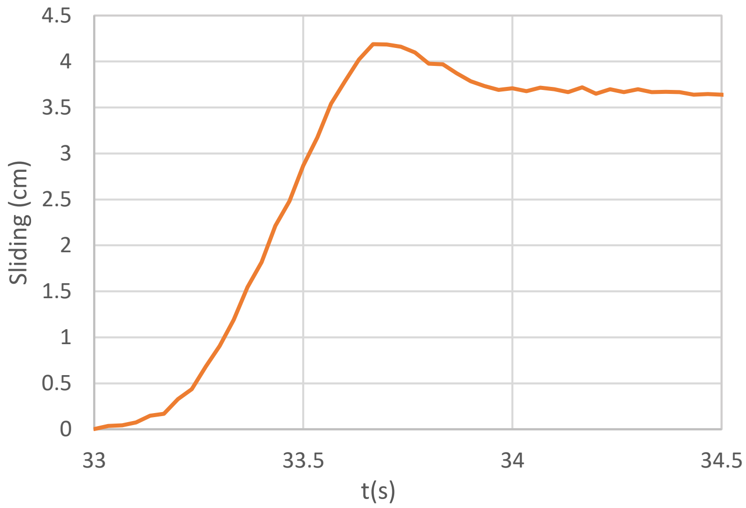

Figure 5.22. Sliding time series for a lower caisson mass. (Experimental 2)

A caisson mass was considered to avoid such conditions for the plate length and submersion tests. This does not yield to rocking movement in the current set-up. Still, in conditions with a rubble foundation, the back and forward movements affect the arrangement of the foundation particles, eventually leading to faster instabilities and other types of failure, such as foundation failures.

Sliding reduction based on the final positioning of the caisson is compiled below for the two experimental tests. As expected, in both cases (Experimental 1 and 2), all the plate lengths led to a reduction in the sliding. For the first case, the sliding reduces with increments of the plate length up to 30 cm (l/h = 0.75) and from there has a drastic change, increasing the sliding for the case 40 cm (l/h = 1), although not reaching the displacement by the non-plate caisson (l/h = 0).

The second test shows the same reduction behavior, but before the drop in sliding reduction for the 40 cm plate (***l***/***h*** = 0), there is a slight 1% reduction from ***l***/***h*** = 0.5 and 0.75. That differentiates from the first test with a 7% increment between ***l***/***h*** = 0.5 and 0.75 cases.

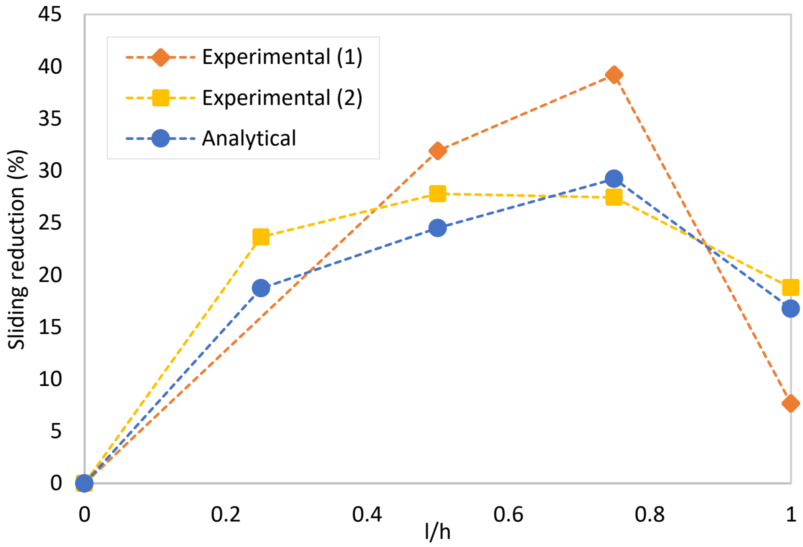

Figure 5.23. Final sliding of caisson according to plate length variation.

Furthermore, when the measured incident force and experimental geometric characteristics are used as input in the analytical model, the sliding reduction due to the plate length is represented as the blue points. The behavior is similar with increments up to ***l***/***h*** = 0.75 and dropped reduction for ***l***/***h*** = 1. However, the analytical model mostly shows smaller values than the experiments. This is related in principle to the non-linearity of the physical phenomenon and the hydrodynamic response of the physical model itself, which includes factors that are impossible to cover entirely by the analytical model, including trapped air, etc.

Plate submersion.

The 20 cm plate was selected for the plate submersion analysis based on the results of the plate length analysis both from the analytical model and the experimental test. Both 20 and 30-cm plate caisson had similar behavior, with the latter slightly higher than the former. Thus, the shorter plate is selected from an economic and design viewpoint. Table 5-9 shows screenshots of representative videos for the first sliding test of the caisson with rear plates at the surface. For this case, the ratios of submersion depth to water depth h_s/h = 0, 0.2, 0.25, 0.5 and 0.75 are tested corresponding to plate length l = 20cm.

Table 5-9. Location of caisson with a submerged plate at the beginning (t_i) and end (t_f) of the motion. Plate length:0.2m

	Case: HS0_PL20 Depth = 0m	Case: HS08_PL20 Case: HS10_PL20 Depth = 0.08, 0.1m	Case: HS20_PL20 Depth = 0.2m	Case: HS30_PL20 Depth = 0.3m
t_i		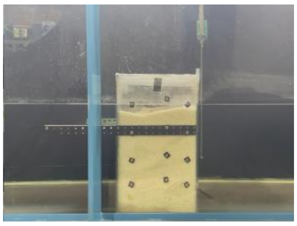	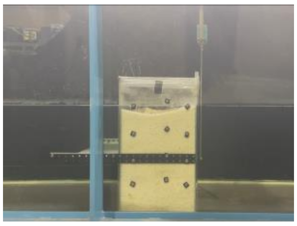	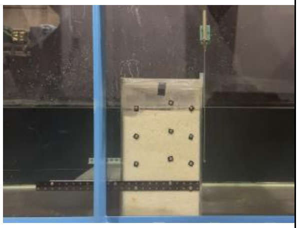
t_f	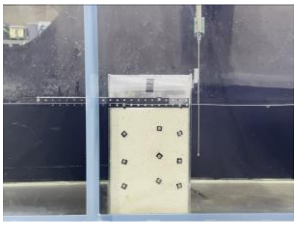	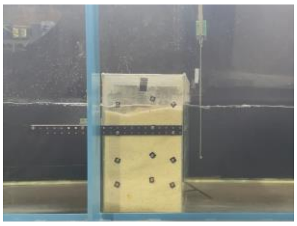	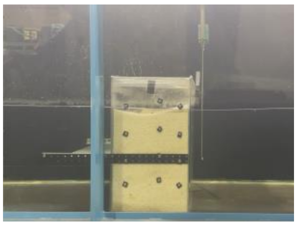	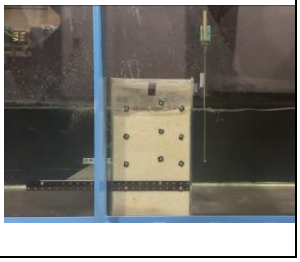

The values of final displacements for each relationship h_s/h are gathered in Figure 5.24. In general, the sliding reduction gets affected when the plate is submerged, turning from the positive influence of the plate at the surface to a negative impact. Thus, submerged plates lead to an increment in the caisson sliding.

The test outputs for plates with 20 cm length (PL20) show that the sliding has a maximum peak the ratio of submersion depth to water depth $h_s/h =$ 0.25 and gets linearly reduced in the range for $h_s/h < 0.25$. A drop on the sliding occurs for $h_s/h = 0.5$ to later increase at $h_s/h = 0.75$ again and decrease until the plate is at the bottom, which is the no-plate condition. The 30 cm plate

(PL30) is examined and added to the graph below to check the previous variable behavior. The PL30 test confirmed the behavior for $\boldsymbol{h_s/h} < 0.25$, but for $\boldsymbol{h_s/h} = 0.5$, a larger displacement is seen. It is valid to point out that it is more compatible with what to expect from the phenomenon.

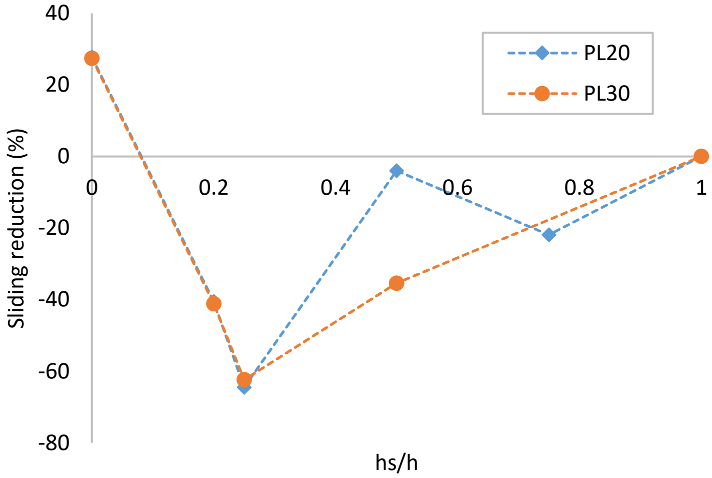

Figure 5.24. Final sliding of caisson according to plate length variation.

5.5 CHAPTER CONCLUSIONS

During the experimental investigation of breakwater caissons with rear plates, an impulsive wave was satisfactorily generated by using the method in Aoki and Koga (2021). The target waveform is reached around 25cm after the target location. The amplitude of the wave maker motion is reduced in the signal transmission. Still, according to the analysis in the numerical wave flume, this is not the reason for the location displacement. The numerical model replicates waveform and location from the analytical model but slightly overestimates the wave height. When applying the method, not for a replica of an actual wave but for models with variations for testing rising times, it is recommended to previously do perform an analysis in a numerical wave flume, adjusting the relationship of wave height and rising time to prevent waveform instabilities.

The addition of the rear plate with lengths up to water depth value positively reduced the sliding when located at the surface. The sliding reduction went as far as 39% for a plate length $\boldsymbol{l}$=0.75$\boldsymbol{h}$. Longer plates led to smaller sliding as far as the plate length was smaller than 2/3 of the water depth. After that point, the sliding reduction drastically diminished. The sliding values for plate length $\boldsymbol{l}$=0.5$\boldsymbol{h}$ and $\boldsymbol{l}$=0.75$\boldsymbol{h}$ are similar, although the former is higher than the latter; thus, the shorter of those two might be better used for practical use. Furthermore, the submersion of the plate, contrary to the length, had a negative effect on the sliding. All cases of plate submersion $\boldsymbol{h_s}$>0.1$\boldsymbol{h}$ led to larger sliding than no-plate caisson cases. Both behaviors, regarding the influence of plate length and submersion, correspond to those from the application of the analytical study.

Chapter 6. CONCLUSIONS

OUTLINE

This chapter summarizes the conclusions of this study based on the findings in Chapter 4 and Chapter 5, which are related to the analytical and experimental models for the investigation of caisson breakwaters, their dynamic response, and their sliding against impulsive waves, respectively.

CONCLUSIONS OF THE ANALYTICAL MODEL

As part of the basic research to enhance the accuracy of caisson motion models, an improved sliding model for regular caissons based on the application of the wavemaker theory and considering the hydrodynamic uplift forces added to the system by the plates was developed, providing a better assessment of the effect of this element on the caisson sliding reduction. The model includes using parameters related to the damping to account for the energy dissipation due to the presence of the plate. The caisson dynamics are modeled using a time-step numerical method to solve the equations of motion for a rigid body numerically.

A methodology is established and applied to superficial and submerged single and multiple plates, simulating the dynamic behavior of the new caisson shapes to analyze later the effect of the plate length and submersion depth on the overall sliding of the structure, which proved to be, along the methods and techniques within it, more practical, accessible and faster. The Boundary-Point Selection Method (BPSM) was applied with excellent results in finding solutions for boundary problems related to breakwaters with horizontal plates. Its application simplifies formulations and reduces programming and computing time. However, it is limited to geometries where the fluid regions have constant water depth. Additionally, aspects related to applying the

Boundary Point Selection method were highlighted, such as the increment of selection points for submersion depths smaller than 25% of water depth to avoid unstable or error results.

Following the main findings regarding the pressures: a) Reasonable distributions according to the boundary conditions were obtained b) The horizontal plates affect the pressure distribution on the caisson, mostly bringing more uniform distributions at the wall for the case of the single plate and at the plates for the twin-plate case; as well as higher pressure values, especially for the double plate, although with more variations on the wall distribution c) Regarding the plate length, the role of the plate as a pressure equalizer is confirmed: when plates' length tends to be equal to the water depth, the plate starts functioning as a pressure equalizer. c) The ratio of the imaginary to the real part of the pressure complex values varies according to the different plate arrangements; thus, its influence should not be dismissed when analyzing annexation elements such as horizontal plates since their geometry resists the forces acting in that direction.

The analysis results confirmed the critical influence of uplift forces on the sliding calculations, as well as the importance of including the memory-effect function on it. Excluding the first one leads to overestimating the horizontal plate's positive influence in reducing the sliding, especially for large *l/h* ratios. While dismissing the latter, it overestimates the maximum sliding distance.

The double plate analysis confirmed the increments of the added mass; however, it also showed a drastic reduction of the memory effect, which led to an increase in sliding. This confirmed that an increase in the added mass does not lead to smaller displacement and that the memory-effect function plays an important role in the sliding simulation under impulsive wave loads, which has been underestimated. Additionally, a relation in which shapes with larger damping coefficients and added mass increments induce better structure performance. Furthermore, for a preliminary prediction of better performance, i.e., a reduction of the sliding distances, analysis based only on the Added Mass is not enough; instead, also searching for sections with larger values of memory effect focusing on larger values of R^*(t=0) should be included.

A general conclusion from the preceding findings is that the analytical model for caissons with plates should not be simplified up to the point of the conventional models used for regular caissons since they underestimate the sliding of this structure and lead to fictional preliminary assumptions of great responses.

CONCLUSIONS OF THE EXPERIMENTAL MODEL

Small-scale laboratory experiments were carried out for the impulsive wave generation, forces, and the motion of a caisson, both regular and with horizontal rear plates. A numerical calculation in CADMAS-SURF was also conducted to investigate the reproducibility of the analytical method and the experimental wave generation. The influence of the plates on the sliding of the caisson during the physical tests was discussed.

During the experimental investigation, impulsive waves were satisfactorily generated by using the Aoki and Koga (2021) method. The target waveform was reached around 25cm after the target location from the analytical model. The amplitude of the wave maker motion was reduced in the signal transmission, but according to an analysis of a numerical wave flume, that was not the reason for the location displacement. The numerical model replicates wave form and location using the analytical model but slightly overestimates the wave height. When applying the method, not for a replica of an actual wave but for models with variations for testing rising times, it is recommended to previously do perform an analysis in a numerical wave flume, adjusting the relationship of wave height and rising time to prevent waveform instabilities. Furthermore, scale effects probed to be limitations in the physical modeling because it was impossible to satisfy all scaling parameters. At the same time, the numerical model, although not directly affected by it, had some parameters introduced indirectly through modeling assumptions but with less influence on the final output.

Finally, the addition of the rear plate with lengths up to the water depth value positively reduced the sliding when located at the surface. Longer plates led to smaller sliding as far as the plate length was smaller than 2/3 of the water depth. After that point, the sliding reduction drastically diminished. The sliding values for plate lengths in the range $\boldsymbol{l}$=0.5$\boldsymbol{h}$ to $\boldsymbol{l}$=0.75$\boldsymbol{h}$ were similar, although the former was higher than the latter; thus, from practical use, the shorter of those two might be better used. Furthermore, the submersion of the plate, contrary to the length, had a negative effect on the sliding, leading to larger sliding than no-plate caisson cases.

LIMITATIONS AND RECOMMENDATIONS

The presented analytical model can be applied to determine the hydrodynamic parameters and sliding of multiple shapes in other to preliminary determine best performance. However, the use of the boundary point selection method for the velocity potential calculation is restricted to shapes where the fluid in each region has constant water depth. For geometries not complying with this condition, the velocity potential can be calculated with the conventional approach; and follow the rest of the present methodology to determine the hydrodynamic parameters and sliding.

The experimental analysis showed that the analytical model was correct predicting the best shapes. However, the quantitative influence of the plate on the sliding reduction was different from the experiments and the analytical model with the experimental parameters when compared with the initial analytical model. This is mainly due to the differences in the parameters, properties and characteristics: mainly the friction coefficients, wave force rising time and magnitude. A sensitive analysis of the multiple combinations of the variability of such parameters is not included in this part of the study. Proceeding with it is expected to provide a better understanding of the quantitative effect of the plate based on such parameter’s variability.

Additionally, the experimental sliding tests at this scale within a flume led to an adjustment of materials and reduced workability. Carrying similar experiments in a basin will increase the workability for the repositioning of the caisson, the addition and change of plates u other annexation elements, as well as location variation of measurement devices. It would also allow to utilize materials with properties closer to the prototypes: concrete caissons, concrete bottoms that are not damaged by the friction with the caisson, sand or gravel over it during the sliding.

The scale in the physical experimental was exact for the caisson dimensions, not the case for the density since the material were different as well as further mass reduction to secure a representative sliding under a wave with limited overtopping. to be measured with the current camera (providing 30 frames per second). A further reduction of the scale is not recommendable since, although the caisson dimensions can be directly scalable and reduced, scaling all the wave parameters is practically impossible, and can introduce larger errors. Larger scales, i.e., larger models would lead to results closer to real wave and structure performance.

The analytical model did not consider wave overtopping; thus, the generated wave was designed for a maximum wave elevation equal to the caisson freeboard. However, some overtopping was observed during the physical test, a representation of the natural behavior associated to impulsive waves impacting structures. Including the overtopping in future models will be a better representation of the phenomena. It will also contribute to provide insights on the influence of the plate on other process such as foundation’s erosion that can occur in the harborside of the caisson due to such overtopping, leading to other failures. From the visual inspection during the physical tests, a positive impact can be expected since the possible erosion will be produced far from the back toe of the caisson.

GENERALS

The analytical models reproduce the behavior shown in the experiments well. They can be used in determining the sliding and hydrodynamic coefficients, such as added mass and damping coefficient, of the different shapes of caissons as far as the fluid regions formed by such geometry have constant water depth. The models allow a preliminary fast estimation of caisson geometries leading to better performance under wave impact and the reduction of extended resourceful physical experiments to the best shapes. Best approximations of the actual behavior will be obtained from the model by utilizing accurate input data, especially those related to the wave characteristics.

Physical models also performed according to the central hypothesis of the improved performance due to the fluid constriction. In the physical test, only the sliding and external forces were measured; thus, it is recommended to extend the measurements to pressure distributions and reaction forces, improving the phenomena' analysis and utilizing more accurate input data for the analytical models.

Besides particular differences due to the approaches used and the limitations of each study, both concluded that horizontal plates affect the sliding of caisson breakwaters. The impact is positive for plates located at the surface since sliding reductions are seen for these arrangements, while the submersion negatively impacts the parameter. On the other hand, increments of the plate length also had a good effect, decreasing the displacement of the caisson under the same conditions and with an optimal plate length between half and two-thirds of the water depth. Furthermore, the positive influence of the plate length started to decrease for plates longer than two-thirds of the water depth.

REFERENCES

Airy, G. B.9 (1845)*Tides and waves*. In Encyclopaedia metropolitana, vol.5, pp.241-396. London

Allsop N.W.H., Vicinanza D, Mckenna J.E., "*Wave forces on vertical and composite breakwaters*" Strategic Research Report SR 443, HR Wallingford, Wallingford, 1996.

Allsop N.W.H., Vicinanza D. :"*Wave impact loadings on vertical breakwaters: development of new prediction formulae*", Proceeding of the 11th International Harbour Congress, Antewerp, Belgium, 1996.

Allsop, N. W. H., H. Oumeraci, K. J. McConnell and A. Kortenhaus (1999). *New design methods for wave loadings on vertical breakwaters under pulsating and impact conditions*, Coastal Structures '99, ed. I. J. Losada, Spain, Balkemare, pp. 595-602.

Aoki S., Koga I.[2021]: *A method for generating concentrated waves of arbitrary waveform at arbitrary locations in a channel*. Coastal Engineering, 2021, Volume 77 , Issue 2, p. I_1-I_6. (in Japanese)

Aoki, S. and Okube A. [1995] "*Sliding simulation of upright breakwater*", Proceedings of Coastal Engineering, Vol. 42, pp.861-865 (in Japanese) (in Japanese)

Baqnold, R.A., (1939): *Interim report of wave pressure research*. Journal of Institute of Civil Engineers, Vol. 12, pp. 210-226.

Brennen, C.E. (2016). *Internet Book on Fluid Mechanics*. Dankat Publishing. Available at: http://brennen.caltech.edu/fluidbook/

British Standards BS-6349, "*Maritime structures Part 1: Code of Practice for general criteria*", BSI, London, UK, 2000.

BRITISH STANDARDS BS-6349, "*Maritime structures Part 1: Code of Practice for general criteria*", BSI, London, UK, 2000

CDIT (Coastal Development Institute of Technology) (2001). "*Research and development of numerical wave channel (CADMAS-SURF)*," Coastal Development of Institute of Technology, CDIT Library. No. 12 (in Japanese).

Cooker, M. J., Peregrine, D. H, *Model for Breaking Wave Impact Pressures*. Coastal Engineering. pp.1473-1483 (1990)

Cozzuto G., Dimakopulos A., De Lataillade T. Otinar P., and Kees C.: *Simulating oscillatory and sliding displacements of caisson breakwaters using a coupled approach*. J. Waterway, Port, Coastal, Ocean Eng. (145:3) pp. XX (2019).

Cummins, W. E. [1962] "*The impulse response function and ship motions*", Shiffstechnik, Bd. 9, Heft 47, pp.101-109. Available at:

https://dome.mit.edu/bitstream/handle/1721.3/49049/DTMB_1962_1661.pdf?sequence=1&isAllowed=y

Cuomo, G. (2007). *Wave impacts on vertical seawalls and caisson breakwaters*. Bulletin of the International Navigation Association, 25-38. Available at: https://repository.tudelft.nl/islandora/object/uuid:a56d6929-4696-41dd-830f-cc66da44f5e8/datastream/OBJ/download

Cuomo, G., Lupoi G., Shimosako K. and Takahashi S.: *Dynamic response and sliding distance of composite breakwaters under breaking and non-breaking wave attack*. Coastal Engineering Journal (58:10) (2011).

Dean R. and Dalrymple R: *Water Wave Mechanics for Engineers and Scientists*. 1st edn. Prentice-Hall. Inc. (1984).

Esteban, M. Takagi, H., and Shibayama, T. [2007] *"Improvement in Calculation of Resistance Force on Caisson Sliding Due to Tilting"*, Coastal Engineering Journal, 49:4, p.417-441, DOI: 10.1142/S0578563407001678.

Franco L. (1994) *"Vertical breakwaters: the Italian experience."* Special Issue on vertical breakwaters, Coastal Engineering 22:31-55. https://doi.org/10.1016/0378-3839(94)90047-7

Franco L. (1991) *"Vertical breakwaters: the Italian experience and lessons from failures"* Proc. of 1st Workshop of MAST G6-S-Project 2, Hannover, Germany.

Fundora Campos, S.M., Aoki, S. (2023). *Effect of Horizontal Plates on the Sliding of Breakwater Caissons*. In: Carbone, G., Laribi, M.A., Jiang, Z. (eds) Advances in Automation, Mechanical and Design Engineering. SAMDE 2022. Mechanisms and Machine Science, vol 138. Springer, Cham. pp-347-36. https://doi.org/10.1007/978-3-031-40070-4_28

Fundora Campos, Sila M.: *Effect of Horizontal Plates on the Sliding of Breakwaters Caissons*. Master Thesis, Osaka University. (2021).

Fundora Campos, S.M., Aoki, Si. (2024). *Effect of Submerged Plates on the Dynamic Response and Sliding Simulation of Caisson Breakwaters*. In: Tajima, Y., Aoki, Si., Sato, S. (eds) Proceedings of the 11th International Conference on Asian and Pacific Coasts. APAC 2023. Lecture Notes in Civil Engineering, vol 394. Springer, Singapore. pp-863-876. https://doi.org/10.1007/978-981-99-7409-2_79

ASTM G115 Standard Guide for Measuring and Reporting Friction Coefficients. Available at: G115 Standard Guide for Measuring and Reporting Friction Coefficients (astm.org)

Galvin C.J. (1964). *Wave-height prediction for wave generators in shallow water*. Washington (DC): U.S. Army Corps of Engineers. TechnicalMemorandum No. 4; p. 1–20 Available at: CERC Technical Memorandum No 4 "Wave-height prediction for wave generators in shallow water" (dren.mil)

Goda Y. (1994) *"Dynamic response of upright breakwaters to impulsive breaking waves forces"* Special Issue on vertical breakwaters, Coastal Engineering 22:135-158. https://doi.org/10.1016/0378-3839(94)90051-5

Goda Y. , Takagi H. (2000), *"A reliability design method of caisson breakwaters with optimal wave heights"*, Coastal Eng. Journal 42, No.4

Goda, Y. (1974) *"New wave pressure formulae for composite breakwater",* Proc. of 14th Int. Conf. Coastal Eng., Copenhagen, Denmark, pp1702−1720. ASCE New York

Goda, Y. (2000). *Random Seas and Design of Maritime Structures*. Advanced Series on Ocean Engineering. 33. 10.1142/3587.

Goda, Y.(2010). *Random Seas and Design of Maritime Structures*, 3rd Edition. s.l.:World Scientific.

H. Oumeraci, A. Kortenhaus. *Analysis of the dynamic response of caisson breakwaters*. Coastal Engineering 22 (1994) 159-183

Hanzawa M., Matsumoto A., and Tanaka H.[2012]: *Applicability of CADMAS-SURF to evaluate detached breakwater effects on solitary tsunami wave reduction*. Earth Planets Space, 64, 955–964.

Hiroi I.(1920), *"The force and power of waves"*, The Engineer, 130, pp.184-187

Hirt, C. and B. D. Nichols [1981]: *Volume of fluid (VOF) method for dynamics of boundaries*, J. Comput. Phys., 39, pp.201–225.

Ijima T., Ozaki S., Eguchi Y. and Kobayashi A. [1974]: *Breakwater and quay well by horizontal plates*. Coastal Engineering. Chapter 94, pp.1137-1556.

Ishikawa, Y., Bai, L., *The 2024 Mj7.6 Noto Peninsula, Japan earthquake caused by the fluid flow in the crust*, Earthquake Research Advances (2024), doi: https://doi.org/10.1016/j.eqrea.2024.100292

Ito, Y., M. Fujishima, and T. Kitatani (1966): *On the stability of breakwaters*, Rept. of Port and Harbour Research Institute, Vol.5, No. 14, 134p (in Japanese).

Kashiwagi M.(2018): *Wave-body interaction theory. Theory of Ship waves. Lecture notes for a graduate course*. Osaka University Available at: http://www.naoe.eng.osaka-u.ac.jp/naoe/naoe1/image/2018-LectureNote.pdf

Kim T. and Takayama T. (2003) *Computational Improvement for Expected Sliding Distance of a Caisson-Type Breakwater by Introduction of a Doubly-Truncated Normal Distribution*, Coastal Engineering Journal, 45:3, 387-419, DOI: 10.1142/S0578563403000816

Kim T. and Takayama T. (2004) *Effect of caisson tilting on sliding distance of Breakwater Caisson*, Annual Journal of Civil Engineering in the Ocean, JSCE, Vol.20, pp.89-94.

Kortenhaus, Andreas & Oumeraci, H. & Allsop, William & Mcconnell, K. & Gelder, P.H.A.J.M. & Hewson, P. & Walkden, Mike & Müller, G. & Calabrese, Mario & Vicinanza, Diego. (2001). *Wave Impact Loads - Pressures And Forces*. Available at: https://www.researchgate.net/publication/2460541_Wave_Impact_Loads_-_Pressures_And_Forces

Kukavica, I., Tuffaha, A. *An inviscid free boundary fluid-wave model*. J. Evol. Equ. **23**, 41 (2023). https://doi.org/10.1007/s00028-023-00888-w An inviscid free boundary fluid-wave model | Journal of Evolution Equations (springer.com)

Loginov V. N. (1962) *"Evaluation of the pressure impulse on vertical structures subject to breaking waves."* Trudy Soiuzmorniiproekta (in Russian) 2:47-59

Loginov V. N. (1969) *"Non linear oscillations of vertical breakwaters subject to wave impact loads"* Trudy Soiuzmorniiproekta (in Russian) 27:67-75

Lundgren, H. (1969) *"Wave shock forces: an analysis of deformations and forces in the wave and in the foundation"* Proc. Symp. on Research in Wave Action. Delft Hydraulics Lab. Delft, The Netherlands, pp1−20. Available at: http://resolver.tudelft.nl/uuid:4a4a2af8-14c6-462c-8a2d-90df9e05d120

Marinski J. R. and Oumeraci H. (1992) *" Dynamic response of vertical structures to breaking wave forces-review of the CIS design experience."* Proc. of 23rd Int. Conf. Coastal Eng., Venice, Italy. ASCE New York, 1357-1370

NILIM, *A Draft Manual For Developing Earthquake-tsunami Disaster Scenarios Including Damage to Public Works*. ⟨http://www.nilim.go.jp/lab/bcg/siryou/ tnn/tnn0485.htm⟩, 2013 (May 29, 2014) (in Japanese).

Official website of DITECT Corporation. Available at:
https://www.ditect.co.jp/en/software/dipp_motionv.html

Omatsu S.: *On the transient wave phenomenon by a wave machine - in constant water depth* -, Bulletin of the Seibu Kankyo Kai, No. 57, pp. 53-67, 1978 (in Japanese)

Omatsu S.[2009]: *"On the Absorption Method of Transient Wave in the Time Domain,"* Proceedings of the Japan Maritime Research Institute, Vol. 9, No. 2, 2009, pp. 65-75. (in Japanese)

Oumeraci H., Allsop N.W.H., de Groot M.B., Crouch R.S., Vrijling J.K.. (1999) *Proverbs: Probabilistic design tools for vertical breakwaters.*
Available at: http://resolver.tudelft.nl/uuid:ce9ec158-78b0-484a-9344-d55c326b4ede

Oumeraci, H.: *Review and analysis of vertical breakwater failures – lessons learned. Special Issue on vertical breakwaters.* Coastal Engineering 22, pp. 3−29 (1994) https://doi.org/10.1016/0378-3839(94)90046-9

Oumeraci, H.; Kortenhaus, A. (1997): *Wave impact loading - tentative formulae and suggestions for the development of final formulae*. Proceedings 2nd Task 1 Workshop, MAST III, PROVERBS-Project: Probabilistic Design Tools for Vertical Breakwaters, Edinburgh, U.K., Annex 1.0.2, 13 pp; 3 Annexes

Raby A, Macabuag J., Pomonis A., Wilkinson S, Rossetto T. (2015): *Implications of the 2011 Great East Japan Tsunami on sea defense design*, International Journal of Disaster Risk Reduction, Volume 14, Part 4, pp.332-346, https://doi.org/10.1016/j.ijdrr.2015.08.009.

Sato T. Nikkei Crosstec, Nikkei Construction (2024): *Breakwater at Iida Port in Suzu City destroyed by tsunami, possibly contributing to tsunami inundation (xTECH)*. Available at: https://xtech.nikkei.com/atcl/nxt/column/18/02706/010900026/

Shimosako K., Takahashi S. and Tanimoto K. (1994) *"Estimating the sliding distance of composite breakwaters due to wave forces inclusive of impulsive forces"*, Proc. of 24th Int. Conf. Coastal Eng., Kobe, ASCE, pp 1580-1594

Shimosako, K and Takahashi, S. [1999] *"Application of reliability design method for coastal structures-expected sliding distance method of composite breakwaters"*, Proc. of Coastal Structures '99, pp. 363-371.

Shimosako, K. and Takahashi, S. [2000] "*Application of expected sliding distance method for composite breakwaters design*" in Procedures of 27th International Conference on Coastal Engineering, ASCE, pp. 1885-1898.

Shimosako, K., Osaki, N. and Nakano, F.: *Reliability design of composite breakwaters based on sliding distance*. Report of the Port and Airport Research Institute 45(3) (2006).

Stokes, G.G. 1846. *Report on recent researches in hydrodynamics. Report of the 16th meeting*, British Association for the Advancement of Science, Southampton. London, John Murray, p. 1–20 Available at: Google Scholar

Suppasri A., Shuto N., Imamura F., Koshimura S., Mas E. And Yalciner A.C.[2013] *"Lessons Learned from the 2011 Great East Japan Tsunami: Performance of Tsunami Countermeasures, Coastal Buildings, and Tsunami Evacuation in Japan."* Pure Appl. Geophys. Vol 170 (2013),p. 993–1018. DOI 10.1007/s00024-012-0511-7

Svendsen Ib. A.: *Introduction to Nearshore Hydrodynamics in Advances Series on Ocean Engineering*, vol.24. Ch.3. World Scientific Publishing Co. Pte. Ltd. (2006)
T. Arikawa, M. Sato, K. Shimosako, I. Hasegawa, G.S. Yeom, T. Tomita, Failure mechanism of Kamaishi breakwater due to the Great East Japan Earthquake Tsunami, in: Proceedings of the 33rd International Conference on Coastal Engineering, Santander, 2012.

Takagi, H. & Shibayama, T. [2006] "*A new approach on performance-based design of caisson breakwater in deep water*", Annual Journal of Coastal Engineering, JSCE 53, 901-905 (in Japanese).

Takahashi S., Shimosako K., Kimura K. and Suzuki K.: *Typical failures of composite breakwaters in Japan.* Proc. of 27th Int. Conf. Coastal Eng. ASCE New York. (2000)

Takahashi S., Tanimoto K., Shimosako K.,(1993): *Experimental Study of Impulsive Pressures on Composite Breakwaters.* Report of the Port and Institute Harbour Research. Vol.31 No.5 pp.33-72.

Takahashi, S., Shimosako, K., Kimura, K., & Suzuki, K. (2001). *Typical Failures of Composite Breakwaters in Japan.* Coastal Engineering 2000. doi:10.1061/40549(276)148

Takayama, T. and H. Fujii (1991). *Probabilistic estimation of stability of slide for caisson type breakwater*, Report of the Port and Harbour Research Institute 30, 4, pp. 35-64 (in Japanese).

Tanimoto K., Takahashi S.(1994): *Design and construction of caisson breakwaters— the Japanese experience,* Coastal Engineering, 22:1-2, pp. 57-77, https://doi.org/10.1016/0378-3839(94)90048-5.

Tomita, T., Yeom, G., Ayugai, M And Niwa T. [2012] *"Breakwater Effects on Tsunami Inundation Reduction in the 2011 off the Pacific Coast of Tohoku Earthquake"*. JSCE Proceedings B2 (Coastal Engineering) Vol.68, No. 2, 2012, p.156-160. (in Japanese)

U.S. ARMY CORPS OF ENGINEERS, *"Coastal Engineering Manual"*, 1110-2-1100, U.S. Army Corps of Engineers, Washington, D.C. (in 6 volumes), 2002

Usui A., Aoki S., Kawasaki K.[2017]: *Numerical study of arbitrary waveforms with self - propelled waves.* Civil Engineering Society B3 (Marine Development), Vol. 73, No. 2, pp. I_234-I_239. (in Japanese)

Usui A., Hiratsuka Y., Aoki S., Kawasaki K.[2016]: *Self-propelled wave for the tsunami and storm surge experiments*, the Civil Engineering Society Paper B2 (Costal Engineering), Vol. 72, No. 2, pp. I_31-I_36

Wagner, H., (1932): Uber stoss-und Gleitvorgange an der Oberflache von Flussigkciten, Zeishrift fur Angewandete Mathematik und Mechanik, Band 12, Heft 4, pp. 193-215.

Yoshida, A., Kojima, H., and Tsurumoto, Y.: *A collocation method of matched eigenfunction expansions on the boundary-value problem of wave-structure interactions*. JSCE Proceedings (417:13) (1990). (in Japanese)

Yoshihara, M.: *Development of breakwater with a horizontal plate for the purpose of reducing the amount of sliding of the caisson*. Master Thesis, Osaka University. (2019). (in Japanese)